

# The Search for New Quasicrystals

Peter J. Lu

A SENIOR THESIS SUBMITTED IN PARTIAL FULFILLMENT  
OF THE REQUIREMENTS FOR THE DEGREE OF BACHELOR OF ARTS IN PHYSICS  
AT PRINCETON UNIVERSITY

APRIL 24, 2000

© Copyright 2000 by Peter J. Lu.

All rights reserved.

# Abstract

Having examples of quasicrystals with a large variety of compositions and stoichiometries is important in exploring physical properties and finding practical applications. The discovery of new quasicrystals has historically depended on serendipity. The goal of this thesis is determine if a more systematic approach can be developed. Based on a theoretical understanding of quasicrystal diffraction properties, a computer search scheme has been developed to identify icosahedral quasicrystals based on records in the international Powder Diffraction File, a collection of about 70,000 x-ray powder diffraction patterns. The scheme is first tested by determining if it can successfully identify and index the known icosahedral patterns in agreement with published analyses. Then, the scheme is applied to the remainder of the Powder Diffraction File (materials described as crystalline) to identify the most promising quasicrystal candidates. The leading candidates are examined with electron microscopy. The electron diffraction patterns of the most thoroughly investigated of the mineral candidates to date, krennerite, strongly indicates that it is an incommensurately modulated crystal, only the second such incommensurate mineral known. The fact that the mineral arose from a search for icosahedral quasicrystals means that its structure is not only incommensurate, but the incommensurate ratios of diffraction wavevectors are simply related to the golden ratio. A generic incommensurate crystal can have arbitrary irrational ratios. The finding suggests that the incommensurability may be related to an icosahedral phase, perhaps one obtained by varying the stoichiometry slightly. The system merits synthesis and further testing in the laboratory.

# Acknowledgments

This thesis simply would not have been possible without the tremendous aid of a number of people. Thanks must first go to Professor Paul Steinhardt, Department of Physics, Princeton University, advisor of this thesis, whose careful guidance and extreme patience fostered an environment where learning was not only encouraged, but demanded. Professor Kenneth Deffeyes, emeritus, Department of Geology, Princeton University, my former academic advisor, was a constant source of new ideas, most notably that of checking for  $(\Delta N, \Delta M)$  pairs, as well as moral support. Thanks also to Professors Paul Chaikin and David Huse, Department of Physics, Princeton University, for help on the theory of scattering. On the experimental side Dr. Nan Yao, Princeton Materials Institute, provided constant encouragement and went far beyond the call of duty to acquire an electron diffraction unit in the scanning electron microscope for this investigation. Dr. Jeffrey Post, Curator-in-Charge, Mineral Collection, Department of Mineral Sciences, Smithsonian Institution, graciously provided the type specimens for both keithconnite and theophrastite, allowing our experimental investigation to move forward when there was literally no other way in the world to get access to these exceedingly rare minerals. Richard Bideaux, Mineral Data Publishing, graciously provided several volumes of his *Handbook of Mineralogy* and introduced me to the incommensurate calaverite system. I am also very thankful for the emergency last-minute proofreading of Professor Robert Bagley, Department of Art and Archaeology, Princeton University.

“To the only wise God, through Jesus Christ, be the glory forever. Amen.” [54]

“WHILE PENTAGONAL SYMMETRY IS FREQUENT IN THE ORGANIC WORLD, ONE DOES NOT FIND IT AMONG THE MOST PERFECTLY SYMMETRICAL CREATIONS OF INORGANIC NATURE, AMONG THE CRYSTALS.” [1]

—Hermann Weyl, *Symmetry* (1952)

# Contents

<b>Abstract</b>	iii
<b>Acknowledgments</b>	iv
<b>I Introduction and Background Theory</b>	<b>1</b>
<b>1 The Rational Basis of Conventional Crystallography</b>	<b>9</b>
1.1 An Historical Overview of Crystallography . . . . .	10
1.2 The Lattice . . . . .	13
1.3 Symmetry and Groups . . . . .	16
1.4 Symmetry Restrictions due to Periodicity . . . . .	18
1.5 Space Groups . . . . .	20
<b>2 Diffraction, Scattering and the Fourier Transform</b>	<b>23</b>
2.1 Classical Light Waves . . . . .	23
2.2 Fraunhofer Diffraction of Classical Light Waves . . . . .	24
2.3 The Fourier Transform . . . . .	26
2.4 General Scattering . . . . .	28
2.5 The Reciprocal Lattice . . . . .	31
2.6 Bragg Scattering . . . . .	34
2.7 X-ray and Electron Diffraction . . . . .	38
2.7.1 One-Dimension: Powder X-ray Diffraction . . . . .	39
2.7.2 Two-Dimensions: Single-Crystal Diffraction . . . . .	39

2.8	Diffraction and Symmetry . . . . .	40
<b>3</b>	<b>Quasicrystals</b>	<b>43</b>
3.1	The Quasilattice . . . . .	43
3.2	From Quasilattice to Quasicrystal . . . . .	45
3.2.1	Projection . . . . .	46
3.2.2	Phonons and Phasons . . . . .	49
3.3	Symmetry and Quasiperiodicity . . . . .	50
3.4	The Icosahedral Quasicrystal . . . . .	52
3.4.1	Decorations of the Icosahedral Quasicrystal . . . . .	55
3.5	Powder Diffraction of an ideal Simple Icosahedral Quasicrystal . . . . .	56
3.5.1	Deviations from the ideal powder pattern . . . . .	56
<b>II</b>	<b>Original Work</b>	<b>59</b>
<b>4</b>	<b>The Program</b>	<b>61</b>
4.1	The Powder Diffraction File . . . . .	61
4.2	Search Strategies . . . . .	62
4.3	Screening Criteria . . . . .	64
4.3.1	Hoaxes . . . . .	68
4.4	Comparison with the published data . . . . .	69
4.5	Key Search Results: Scatterplots . . . . .	70
4.6	Key Search Results: The List . . . . .	83
<b>5</b>	<b>Experimental Techniques: Electron Microscopy</b>	<b>85</b>
5.1	Overview of Scanning Electron Microscopy . . . . .	86
5.1.1	Secondary Electron (SE) Imaging . . . . .	91
5.1.2	Backscattered Electron (BSE) Imaging . . . . .	94
5.1.3	Energy-Dispersive Spectroscopy (EDS) . . . . .	96

5.1.4	Backscattered Electron Diffraction . . . . .	99
5.1.5	Combining Imaging Modes . . . . .	100
5.1.6	Artifacts: Charging . . . . .	102
5.2	Transmission Electron Microscopy . . . . .	103
<b>6</b>	<b>Experimental Results</b>	<b>107</b>
6.1	Krennerite, (Au,Ag)Te <sub>2</sub> . . . . .	108
6.2	Other Studies . . . . .	111
6.2.1	Ni(OH) <sub>2</sub> : Synthetic and Natural Theophrastite . . . . .	111
6.2.2	Volynskite, AgBiTe <sub>2</sub> . . . . .	116
<b>7</b>	<b>Conclusions and Directions for Future Research</b>	<b>119</b>
7.1	Conclusions . . . . .	120
7.1.1	Computer Programs . . . . .	120
7.1.2	Experimental Investigation . . . . .	121
7.2	Directions for Future Research . . . . .	122
<b>A</b>	<b>Published Quasicrystal Indexings</b>	<b>125</b>
<b>B</b>	<b>Top Ten Mineral Candidates</b>	<b>131</b>
<b>C</b>	<b>Top Fifty Overall Candidates</b>	<b>139</b>
<b>Bibliography</b>		<b>141</b>
<b>List of Figures</b>		<b>147</b>
<b>List of Tables</b>		<b>151</b>

# **Part I**

## **Introduction and Background**

## **Theory**



Much of the traditional thinking in condensed-matter physics has assumed that the solids and potentials created by their constituent atoms are periodic. This paradigm forms a basis for explaining many of the properties of solids, such as thermal and electrical conductivity due to the motions of phonons and electrons. Crystalline metals have high conductivities because the phonons and electrons, encountering a perfectly periodic potential created by the lattice, propagate as waves and are not bound to one atom in particular. Symmetry, too, can influence physical properties in obvious ways. The crystal-field splitting of transition metal ions in solids that gives color to many compounds, for example, depends directly on the local point symmetry at the lattice site where the ion is located; different symmetries lead to differently-colored materials.

Until 1984, only those symmetries compatible with periodicity, namely two-fold, three-fold, four-fold and six-fold rotational symmetry, were thought to be relevant to physical solids. In that year, materials that had diffraction patterns with crystallographically forbidden five-fold symmetry were discovered by Schectman.[31] As explained by Steinhardt and Levine[32], this was possible only by replacing periodicity with a new form of long-range order: quasiperiodicity. Two basis vectors in each dimension are required to describe the position of atoms in the quasicrystal structure, and electrons moving through the lattice no longer encounter a periodic potential. This has profound, though as yet not completely understood, consequences for quasicrystal physical properties. Quasicrystals composed of metals that when crystalline are highly conducting have an incredibly high electrical resistance.[41] Heating a crystalline metal introduces disorder into the lattice, interrupting the otherwise smooth motion of electrons and increasing electrical resistance.[10] By contrast, in a quasicrystal, introducing disorder by heating actually *decreases* electrical conductivity.[41] Unlike the soft crystalline metals, quasicrystal alloys are exceedingly hard and have a high degree of surface slipperiness, motivating the first commercial application of quasicrystals as a cookware coating alternative to teflon.[40] Most recently, the forbidden

symmetry of twelve-fold symmetric quasicrystals has been exploited to create novel photonic waveguides.[42].

In addition to periodicity and symmetry, physical properties also obviously depend on stoichiometry. To develop further novel materials with interesting physical properties, it is necessary to control both structure and chemistry. Many novel materials are found by beginning with a known phase and systematically varying its chemistry or symmetry until a material with interesting properties is created. The discovery of new crystals for diode-pumped lasers, for example, has depended on substituting a few different ions, most notably neodymium, into a family of related host structures. While in the case of most periodic materials, both symmetry and chemistry can be finely tuned, this is not generally the case with most of families of quasicrystals.

It is important for exploring physical properties and finding practical applications to have examples of quasicrystals with a wide variety of symmetries and compositions, but discovery of new quasicrystals up to this point has for the most part relied on the remarkably unsystematic process of serendipity. The original Schectman discovery of crystallographically-forbidden symmetry in aluminum manganese was an accident.[31] Subsequent discovery of the first perfect stable quasicrystal by Gayle, aluminum copper lithium, was similarly unexpected, found while looking for completely different phenomena.[34] Only *after* the diffraction pattern was seen to be five-fold symmetric was any thought given to quasicrystallinity. There are only a few different families of known quasicrystals, and of those, only the aluminum alloys and Zn-rare earth systems have been systematically explored. Only in these cases have any rules been developed to guide the search for new quasicrystals within the family.

There are several general ways to imagine finding new quasicrystals. One is to continue to develop new theory that might predict which real systems would be likely to be quasiperiodic. A second, adopted here, is a broadband empirical approach, systematically searching through existing data. The best way to identify quasicrystals is based on their diffraction properties, making obvious the crystallographically

forbidden symmetry that defines them. Unfortunately, no full three-dimensional catalogs of X-ray or electron diffraction patterns exist, and in general this is not the way in which materials are first identified. Instead, early phase and structure identification usually rely on *powder diffraction*. There does exist a comprehensive catalog of the powder diffraction patterns of about seventy thousand materials, known as the *Powder Diffraction File*. This file is now available in digital format.

The main goal of this thesis is to determine what can be learned about quasicrystals from their powder diffraction patterns. Whether quasicrystals can be identified based on their powder patterns alone is an open question. If this indeed is the case, one might apply the screening criteria used to identify quasicrystals to the full Powder Diffraction File to see if there are other materials, not known to be quasicrystals, that might be identified as such based on their powder patterns. A search scheme for quasicrystallinity based on powder diffraction patterns that yields new candidates for quasicrystals would be useful for several reasons. A naturally occurring quasicrystal has never been found and such a discovery would change the thinking about possible natural forces at work in mineral synthesis. Stoichiometries identified as either quasicrystalline or nearly quasicrystalline could provide a focus for systematic synthetic exploration in the laboratory. Because the Powder Diffraction File covers a huge range of materials, from natural minerals to synthesized organic phases to superconductors, there is a good chance that a successful test for quasicrystallinity will turn up interesting systems unrelated to the known quasicrystals.

There are a number of challenges to this project. It is not apparent *a priori* that even perfect quasicrystals can be identified from powder patterns. Their most distinctive feature, non-crystallographic symmetry, cannot be observed directly since the diffraction pattern has been collapsed into one-dimensional radial information. There may be crystals that mimic quasicrystalline behavior in powder patterns, and it is not known whether such “hoaxing” is common. Because quasicrystals occur within a fairly narrow stoichiometric range, it is also unclear how structures slightly

varying from the ideal quasicrystal range will appear in a powder pattern.

The project adopted the following broad outline. First, powder patterns of known, published quasicrystals in the Powder Diffraction File are studied to look for identifying features. A computerized search scheme is then devised to exploit these features and see if the quasicrystals can be extracted from the file. It is not obvious that such features exist, particularly since experimental errors and other distortions force any such program to allow some tolerance for every parameter; these tolerances might have to be so large that an overwhelming number of crystals are extracted with the known quasicrystals. Applying the scheme to the whole Powder Diffraction File renders a list of those compounds most likely to be quasicrystalline, which hopefully includes the known quasicrystals. After repeating this procedure of writing tests and looking at results a few times, some of the most promising candidate materials are examined in the lab to determine their structure. If they are not quasicrystalline, how they are fooling the search scheme is examined with the goal of improving the scheme itself, which is then applied again to yield a new list of candidates. This creates an iterative loop between the search scheme and laboratory investigation that will hopefully yield new quasicrystals. There are a number of symmetries in which quasicrystals can occur, but the most distinctive is the simple icosahedral structure in three dimensions. Consequently, this study focuses on searching for the simple icosahedral quasicrystal as a test of principle whether or not a reasonable search scheme can be constructed to identify quasicrystals based solely on powder diffraction data.

The thesis is organized into two parts. Part I, encompassing the first three chapters, surveys the background theory necessary to explain the search scheme. Chapter 1 reviews conventional crystallography, group theory, and the reasons why no five-fold rotational symmetry can be found in periodic crystals. Chapter 2 surveys diffraction, Fourier transforms, and general scattering for periodic solids. Chapter 3 is a review of the theory of quasicrystals and their diffraction behavior, with an emphasis on looking at quasicrystal lattices as projections of higher-dimensional periodic lattices

and some novel derivations. Part II describes the original work performed for this senior thesis. Chapter 4 describes the computerized search scheme devised to probe the Powder Diffraction File for quasicrystals and the results of those searches. Chapter 5 surveys the general electron microscopy techniques and methodology actually used in the laboratory phase of the investigation, though this chapter contains additional background material. Finally, chapter 6 describes the mostly preliminary results of our experimental investigation.



# Chapter 1

---

## The Rational Basis of Conventional Crystallography

“So there is nothing new under the sun. Is there anything of which one might say, ‘See this, it is new’? Already it has existed for ages which were before us.” [53]

The study of minerals and crystals is not new. Since antiquity people have been fascinated with the variety and properties of the natural materials around us. Part of this fascination surrounds the often obvious geometry of natural crystals which even at first glance separates them from other natural objects. Ideas that a crystal might be made up of many minuscule, identical bodies were subsequently introduced in an attempt to answer the natural question of how crystals formed. These two concepts, eventually formalized as symmetry and periodicity, are still the foundation for the modern approach to crystallography.

One of the triumphs of the modern theory of crystallography is the recognition that the atoms of a crystal can adopt only a finite number of arrangements. Only those symmetries compatible with periodicity are allowed; all other arrangements are *forbidden*. But to go from observing a crystal in hand to describing what shapes crystals simply *cannot* have involves a few steps in between, which are reviewed in the following brief overview of conventional crystallography.

## 1.1 An Historical Overview of Crystallography

The earliest written work pertaining to crystals is most likely Theophrastus's (372-288 B.C.) *de Lapidibus (On Stones)*. Primarily concerned with mining and the uses of various stones, he nonetheless gives descriptions of a fair number of the minerals with practical uses at the time.[7] But the major work of antiquity which would define mineralogy for the next millennium and a half was the final pair of books in the mammoth magnum opus of Pliny the Elder (23-79 A.D.), *Plinii Naturalis Historiae (Pliny's Natural History)*, completed in 77 A.D. Books 36 and 37 of *Natural History* survey minerals and precious stones. Although Pliny begins with a polemic against the extravagant uses of ornamental stone in luxury goods and later describes the formation of quartz as “moisture from the sky falling as pure snow,” he nevertheless makes the first recorded observations of quartz crystal geometry.

“Quare nascatur sexangulis lateribus, non facile ratio iniri potest, eo magis quod neque in mucronibus eadem species est et ita absolutus laterum levor est ut nulla id arte possit aequari.”

“It is not easy to explain why it is formed hexagonally; and even more, the terminations do not have identical appearance, and its faces are so completely smooth that no art could equal it.”<sup>1</sup>

His exceedingly comprehensive catalogue of the known minerals describes the geometry of octahedral diamonds as having “smooth faces meeting at six corners” and asserts that pyrite “always resembles small cubes.” Pliny also describes a so-called “rainbow stone,” most likely a quartz crystal showing colors by acting as a prism in sunlight:

“It is agreed that it is hexagonal, like quartz, but some other people argue that it has rough faces and unequal angles.”<sup>2</sup>

---

<sup>1</sup>My translation of Latin text in [3], guided by English translations in [3] and [4]

<sup>2</sup>Ibid.

Who those “other people” were and why they were arguing for unequal angles between the faces of a quartz crystal will likely remain a mystery. The debate over the constancy of interfacial angles was not entirely settled until Nicolaus Steno (Niels Stensen) measured the interfacial angles of a large number of quartz crystals, which he published in his 1669 *Prodromus*. Steno concluded that, irrespective of the shape or size of the faces of a crystal, the angles between them were the same.[30] The *Prodromus* included a series of detailed observations of quartz crystal growth, including that “the crystalline matter is not added to all the terminal planes at the same time, nor in the same amount;” this unequal growth led to significant differences in the shapes and sizes of a crystal’s faces, yet inexplicably still preserved the angles between those faces.[6]

Steno’s observations on the constancy of interfacial angles in quartz were extended to include all crystals in 1688 by Domenico Guglielmini (1655-1710).[8] But *why* should these angles be preserved when a crystal is only growing from one side? The notion of a crystal being constructed from identical subunits had been floating around for some time; perhaps the preservation of angles reflected some fundamental underlying geometry present in these subunits. Kepler had attempted to explain why snowflakes were invariably six-sided in his 1611 *Strena Seu de Nive Sexangula (A New Year’s Gift or the Six-Cornered Snowflake)* by postulating that they were composed of tiny spheres of ice. Although he discussed simple cubic, face-centered and body-centered cubic, and simple hexagonal packings, and further predicted some of the polyhedra that could be constructed from such packings, he was unable to explain the shape of snowflakes based on geometry alone.[5] The final unification of symmetry with the construction of crystals from smaller, repeating, identical units would have to wait another century.

In 1784, Réné Just Haüy published his “Essai d’une Théorie sur la Structure des Crystaux (Essay on the Theory of Crystal Structure)” in which he made the important advances that have earned him the title of founder of modern crystallography. The

book contains six plates vividly depicting the derivation of more complicated crystal forms from the simple cube, octahedron, dodecahedron, rhombohedron and hexagonal prism. The accompanying text demonstrates how all of the crystal forms can be constructed from a few simple types of symmetry and that a particular crystal form is created from a particular chemical composition. Considering the state of chemistry at the time—the discoveries of Priestley (oxygen), Lavoisie (nature of chemical reactions) and Cavendish (compound nature of water) were less than a decade old—this was a remarkable feat.

But perhaps even more remarkable was Haüy's deduction by observation of the “*Law of Rational Indices*” or “*Haüy's Law*”: that the distances along the three principal axes of a crystal intercepted by faces not parallel to these axes can be expressed as ratios of integers. The law's requirements greatly reduced the number of possible crystal forms, and the intercepts are related to the Miller indices (see section 2.5). Furthermore, by observing minerals with perfect cleavage, and breaking them into ever smaller pieces in which the geometry of the cleavage was preserved, Haüy also developed the concept of a fundamental subunit, which he termed the “*Molécules Intégrantes*”, composing and dictating the final geometry of the larger crystal. These *molécules intégrantes* were in turn composed of “*Molécules Elémentaires*,” the simple constituents composing a chemical compound, which Haüy postulated might have specific oriented positions within the *molécules intégrantes*. Thus was born the idea of a repeating unit cell, comprised of a group of specifically positioned atoms, whose geometry and composition would ultimate determine the overall symmetry and stoichiometry of a crystal.[8]

Haüy's ideas would be developed and formalized as mathematics, particularly through applying the group theory of Cauchy and others (see section 1.3), developed in first half of the nineteenth century. The biggest leap forward, though, came in the form of the elegant memoirs of August Bravais. In 1850, he presented his “*Mémoire sur les systèmes formés par des points distribués régulièrement sur un plan ou dan*

*l'espace' (Memoir on the Systems Formed by Points Regularly Distributed on a Plane or in Space)", establishing a precise quantitative framework for crystallography that remains more or less unchanged today.*

## 1.2 The Lattice

Bravais began his work by creating the concept of a lattice. To do so he used the following constructions. First, place an unlimited series of equidistant points along a line, creating a row. Then, place an infinite series of equidistant parallel rows in the same plane; in each row, designate one point a “starting point” and slide each row in the direction of its length until the starting points of each row fall on a straight line. This collection of rows in a plane is termed a net. To form a *lattice*, create an infinite series of equidistant parallel nets and slide each net so that all of the starting points now fall on a single plane; such a lattice is unlimited in its three dimensions. Bravais then describes a number of the properties of lattices, which he claims are “sufficiently evident to warrant no demonstration”:

“None of the individual points can be distinguished from any other by any uniqueness of relative position.

The configuration formed by the lattice, imagined unlimited, around any one of its points is the same, whatever the point selected. If, for instance, such a point is taken as the origin of an set of coordinates, rectangular or oblique, then around each such point taken successively as origin, other points are found similarly situated and with the same coordinates, provided only that in changing origins, the direction of the axes is preserved.”

“I postulate that these points are bound one to the other by forces such that the form of the entire lattice is invariable, all mutual distances remaining the same, although it is capable of being moved about in space

like a rigid body, either by translation, or by a rotation about a given axis, whenever it becomes necessary to impress upon it such movements.

If we give the entire system a movement of translation, a lattice point reaches the position which was previously occupied by another point, and all the other lattice points similarly reach positions in space previously occupied by other points of the system at the beginning of the motion. I then state that the locus of the lattice points has not been disturbed by the general movement impressed upon the lattice, or, in a simpler way, that there has occurred a restitution of the loci of lattice points.” [2]

Bravais thus formulated the modern notion of a lattice, which can be restated using the concept of vectors. Consider three fundamental translation basis vectors, one each for translation between adjacent points in a row, between starting points on adjacent rows within the same net, and between starting points on adjacent nets. Any point on the lattice can then be reached from any other point on the lattice by a translation comprised of a suitable *integral* linear combination of these basis translation vectors. And since all points are equal, we could have defined the lattice by starting with a single point and the three translation basis vectors; at every integral linear combination of these basis vectors we place an identical point. The resulting group of points would be a lattice entirely equivalent to that defined by Bravais above.

Generalizing to  $d$  dimensions, the position of any lattice point  $\vec{R}_l$  can be specified as an *integral* linear combination of linearly independent translation vectors  $\vec{a}_i$ :

$$\vec{R}_l = l_1 \vec{a}_1 + l_2 \vec{a}_2 + \cdots + l_d \vec{a}_d = \sum_{i=1}^d l_i \vec{a}_i \quad (1.1)$$

The vector  $\vec{l} = (l_1, l_2, \dots, l_d)$  is an index vector in  $d$ -dimensions, indexing the particular unit cell whose position is represented in  $d$ -dimensional real space by  $\vec{R}_l$ . A lattice is completely defined by the set of these translation vectors  $\vec{a}_i$ . Though there are an infinite number of different sets of  $\vec{a}_i$ , it is always possible to choose them such that they contain the shortest distance between two points in the lattice; the  $\vec{a}_i$  are

then called the set of *primitive translation vectors*. A general translation vector  $\vec{T}$  (also known as a lattice vector) is the vector between any two equivalent points on the lattice:

$$\vec{T} = \vec{R}_l - \vec{R}_{l'} \quad (1.2)$$

which of course is just another linear combination of the  $\vec{a}_i$ .

Since translating the lattice repeatedly by the same translation vector (which can be any combination of basis translation vectors) inevitably leads to the same original lattice, the lattice is said to be *periodic*. Moreover, the set of translation vectors  $\vec{T}$  is *closed* under all integral linear combinations; that is, for any translation vector  $\vec{T}_i$ :

$$\vec{T}' = \sum_i c_i \vec{T}_i$$

is another translation vector for any positive or negative integer  $c_i$ .

In real crystals, each lattice point is occupied by a repeating structural unit of one or more atoms called a *unit cell*. An infinite number of unit cells can be constructed in any given periodic lattice; the unit cell with the smallest volume is called the *primitive cell*. Another important unit cell is the *Wigner-Seitz cell*, which is defined for a given lattice point as the set of all points in space closer to that lattice point than any other lattice points. Constructing perpendicular bisecting planes of the lines drawn from a lattice point to all of its nearest neighbors, the smallest volume enclosed by that plane is the Wigner-Seitz cell.

When the unit cell contains multiple atoms, their positions relative to the lattice point in the unit cell are collectively known as the *basis*; the entire structure is then called a ‘lattice with a basis.’ Although formalized in more modern notation, the notion of the unit cell itself is little more than Haüy’s *molécules intégrantes*, an idea more than two hundred years old.

## 1.3 Symmetry and Groups

Bravais described many other aspects of lattices in general before focusing his attention on the special subset he called *symmetrical lattices*. He defined two symmetry elements, the rotational symmetry axis and plane of symmetry:

“I call axis of symmetry of a lattice any straight line such that, when the lattice rotates through a given angle and as one body about that axis, the same points of space coincide with the points of the lattice before and after the rotation. I say in this case that the apparent locus of the points of the lattice has been restored after this rotation.”

“Any plane which cuts a lattice into two geometrically symmetrical halves will be known as a plane of symmetry of the lattice.”

The modern formalism of operations such as rotation and reflection that leave objects unchanged is known as *group theory*. In general, a *group*  $G$  is a set of elements  $g_i$ , which can be operations or objects, subject to the following four conditions on group multiplication, quoted from [23]:

1. The product  $g_i g_j$  of any two group elements must be a group element.
2. Group multiplication is *associative*:  $(g_i g_j) g_k = g_i (g_j g_k)$ .
3. There is a unique group element  $g_1 = I$ , called the *identity*, such that

$$Ig_i = g_i I = g_i$$

for all  $g_i$  in  $G$ .

4. Each element has a unique *inverse*; that is, for each  $g_i$  there is a unique element  $g_i^{-1}$  such that

$$g_i g_i^{-1} = g_i^{-1} g_i = I$$

If group multiplication is *commutative* so that  $g_i g_j = g_j g_i$  for all pairs of elements in the group, then  $G$  is a commutative or *Abelian* group. When a subset  $S$  of the group  $G$  is itself a group,  $S$  is called a *subgroup* of  $G$ .[23]

The groups of interest in crystallography involve elements that are geometric operations performed on the lattice. The *Euclidean group* is the set of arbitrary rotations, reflections and translations.[14] The *symmetry group* is the subgroup of the Euclidean group that leaves a system unchanged; that is, the group whose operation creates a system *indistinguishable* from the original system.

To speak of indistinguishable rather than identical systems is relatively new; symmetry operations on systems were originally defined as generating *identical* systems. But in real systems with real atoms, there is no such thing as an identical system, due to thermal oscillation, quantum uncertainty, and other causes. The atoms of a fluid, for example, are randomly distributed throughout its volume, and were the position of each atom to be known exactly at a particular instant in time, there would be no apparent symmetry. On the other hand, the *average* environment of a given point in the fluid, it is identical to any other point in the fluid, so that, on average, the fluid is entirely isotropic and its symmetry group is the Euclidean group.[14] Similarly, if thermal oscillations and other uncertainties are ignored, the condition of indistinguishability for the average position of points in a lattice reduces to the condition of identity.

For a given fixed point  $O$  with a set of points around it, there are three types of operations that leave the point  $O$  unchanged and transform the points around it to a configuration indistinguishable from the original: *rotation* about an axis, *reflection* about a plane and *inversion* through a center of symmetry. Given a point whose position is represented by  $\vec{p}$  relative to a fixed origin, inversion is the operation that transforms  $\vec{p} \mapsto -\vec{p}$ , which Bravais also defined later in his *Mémoire*. Rotation, reflection and inversion are all subgroups of the symmetry group. The combinations of these operations that form subgroups of the symmetry group are known as “point

symmetry groups.” There are no inherent restrictions on the point symmetries of a collection of points; a sphere, for example, has an infinite number of rotation axes and reflection planes. But when those points must possess periodicity, as in a lattice, limitations appear.

## 1.4 Symmetry Restrictions due to Periodicity

Bravais was the first to recognize that imposing periodicity on a lattice restricted the types of symmetry it could have. After setting forth a definition of rotation axes, he characterized them in several ways, first by stating the theorem that the angle of rotation is a submultiple of 360 degrees. Then, most important for our purposes, Bravais stated the theorem restricting what those angles of rotation can be, in what has become known as the *crystallographic restriction*:

**“Theorem XLVI. A lattice can have only twofold, threefold, four-fold, or sixfold axes of symmetry.”**

If periodicity is not required, then a distribution of points can have any point symmetry. But once that distribution is required to be a periodic lattice, it can have only 2-, 3-, 4- and 6-fold rotation axes. Aside from the trivial asymmetric case of a 1-fold rotation axis, there are no other possible rotational symmetries.

Although Bravais gives a rigorous proof, a slightly clearer proof given by [22] is reproduced here (see figure 1.1).

$A$  is a point on the lattice, lying on an axis of symmetry perpendicular to the plane of the diagram.  $B$  is another lattice point separated from  $A$  by a possible translation, so that a similar symmetry axis must pass through  $B$ . If we rotate about the axis through  $A$  by an angle  $\phi = 2\pi/n$  (where  $n$  is an integer),  $B$  is carried to  $B'$ ; a similar rotation about the axis through  $B$  carries  $A$  to  $A'$ . Since  $A'$  and  $B'$  must be points on the lattice, the distance  $|A' - B'|$  must be a translational period of the lattice. If

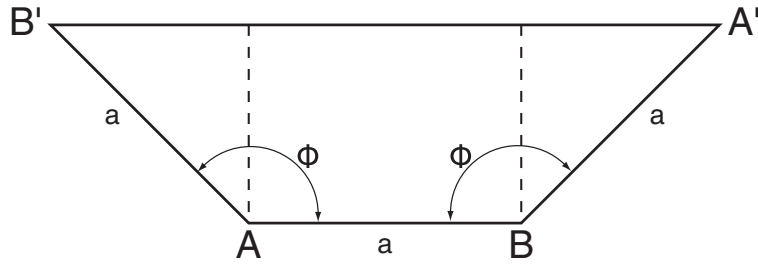


Figure 1.1: Restrictions on lattice symmetry due to the imposition of periodicity

the distance  $|A - B| = a$  is the shortest translation in the lattice,  $|A' - B'|$  must be equal to  $pa$  where  $p$  is an integer. From the geometry of the figure 1.1,

$$|A' - B'| = a + 2a \sin(\phi - \pi/2) = a - 2a \cos \phi = pa$$

simplifying,

$$\cos \phi = (1 - p)/2$$

Since  $|\cos \phi| \leq 1$ ,  $p$  can be 0, 1, 2 or 3. It can have no other value. Therefore,

$$\cos \phi = \frac{1}{2}, 0, \frac{-1}{2} \text{ or } -1$$

so,

$$\phi = \frac{\pi}{3}, \frac{\pi}{2}, \frac{2\pi}{3} \text{ or } \pi$$

and  $n$  can only equal 6, 4, 3, and 2. No other values (i.e. 5 or  $\geq 7$ ) are permitted.

One way to think about symmetries that are compatible with periodicity is to try tiling a bathroom floor with regular polygons. Twofold symmetry can be achieved with rectangles; threefold with triangles, fourfold with squares and sixfold with hexagons. But what about fivefold symmetry? The floor cannot be tiled with pentagons alone; “leftover” spaces remain (see figure 1.2).

Then what about those minerals that crystallize into dodecahedrons, like pyrite? A common habit is the so-called “pyritohedral” crystal, which indeed is a dodecahedron with twelve pentagonal faces (see figure 1.3). But closer inspection will reveal

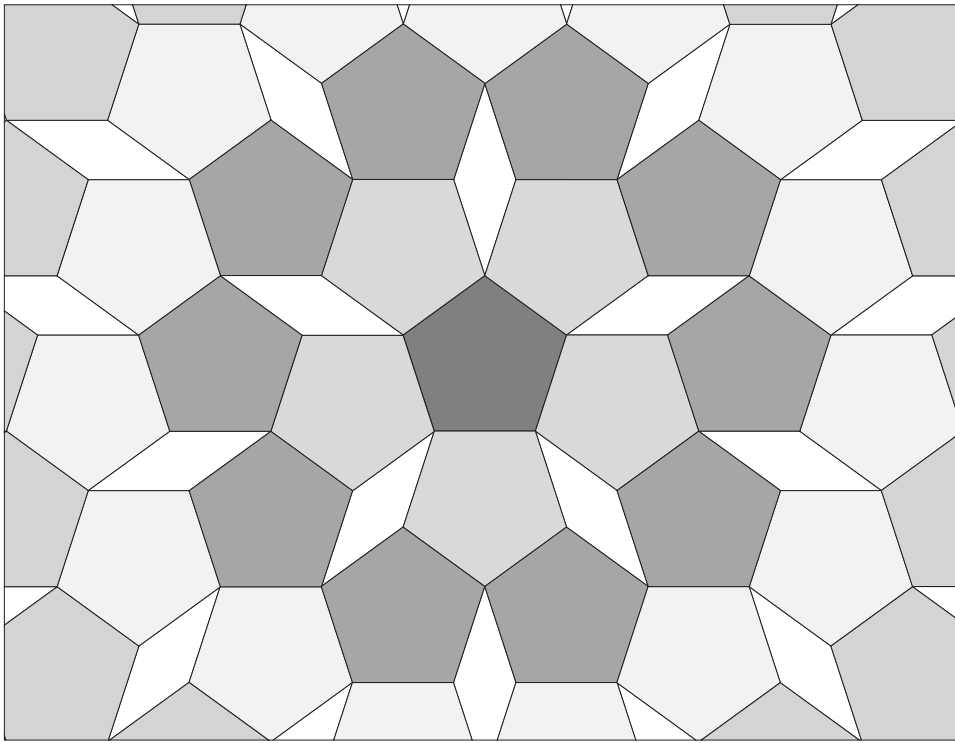


Figure 1.2: Attempted tiling of the plane with regular pentagons.

that these pentagons are *not regular* and hence possess no five-fold symmetry. In fact, the pyritohedral crystals are a perfectly fine example of cubic symmetry; the polyhedron can be created by replacing each of the six faces of the cube with two new faces at a slight angle from each other.

## 1.5 Space Groups

For a given point in a lattice, then, there are only 32 possible point groups. Using this finite set of possible point symmetries, Bravais was the first to classify the 14 unique types of point lattice possible in three dimensions; they now bear his name as the *Bravais lattices*. These Bravais lattices only summarize the geometry of the underlying periodic structure of identical repeating units, composed of one or more



Figure 1.3: Pyritohedral Pyrite crystals.

atoms, molecules, etc.[10]

The subgroup of the symmetry group that includes both point symmetry and translation is called the *space group*. In the case of the Bravais lattices, the space group is the product of the translation and point symmetry groups; any point symmetry can be combined with any arbitrary translation and the result will still be in the space group. This is called the *symmorphic* case. But an individual translation can be *combined* with an individual point symmetry operation to make an element of the space group, while individually that point operation and translation is not part of the group. This combination of elements leads to new elements such as the screw axis (rotation plus translation) and glide plane (plane of symmetry plus translation). Using all of these elements, there are 230 possible space groups. All materials with a periodic lattice, crystals for example, occur in one of these 230 space groups, with a basis of one or more atoms.[11]

Over the next 50 years, crystallography was extended by Federov, Schoenflies and others within the framework established by Bravais.[5] By the end of the Nineteenth Century, crystallographers could confidently pronounce that no crystal with a periodic lattice could possibly have five-fold external symmetry. Even today, there are no

natural crystals that are truly pentagonal or decagonal prisms, pentagonal dodecahedrons, icosahedrons or any other polyhedron with five-fold rotational axes. As the 20th century began, crystallographers had developed a highly successful scheme to classify the geometry and symmetry of practically all the known crystals. With the advent of new technology to probe the internal structure of these crystals, and thus demonstrate that Bravais's notion of a lattice was indeed the case, the triumph would seem even more complete.

# Chapter 2

---

## Diffraction, Scattering and the Fourier Transform

### 2.1 Classical Light Waves

The history of diffraction began with the study of light waves. In his 1690 *Traite de la Lumiere*, Christian Huygens first asserted that,

“each element of a wave-front may be regarded as the centre of a secondary disturbance which gives rise to spherical wavelets.”

and

“the position of the wave-front at any later time is the envelope of all such wavelets.” [20]

Unfortunately, the important notion that light could behave like a wave was suppressed for most of the eighteenth century because the most eminent scientist of the day, Isaac Newton, favored the ‘corpuscular’ theory, in which light was envisioned as a collection of small particles. It was not until 1801 that the wave theory was revived by the experiments of Thomas Young, who introduced the principle of interference: “if light from a source is divided by a suitable apparatus into two beams which are then superposed, the intensity in the region of the superposition is found to vary from

point to point between maxima which exceed the sum of the intensities in the beams, and minima which may be zero.”[12].

The ideas of Huygens and Young were unified in an 1818 memoir by Augustin Jean Fresnel, in which he argued what came to be known as the *Huygens-Fresnel Principle*: that secondary wavelets can interfere.

When light propagating through free space encounters an opaque screen with transparent holes in it, the light emerging at each hole can be regarded as the source of a new wave front. Far away from the screen, these sources will interfere to create the pattern of bright and dark spots called a *diffraction* pattern. The *Huygens-Fresnel Principle* is a powerful tool for calculating the often surprising diffraction patterns of sets of points. When Fresnel presented his theory to a prize committee of the French Academy of Sciences, S. Poisson argued that the theory had to be wrong since it could be shown to predict a bright spot in the center of the shadow of an opaque disk. The chairman of the committee, F. Arago, soon performed the experiment and, sure enough, found the predicted spot; Fresnel won the prize, though the effect was somewhat ironically named the “Poisson Spot.”[18] An early example of a startling diffraction pattern, it would not be the last.

## 2.2 Fraunhofer Diffraction of Classical Light Waves

The ability to interfere or diffract is perhaps the most distinguishing characteristic of waves; Feynman rightly states the impossibility of defining a difference between interference and diffraction[16]. Since the *Huygens-Fresnel Principle* is regarded as the “basic postulate of the wave theory of light,” [18] it is instructive to put this notion of diffraction on a more quantitative footing. [21] A plane wave

$$E = E_0 e^{i(kz - \omega t)} \quad (2.1)$$

is incident upon the  $x$ -axis, which is an infinite, opaque line at  $z = 0$ , and for convenience  $t = 0$  (see figure 2.1). The  $x$ -axis has a number of tiny holes poked in it;

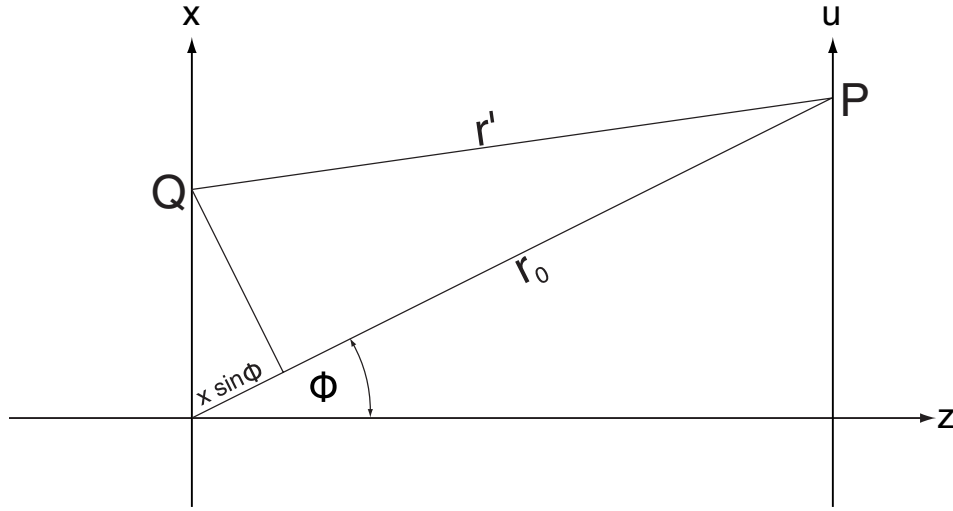


Figure 2.1: Fraunhofer (far-field) diffraction

one such hole is at the point  $Q = (x_0, 0)$ . By the *Huygens-Fresnel principle*, the light coming out of the tiny hole at  $Q$  will be a spherical wave:

$$E = E_0 e^{ikr} \quad (2.2)$$

with the wavevector  $k$  such that,

$$k = \frac{2\pi}{\lambda} \quad (2.3)$$

At point  $P$ , far away from the line at  $z = 0$ , along the  $u$ -axis, the amplitude of the wave originating at  $Q$  is

$$E_Q = E_0 e^{ikr'} = e^{\frac{2\pi i r'}{\lambda}} \quad (2.4)$$

where  $r' = |Q - P|$ . Summing up the contribution from the rest of the tiny holes *in phase*,

$$E_{tot} = \sum_{r'_n} E_0 e^{\frac{2\pi i r'_n}{\lambda}} \quad (2.5)$$

The region of interest is far away from the screen, in the so-called “far-field” region; that is, the distance between the source plane and its diffraction pattern is much greater than the size of the aperture, leading to the approximation:

$$r' \gg x_0$$

Known as the Fraunhofer approximation (yielding a ‘Fraunhofer’ or ‘far-field’ diffraction pattern), in practice this gives:

$$r'_n \cong r_0 - x_n \sin \phi \quad (2.6)$$

Substituting:

$$E_{tot} = \sum_{x_n} E_0 e^{2\pi i(r_0 - x_n \sin \phi)/\lambda} = E_0 e^{2\pi i r_0 / \lambda} \sum_{x_n} e^{-2\pi i x_n \sin \phi / \lambda} \quad (2.7)$$

Letting  $\frac{\sin \phi}{\lambda} \equiv u$ , and the constant  $C \equiv E_0 e^{2\pi r_0 / \lambda}$  leaves:

$$E = C \sum_{x_n} e^{2\pi i u x_n} \quad (2.8)$$

which is the discrete Fourier transform. In sum, based solely on classical arguments, it is clear that the Fraunhofer diffraction pattern of a distribution of points is simply the Fourier transformation of that distribution.

## 2.3 The Fourier Transform

Given a continuous function  $f(\vec{x})$ , the Fourier transform  $\Phi(\vec{u})$  of that function is defined as

$$\Phi(\vec{u}) = \int_{-\infty}^{+\infty} f(\vec{x}) e^{2\pi i \vec{u} \cdot \vec{x}} d\vec{x} \quad (2.9)$$

For a distribution of  $N$  discrete points  $x_n$ , the Fourier transform is a discrete sum:

$$\Phi(u) = \sum_{n=0}^N e^{2\pi i u x_n} \quad (2.10)$$

As an example, consider a one-dimensional lattice with lattice constant  $a$ , an infinite set of equidistant points a distance  $a$  apart, placed along the  $x$ -axis. This can be represented as a set of Dirac delta functions

$$f(x) = \sum_n \delta(x - na) \quad (2.11)$$

or, equivalently, as the discrete set

$$x_n = na \quad (2.12)$$

The diffraction pattern is determined by the Fourier transform:

$$\Phi(u) = \sum_n \int \delta(x - na) e^{2\pi i u x} dx = \sum_{x_n} e^{2\pi i u x_n} = \sum_n e^{2\pi i u n a} \quad (2.13)$$

which can be rewritten,

$$\sum_{n=-\infty}^{+\infty} e^{2\pi i u n a} = \sum_0^{+\infty} (e^{2\pi i u a})^n + \sum_0^{+\infty} (e^{-2\pi i u a})^n - 1 \quad (2.14)$$

Using the identity

$$\sum_0^\infty x^n = (1 - x)^{-1} \quad (2.15)$$

The sum can be rewritten:

$$\sum_{n=-\infty}^{+\infty} e^{2\pi i u n a} = (1 - e^{2\pi i u a})^{-1} + (1 - e^{-2\pi i u a})^{-1} - 1 \quad (2.16)$$

$$= \left( \frac{1 - e^{2\pi i u a} + 1 - e^{-2\pi i u a}}{1 - e^{2\pi i u a} + 1 - e^{-2\pi i u a}} \right) - 1 \quad (2.17)$$

$$= 0 \quad (2.18)$$

except at those points where

$$e^{\pm 2\pi i u a} = 1 \quad (2.19)$$

at which point the sum diverges. Taking the logarithm of both sides,

$$2\pi i u a = 2\pi n \quad (2.20)$$

$$\frac{n}{a} = u \quad (2.21)$$

where  $n$  is an integer. For values of  $u = n/a$ , the Fourier transform diverges, otherwise it is zero. This is just another infinite set of Dirac delta functions:

$$\Phi(u) = \sum_n e^{2\pi i n(u \cdot a)} = \sum_n \delta(u - n/a) \quad (2.22)$$

Thus the Fourier transform of a set of equally-spaced delta functions is another set of equally spaced delta functions.

## 2.4 General Scattering

The beginning of the twentieth century saw physics revolutionized by quantum mechanics. Newton's corpuscular theory would be resurrected with the realization that light, in addition to being a wave, could also be a particle. It was similarly realized that matter, traditionally thought of as particulate, can also behave as a wave. This notion was first formulated by Louis de Broglie in his "matter-wave hypothesis," that particles can act as waves with a wavelength of

$$\lambda = \frac{2\pi\hbar}{p} \quad (2.23)$$

where  $p$  is the particle's momentum. This naturally led to the idea that matter, too, can diffract, and the exploration of this idea required entrance into the realm of quantum mechanics. The following treatment of scattering is closely based on that given by [14].

According to a formula first obtained by P. A. M. Dirac and later dubbed by E. Fermi as the 'Golden Rule' of perturbation theory, the transition rate  $W$  from an initial state  $|\vec{k}\rangle$  to final state  $|\vec{k}'\rangle$  is[13]

$$W = \frac{2\pi}{\hbar} |U_{kk'}|^2 \rho_{k'}(E) \quad (2.24)$$

where  $\rho_{k'}(E)$  is the density of final states and the matrix element  $U_{kk'}$  is defined by

$$U_{kk'} = \langle \vec{k}|U|\vec{k}'\rangle = \int d\vec{x} e^{-i\vec{k}\cdot\vec{x}} U(\vec{x}) e^{i\vec{k}'\cdot\vec{x}} \quad (2.25)$$

$U(\vec{x})$  is the scattering potential, and

$$\langle \vec{x}|\vec{k}\rangle = e^{i\vec{k}\cdot\vec{x}} \quad (2.26)$$

is the unnormalized wavefunction. The differential cross section per unit solid angle of the final wave vector  $\vec{k}'$  is

$$\frac{d^2\sigma}{d\Omega} \propto \frac{2\pi}{\hbar} |U_{kk'}|^2 \quad (2.27)$$

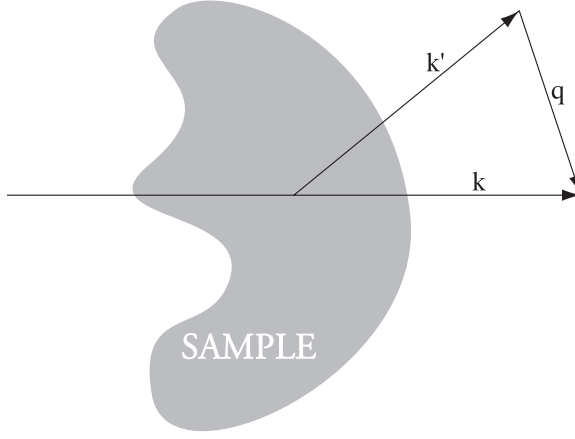


Figure 2.2: General scattering geometry, showing incident  $\vec{k}$ , final  $\vec{k}'$  and scattering  $\vec{q}$  wave vectors.

In systems of many particles,

$$U(\vec{x}) = \sum_i U_i(\vec{x} - \vec{x}_i) \quad (2.28)$$

is the total potential at  $\vec{x}_i$ , the position of the  $i$ th particle. The matrix element  $U_{kk'}$  is now equal to

$$U_{kk'} = \sum_i \int d\vec{x} e^{-i\vec{k}\cdot\vec{x}} U_i(\vec{x} - \vec{x}_i) e^{i\vec{k}'\cdot\vec{x}} \quad (2.29)$$

Substituting  $\vec{R}_i = \vec{x} - \vec{x}_i$ ,

$$U_{kk'} = \sum_i \int e^{-i\vec{k}\cdot(\vec{x}_i + \vec{R}_i)} U_i(\vec{R}_i) e^{i\vec{k}'\cdot(\vec{x}_i + \vec{R}_i)} d\vec{R}_i \quad (2.30)$$

$$= \sum_i \left( e^{-i\vec{q}\cdot\vec{R}_i} U_i(\vec{R}_i) d\vec{R}_i \right) e^{-i\vec{q}\cdot\vec{x}_i} \quad (2.31)$$

$$\equiv \sum_i U_i(\vec{q}) e^{-i\vec{q}\cdot\vec{x}_i} \quad (2.32)$$

where  $U_i(\vec{q}) \equiv \int e^{-i\vec{q}\cdot\vec{R}_i} U_i(\vec{R}_i) d\vec{R}_i$  is the Fourier transform of the particle potential and  $\vec{q} \equiv \vec{k} - \vec{k}'$  is the scattering wave vector. The general geometry of this scattering is shown in figure 2.2.

The differential cross section is thus proportional to

$$|U_{kk'}|^2 = \sum_{ii'} U_i(\vec{q}) U_{i'}^*(\vec{q}) e^{-i\vec{q}\cdot\vec{x}_i} e^{i\vec{q}\cdot\vec{x}_{i'}} \quad (2.33)$$

If all of the particles are identical, the cross section then becomes

$$\frac{d^2\sigma}{d\Omega} \propto |U_i(\vec{q})|^2 I(\vec{q}) \quad (2.34)$$

where

$$I(\vec{q}) = \sum_{ii'} e^{-i\vec{q}\cdot(\vec{x}_i - \vec{x}_{i'})} \quad (2.35)$$

$I(\vec{q})$  is called the *structure function*. When normalized by dividing by volume  $V$ , becomes the *structure factor*  $S(\vec{q})$ :

$$S(\vec{q}) = \frac{I(\vec{q})}{V} \quad (2.36)$$

The equations to this point are valid for any plane-wave state, including photons and electrons scattered elastically, in situations where single-scattering events dominate. When a plane-wave state scatters multiply through a sample, due to stronger interaction, the scattering behavior becomes more complicated.[14]

In the sample itself, the number density operator  $n(\vec{x})$  represents the number of particles per unit volume at a point  $\vec{x}$ :

$$n(\vec{x}) = \sum_i \delta(\vec{x} - \vec{x}_i) \quad (2.37)$$

For a lattice, following the notation in equation (1.1), this is

$$n(\vec{x}) = \sum_l \delta(\vec{x} - \vec{R}_l) \quad (2.38)$$

If the lattice has a basis of atoms of mass  $m_i$  located at positions  $\vec{c}_i$  within the unit cell, the mass density is

$$\rho(\vec{x}) = \sum_{l,i} m_i \delta(\vec{x} - \vec{R}_l - \vec{c}_i) \quad (2.39)$$

Because of thermal oscillations and crystal defects, this mass density itself is not strictly periodic; on the other hand, the ensemble average of this mass density, represented as  $\langle \rho(\vec{x}) \rangle$ , is periodic and invariant through all lattice translations:

$$\langle \rho(\vec{x}) \rangle = \langle \rho(\vec{x} + \vec{T}) \rangle \quad (2.40)$$

where  $\vec{T}$  is any general translation vector of the lattice, as defined in equation (1.2).

Of the various density correlation functions (ensemble averages of products of the number density operator taken at different points in space), the most important is the *two-point density-density correlation function*  $C_{nn}(\vec{x}_1, \vec{x}_2)$ :

$$C_{nn}(\vec{x}_1, \vec{x}_2) = \langle n(\vec{x}_1)n(\vec{x}_2) \rangle \quad (2.41)$$

$$= \left\langle \sum_{ii'} \delta(\vec{x}_1 - \vec{x}_i) \delta(\vec{x}_2 - \vec{x}_{i'}) \right\rangle \quad (2.42)$$

From equation (2.35) defining the structure function  $I(\vec{q})$ ,

$$I(\vec{q}) = \sum_{ii'} e^{-i\vec{q} \cdot (\vec{x}_i - \vec{x}_{i'})} \quad (2.43)$$

$$= \sum_{ii'} \int e^{-i\vec{q} \cdot (\vec{x}_i - \vec{x}_{i'})} \delta(\vec{x}_1 - \vec{x}_i) \delta(\vec{x}_2 - \vec{x}_{i'}) d\vec{x}_1 d\vec{x}_2 \quad (2.44)$$

$$= \int e^{-i\vec{q} \cdot (\vec{x}_1 - \vec{x}_2)} \left\langle \sum_{ii'} \delta(\vec{x}_1 - \vec{x}_i) \delta(\vec{x}_2 - \vec{x}_{i'}) \right\rangle d\vec{x}_1 d\vec{x}_2 \quad (2.45)$$

$$= \int e^{-i\vec{q} \cdot (\vec{x}_1 - \vec{x}_2)} C_{nn} d\vec{x}_1 d\vec{x}_2 \quad (2.46)$$

The structure function  $I(\vec{q})$  is the Fourier transform of the two-point density-density correlation function.  $I(\vec{q})$  can also be written,

$$I(\vec{q}) = \langle n(\vec{q})n(-\vec{q}) \rangle \quad (2.47)$$

where the Fourier transform of the density,  $n(\vec{q})$  is defined by

$$n(\vec{q}) = \int n(\vec{x}) e^{-i\vec{q} \cdot \vec{x}} d\vec{x} = \sum_i e^{i\vec{q} \cdot \vec{x}_i} \quad (2.48)$$

Thus, scattering is a measure of the density-density correlation function of a material.

## 2.5 The Reciprocal Lattice

For every periodic lattice there is an infinite set of equally-spaced parallel planes containing all lattice points (see figure 2.3). The planes  $\mathbf{G}$  can all be represented by

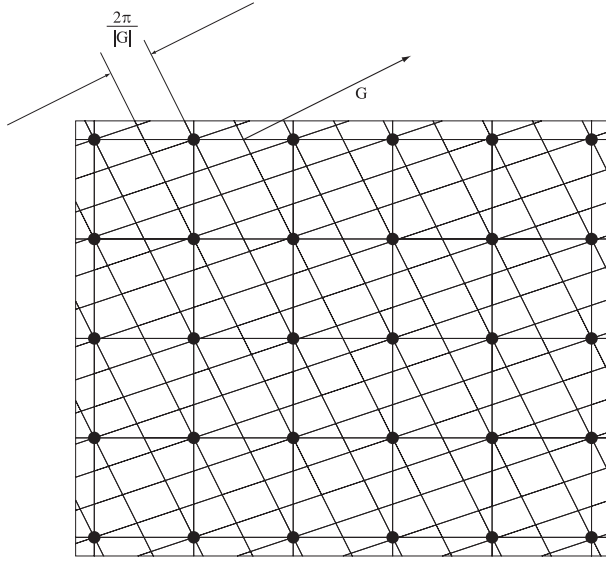


Figure 2.3: Lattice planes and a reciprocal lattice vector.

their normal vector  $\vec{G}$ . Lattice vectors  $\vec{T}$  in  $\mathbf{G}$  satisfy  $\vec{T} \cdot \vec{G} = \text{constant}$ , which we then assign:

$$\vec{T} \cdot \vec{G} = 2\pi n \quad (2.49)$$

where  $n$  is any integer. The selection of  $2\pi$  as the constant forces

$$e^{i\vec{T} \cdot \vec{G}} = 1 \quad (2.50)$$

Any point  $\vec{x}_n$  in the  $n$ th plane  $\mathbf{G}_n$  normal to  $\vec{G}$  follows the relation  $\vec{G} \cdot \vec{x}_n = 2\pi n$ , so that for points on adjacent planes  $\mathbf{G}_n$  and  $\mathbf{G}_{n+1}$ ,

$$\vec{G} \cdot (\vec{x}_{n+1} - \vec{x}_n) = 2\pi \quad (2.51)$$

The component of  $\vec{x}_{n+1} - \vec{x}_n$  parallel to  $\vec{G}$  is the interplanar spacing  $l$ , which therefore is

$$l = \frac{2\pi}{|\vec{G}|} \quad (2.52)$$

Consequently, for any set of primitive lattice translation vectors  $\vec{a}_i$ , there is always a set of *reciprocal lattice vectors*  $\vec{b}_i$  ( $i = 1, 2, \dots, d$ ) obeying the following relation:

$$\vec{a}_i \cdot \vec{b}_j = 2\pi\delta_{ij} \quad (2.53)$$

where  $i, j = 1, 2, \dots, d$ . Any arbitrary vector satisfying equation (2.49) can be written as a linear combination of these primitive translation vectors:

$$\vec{G} = \sum_i m_i \vec{b}_i \quad (2.54)$$

where the  $m_i$  can be any integer. Comparing with equation (1.1), it is clear that the set of vectors  $\vec{G}$  must also form a periodic lattice, which is called the *reciprocal lattice*.[14] Because of their geometric connection, the lattice planes  $\mathbf{G}$  can be indexed according to the vectors  $\vec{G}$  with *Miller indices*. The Miller indices of a lattice plane are simply the coordinates of the shortest reciprocal lattice vector normal to that plane.[10]

Any periodic function with a periodicity of the direct lattice can be expanded as a Fourier series using wavevectors in the reciprocal lattice:

$$f(\vec{x}) = \sum_G f(\vec{G}) e^{i\vec{G} \cdot \vec{x}} \quad (2.55)$$

Taking the Fourier transform of  $f(\vec{x})$ :

$$f(\vec{q}) = \int f(\vec{x}) e^{-i\vec{q} \cdot \vec{x}} d\vec{x} \quad (2.56)$$

$$= \sum_T \int_{UC} f(\vec{x} + \vec{T}) e^{-i\vec{q} \cdot (\vec{x} + \vec{T})} d\vec{x} \quad (2.57)$$

$$= \left( \sum_T e^{-i\vec{q} \cdot \vec{T}} \right) \int_{UC} f(\vec{x}) e^{-i\vec{q} \cdot \vec{x}} d\vec{x} \quad (2.58)$$

where  $\int_{UC}$  is integration over a single unit cell. For a lattice with  $N_c$  unit cells, the sum over  $\vec{T}$  is:

$$\sum_T e^{-i\vec{q} \cdot \vec{T}} = N_c \delta_{\vec{q}, \vec{T}} \quad (2.59)$$

If  $\vec{q}$  is a reciprocal lattice vector, then the  $\sum_T$  simply counts the number of unit cells. Otherwise the sum is zero; this is evident from equation (2.49). Substituting back into equation (2.58),

$$f(\vec{q}) = N_c v_0 \sum_G \delta_{\vec{q}, \vec{G}} f(\vec{G}) \quad (2.60)$$

where  $v_0$  is the volume of the unit cell. Since the  $\delta$  function forces  $\vec{q} = \vec{G}$ ,

$$f(\vec{G}) = \frac{1}{v_0} \int_{UC} f(\vec{x}) e^{-i\vec{G} \cdot \vec{x}} d\vec{x} \quad (2.61)$$

Equations (2.55) and (2.61) are applicable to any function of the real lattice  $f(\vec{x})$ . If we set  $f(\vec{x})$  equal to the mass density or, for example, the average number density,

$$\langle n(\vec{x}) \rangle = \sum_G \langle n(\vec{G}) \rangle e^{i\vec{G} \cdot \vec{x}} \quad (2.62)$$

it is clear that *the real and reciprocal lattices must be Fourier transforms of each other*. Also, since the direct lattice and reciprocal lattices are oriented in space, rotating the real lattice causes a concomitant rotation of the reciprocal lattice.

## 2.6 Bragg Scattering

The scattering potential defined by equation (2.25) can also be expressed in terms of the reciprocal lattice vectors:

$$U_{kk'} = V \sum_G U(\vec{G}) \delta_{\vec{q}, \vec{G}} \quad (2.63)$$

So that the scattering cross section given in equation (2.27) becomes:

$$\frac{d^2\sigma}{d\Omega} \propto |U_{kk'}|^2 = V^2 \sum_G |U(\vec{G})|^2 \delta_{\vec{q}, \vec{G}} \quad (2.64)$$

By equation (2.34), it is apparent that the  $\delta$ -function is the structure function. In a real lattice the mass at each point is represented by a  $\delta$ -function, so that the overall mass density is a periodic series of  $\delta$ -functions. The two-point density-density correlation function is then another series of delta functions. From the result derived

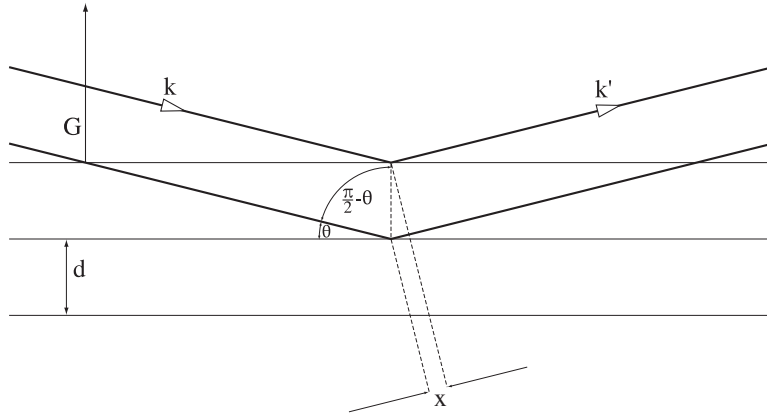


Figure 2.4: Bragg Scattering

in section 2.3, the Fourier transform of a periodic set of  $\delta$ -functions is another set of  $\delta$ -functions; the structure function should therefore be a set of  $\delta$ -functions, which is exactly what emerges.

Consequently, there will be peaks (i.e. the scattering cross section will be large) in the scattering (diffraction) pattern for every scattered wavevector  $\vec{q} = \vec{k} - \vec{k}'$  equal to a reciprocal lattice vector  $\vec{G}$ . These are known as the *Bragg peaks* of the diffraction pattern. In the present case of elastic scattering,  $|\vec{k}| = |\vec{k}'|$ . Setting  $\vec{q} = \vec{G}$ ,

$$\vec{k} - \vec{k}' = \vec{G} \quad (2.65)$$

$$\vec{k}' = \vec{k} - \vec{G} \quad (2.66)$$

$$|\vec{k}'|^2 = |\vec{k}|^2 + |\vec{G}|^2 - 2\vec{k} \cdot \vec{G} \quad (2.67)$$

$$\vec{k} \cdot \left( \frac{\vec{G}}{2} \right) = \left| \frac{\vec{G}}{2} \right|^2 \quad (2.68)$$

The scattering geometry is depicted in figure 2.4. From figure 2.3, the quantity  $|\vec{G}|/2\pi$  for one particular reciprocal lattice vector is equal to the interplanar spacing, represented by  $d$ ; the term  $d$ -spacing is common in the crystallographic literature, and refers to the real space separation of lattice planes. Therefore,

$$|\vec{G}| = \frac{2\pi}{d}$$

The magnitude of wavevector  $\vec{k}$  by definition obeys the following relation:

$$|\vec{k}| = \frac{2\pi}{\lambda}$$

where  $\lambda$  is the wavelength. Therefore:

$$\vec{k} \cdot \left( \frac{\vec{G}}{2} \right) = \left| \frac{\vec{G}}{2} \right|^2 \quad (2.69)$$

$$|\vec{k}| \left| \frac{\vec{G}}{2} \right| \cos \left( \frac{\pi}{2} - \theta \right) = \left| \frac{\vec{G}}{2} \right|^2 \quad (2.70)$$

$$\frac{2\pi}{\lambda} \cos \left( \frac{\pi}{2} - \theta \right) = \left| \frac{\vec{G}}{2} \right| \quad (2.71)$$

$$\frac{2\pi}{\lambda} \sin \theta = \frac{\pi}{d} \quad (2.72)$$

$$2d \sin \theta = \lambda \quad (2.73)$$

Of course, there are other reciprocal lattice vectors  $\vec{G}_i$ , so that the general form of equation (2.73) is:

$$2d \sin \theta = n\lambda \quad (2.74)$$

where  $n$  is any integer. This is the celebrated *Bragg's law*, which can also be derived with a simpler, though certainly less rigorous, argument. Consider plane waves with wavevector  $\vec{k}$  incident upon a set of parallel planes separated by  $d$ . Assuming specular reflection (that is, the angle of incidence  $\theta$  equals the angle of reflection), constructive interference will occur only if the path length difference between rays reflected from different planes ( $2x$  in figure 2.4) is equal to an integral number of wavelengths  $n\lambda$ . Since  $x = d \sin \theta$ , the total path length difference is twice that, which gives equation (2.74) again.

As the general structure function  $I(\vec{q})$  is a Fourier transform of the two-point density-density correlation function, it quantifies the effects of a multi-atom basis within a unit cell.  $I(\vec{q})$  as given in equation (2.35) assumes a monatomic basis; contributions from different atoms will require different coefficients  $f(\vec{x}_i)$  for different

terms in the sum, but the form remains the same sum of phase factors from different atoms in the basis.

$$I(\vec{q}) = \sum_{ii'} f(\vec{x}'_i) e^{-i\vec{q} \cdot (\vec{x}'_i - \vec{x}'_{i'})} \quad (2.75)$$

Under certain circumstances, these phase factors can cancel, causing the structure factor to be zero as a result of either placement or type of atoms in a basis; this is known as an extinction. The structure factor has the ability to modulate the intensity of a diffraction pattern, but does not otherwise change the positions of the peaks.

The condition for seeing a diffraction pattern according to Bragg's law is

$$\lambda \leq 2d$$

Physically this may be better understood with a classical analogy by idealizing the lattice as a set of delta functions. When the characteristic spacing  $d$  is significantly larger or smaller than  $\lambda$ , there will be a forest of delta functions too close to be distinguished, or they will be spaced extremely far apart. These situations correspond to the incident waves either passing through essentially unimpeded (points too far apart to make a significant difference) or getting absorbed (points too close together). In both extreme cases, no diffraction pattern is observed.

The typical spacing between atoms in a crystal is on the order of 1 Å, and since this is also the order of the wavelength of X-rays, X-rays diffract through atoms. At the suggestion of Max von Laue, the father-son pair of William Henry and William Lawrence Bragg found in 1913 that crystalline substances would diffract X-rays. Unlike those of liquids, the diffraction patterns of crystalline materials were entirely composed of discrete and intense spots, which, of course, are now appropriately named *Bragg peaks*. The Braggs developed the law that bears their name to explain diffraction results using only the classical physics available at the time.

Of course matter can also diffract, and combining the de Broglie relation  $\lambda = h/p$  with the classical expression for energy  $E = p^2/2m$ ,

$$E = \frac{h^2}{2m\lambda^2} \quad (2.76)$$

For an electron of mass  $m_e$ , the energy corresponding to a wavelength of 1 Å is about 150 eV. The first experimental observation confirming the wave-like nature of electrons (and de Broglie's hypothesis) was the diffraction of electrons off a nickel crystal surface by Davisson and Germer in 1925.[17],[19]

## **2.7 X-ray and Electron Diffraction**

The full view of the reciprocal lattice required to be able to reconstruct the full real lattice involves varying  $\vec{q}$ , the scattered wavevector, though a large portion of reciprocal space. But since  $\vec{q}$  has three components of direction and cannot be varied directly like the incident wavevector  $\vec{k}$ , there is no easy way to image the full three-dimensional reciprocal lattice at one time, only projections in lower dimensions. In principle, either the wavelength or direction of  $\vec{k}$  can be varied to allow a range of  $\vec{q}$ , but without a synchrotron radiation source, there is no convenient way to vary  $\lambda$  in a controlled manner for X-rays. Since almost all X-ray radiation is produced by sharply defined fixed atomic transitions, varying the direction of  $\vec{k}$  is the only remaining way to vary  $\vec{q}$  and map the reciprocal space. It is similarly much easier to vary the direction of an electron beam than its wavelength.

Although many diffraction methods can be used to determine symmetry and structure, in this thesis we use only three: X-ray powder diffraction, electron diffraction through thin samples in the transmission electron microscope, and electron diffraction from the surface of thick samples in the scanning electron microscope. A brief overview of these techniques in light of diffraction theory is included here, while the experimental details involved in actually collecting the data are included in chapter 5.

### 2.7.1 One-Dimension: Powder X-ray Diffraction

In powder diffraction, a sample is pulverized into myriad micron-scale grains, still vast enough on the atomic scale to diffract X-rays. The powdering process presents an average reciprocal lattice that is randomized in direction; in effect, it is as if the original reciprocal lattice were rotated through all possible angles. Each point at  $\vec{G}$  is replaced by a spherical shell of radius  $|\vec{G}|$ . All directional information has been removed. Data collection then measures only the magnitude of the scattering vector,  $|\vec{q}|$ .[10]

In a typical modern setup in an X-ray powder diffractometer,  $\vec{k}$  is fixed in both magnitude and direction, and  $\vec{k}'$  is determined by measuring the intensity as a function of the scattering angle  $\theta$ . From Bragg's law,  $\theta$  is converted into a series of d-spacings; the magnitude of the reciprocal lattice vectors  $\vec{G}$  are then found from  $|\vec{G}| = 2\pi/d$ .

Because all directional information has been lost, there are often several reciprocal lattice vectors of the same magnitude. Reconstructing the structure then requires that a good deal of information be inferred, since the symmetry cannot directly be observed.

### 2.7.2 Two-Dimensions: Single-Crystal Diffraction

By looking at a two-dimensional diffraction pattern, the symmetry of a sample can be observed. One way to accomplish this is to fire a beam of X-rays or electrons along a rotational axis of symmetry and record the far-field diffraction pattern on a piece of film. By repeating this for every symmetry axis of the crystal, a more or less complete picture of its structure can be deduced.

Because electrons interact more strongly than X-rays with matter, multiple scattering will occur in samples thicker than a micron. Electrons can diffract through thin samples. This is often accomplished inside a transmission electron microscope (TEM) by powdering a sample into small grains, then searching through these grains for thin, electron-transparent regions. Orientation to find axes of symmetry is accomplished

by tilting the stage holding the sample, though this can be rather time-consuming and tedious.

A second method is to send a beam of electrons into thick samples in a scanning electron microscope (SEM). Among the many possible things that can happen (see chapter 5), some of the electrons penetrating deeply into the sample can multiple-scatter diffusely and then reemerge as so-called backscattered electrons. If a screen is set up to image these electrons, it will show a nearly uniform background, since the multiple-scattering causes these backscattered electrons to have a random angular distribution, except for a pattern of dark lines. The lines, called Kikuchi bands, represent those electrons which Bragg-scatter within the lattice and thus do not reemerge.[45]

## 2.8 Diffraction and Symmetry

Because the real and reciprocal lattices are Fourier transforms of each other, group operations performed on the real lattice that leave it invariant will, when performed on the reciprocal lattice, also leave it invariant. Because the diffraction pattern is a map of the reciprocal lattice, then, the pattern should reflect the symmetry of the reciprocal lattice and therefore of the real lattice. Consequently, a major goal of taking diffraction patterns is to determine the original real-space symmetry and therefore the structure of a given material.

In defining symmetry and considering the effect of group operations on a lattice, one can choose in which space to define it, real or reciprocal. For reasons that will be discussed in the next chapter, it is most convenient to define symmetry in reciprocal space, in accordance with Mermin.[29] Symmetry group operations in reciprocal space will leave a lattice *identical* to its original counterpart, while real space operations will only leave the lattice indistinguishable. In periodic crystals, the distinction is meaningless, as the symmetry of real and reciprocal spaces is the same, and group operations always leave the lattice identical to the original.

Nevertheless, at least for crystals, the crystallographic restriction stated in section 1.4 should certainly still apply. Only two-fold, three-fold, four-fold or six-fold rotational symmetry should occur in either the diffraction pattern or the real crystal.



# Chapter 3

---

## Quasicrystals

### 3.1 The Quasilattice

The relation defining a lattice was given in equation (1.1) as:

$$\vec{R}_l = l_1 \vec{a}_1 + l_2 \vec{a}_2 + \cdots + l_d \vec{a}_d = \sum_{i=1}^d l_i \vec{a}_i$$

Any integer linear combination of these basis vectors  $a_i$  will form a vector that is in the lattice. A  $d$ -dimensional periodic lattice has  $d$  integer linearly independent basis vectors.

The concept of a lattice in  $d$  dimensions can be extended to have  $d' \equiv d + n$  basis vectors; that is,  $d + n$  vectors that are integer linearly independent. The construction forms a *quasilattice*. A periodic lattice thus becomes the special case of a quasilattice where  $d' = d$ . Much of the framework developed to describe lattices and their projections can be applied to quasilattices.

If each point on the lattice is represented by a delta function, then the two-point density-density correlation function will also be a set of delta functions with the same support as the lattice itself, up to a scale factor. It was shown in section 2.3 that the Fourier transform of a periodic set of delta functions is another set of periodic delta functions. For a crystal, its two-point density-density correlation function is a periodic set of delta functions with support on the lattice. As described in section

2.6, the Fourier transform of the correlation function, the structure function, will also be a set of delta functions.

A quasilattice, too, has a structure function composed of delta functions. As an example, the derivation given in section 2.3 is extended to include more than one basis vector per dimension. Consider a one-dimensional lattice composed of a delta peaks  $f(x) = \sum_n \delta(x - x_{n,m})$  where  $x_{n,m}$  is now characterized not by a single integer, as in equation (2.12), by the two integers  $n$  and  $m$ :

$$x_{n,m} = (n + m\tau)a = na + m\tau a \quad (3.1)$$

where  $a$  is the lattice constant, and  $\tau$  is an irrational number, making  $n$  and  $m\tau$  relatively irrational. The discrete Fourier transform is:

$$\begin{aligned} \Phi(u) &= \sum_{n=-\infty}^{+\infty} \sum_{m=-\infty}^{+\infty} e^{2\pi i u(n+m\tau)a} \\ &= \sum_{n=-\infty}^{+\infty} \sum_{m=-\infty}^{+\infty} (e^{2\pi i ua})^n (e^{2\pi i u\tau a})^m \\ &= \left( \sum_{n=0}^{+\infty} (e^{2\pi i ua})^n + \sum_{n=0}^{+\infty} (e^{-2\pi i ua})^n - 1 \right) \left( \sum_{m=0}^{+\infty} (e^{2\pi i u\tau a})^m + \sum_{m=0}^{+\infty} (e^{-2\pi i u\tau a})^m - 1 \right) \end{aligned}$$

Using the identity in equation (2.15),

$$\Phi(u) = \left[ (1 - e^{2\pi i ua})^{-1} + (1 - e^{-2\pi i ua})^{-1} - 1 \right] \left[ (1 - e^{2\pi i u\tau a})^{-1} + (1 - e^{-2\pi i u\tau a})^{-1} - 1 \right] \quad (3.2)$$

which simplifies to,

$$\Phi(u) = \left( \frac{1 - e^{2\pi i ua} + 1 - e^{-2\pi i ua}}{1 - e^{2\pi i ua} + 1 - e^{-2\pi i ua}} - 1 \right) \left( \frac{1 - e^{2\pi i u\tau a} + 1 - e^{-2\pi i u\tau a}}{1 - e^{2\pi i u\tau a} + 1 - e^{-2\pi i u\tau a}} - 1 \right) \quad (3.3)$$

This is always equal to zero, unless one of the following two equations is satisfied, at which point equation 3.3 diverges:

$$e^{\pm 2\pi i ua} = 1 \quad (3.4)$$

$$e^{\pm 2\pi i u\tau a} = 1 \quad (3.5)$$

The Fourier transform is therefore another set of delta functions of the general form  $\Phi(u) = \delta(u - u')$ , where

$$u'_{N,M} = \frac{1}{a} \left( N + \frac{M}{\tau} \right) \quad (3.6)$$

The reciprocal lattice of a one-dimensional quasilattice is therefore another quasilattice:

$$\Phi(u) = \sum_{n,m} e^{2\pi i u(n+m\tau)a} = \sum_{N,M} \delta \left( u - \frac{1}{a} (N + M/\tau) \right) \quad (3.7)$$

To clarify the discussion, a set of formal definitions is introduced, based on those given in [32]. Any structure whose structure function (the Fourier transform of its two-point density-density correlation function) is a discrete set of Bragg peaks is a *translationally ordered structure*. Without long-range translational order, for example in a liquid, the structure function is no longer discrete. All crystals clearly fall under this category, as do the quasilattices. From section 2.6, the Bragg peaks of a translationally ordered structure will be centered at a discrete set of vectors  $\{\vec{G}_i\}$ . This set of vectors  $\{\vec{G}_i\}$  is the *reciprocal lattice*. If there is a finite set of vectors  $\{\vec{q}_n\}$  such that each vector  $\vec{G}_i$  in the reciprocal lattice can be expressed as an integer linear combination of the  $\vec{q}_n$ , then the smallest set of vectors  $\{\vec{q}_n\}$  is a *basis set of reciprocal vectors*. Each  $\vec{q}_n$  is a *reciprocal lattice basis vector*. The number of vectors in the basis set is the *rank* of the reciprocal lattice.

A *d*-dimensional *crystal* is a translationally ordered structure with rank of *d*. A *quasiperiodic structure* is a translationally ordered structure whose rank *d'* exceeds *d*.

## 3.2 From Quasilattice to Quasicrystal

Perhaps the reason why quasilattices were not considered as related to atomic systems prior to 1984 was the fact that, for  $d' > d$ , there is no longer any minimum separation distance between lattice points. Between every two points in the quasilattice is another lattice point. Since atoms have finite size, a model with atoms lying at each quasilattice site is unphysical. The way around the problem is to introduce

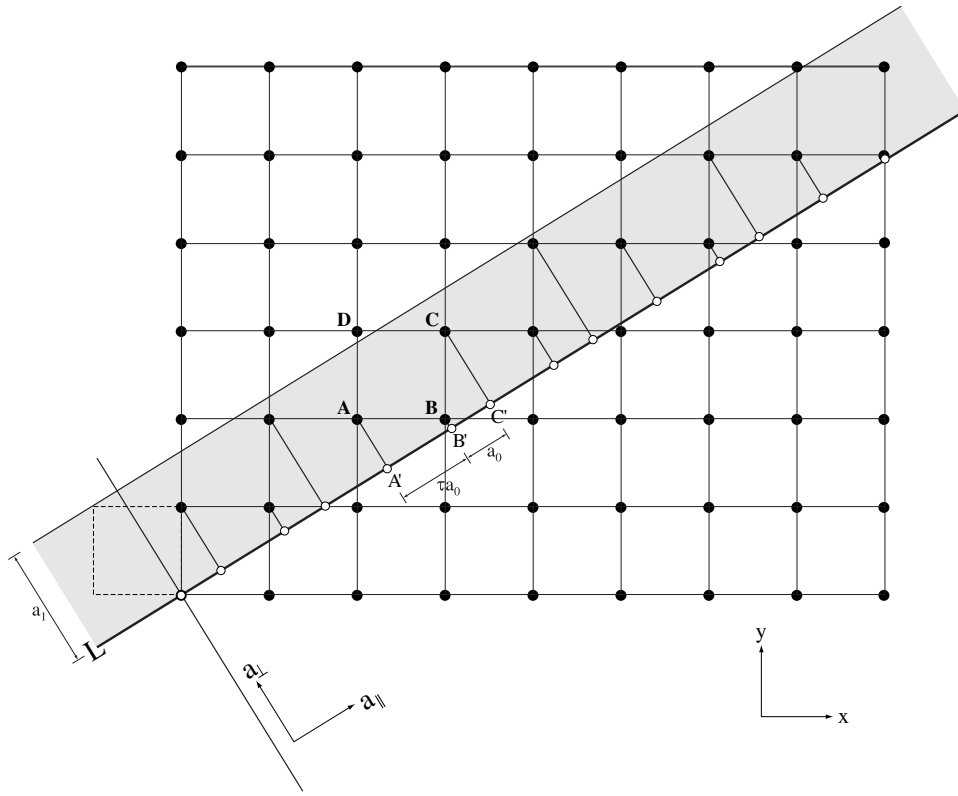


Figure 3.1: Projection of a two-dimensional square lattice onto a line of irrational slope, creating a one-dimensional quasilattice.  $A'$ ,  $B'$  and  $C'$  are the projections of  $\mathbf{A}$ ,  $\mathbf{B}$  and  $\mathbf{C}$  along  $a_{\parallel}$ .  $|B' - C'|$  has length  $\Delta a_{\parallel} = a_0$ ;  $|A' - B'|$  has length  $\Delta a_{\parallel} = \tau a_0$ . The window (gray bar) has width  $\Delta a_{\perp} = a_1$ .

some selection criteria which place atoms at a subset of quasilattice points while still maintaining the symmetry. One method for envisaging the selection rule is by using the relation between quasilattices and periodic lattices in higher dimensions.

### 3.2.1 Projection

A  $d$ -dimensional quasilattice can be thought of as a  $d'$ -dimensional regular lattice projected down into  $d$  dimensions. For example, a one-dimensional quasilattice can be constructed by projecting a two-dimensional square lattice onto a line of irrational slope, as illustrated in figure 3.1.

The slope of the line  $L$  has been chosen to be  $1/\tau$ , where  $\tau \equiv (1 + \sqrt{5})/2$  is the Golden Ratio. The square lattice has points for all integer  $x$  and  $y$ ; in the rotated coordinate system, points of the square lattice are projected parallel to  $a_{\perp}$  onto the line of slope  $1/\tau$ ; the coordinate for distance along that line is  $a_{\parallel}$ . Because of the irrational slope, line  $L$  will intersect at most one lattice point (here selected arbitrarily to be the origin). If all points on the lattice are projected, the points on the line  $L$  will have no minimum separation.

To create a selection rule, a window is introduced (the gray bar in the figure), which extends to infinity in  $a_{\parallel}$  but is finite in  $a_{\perp}$ . Only those lattice points which are inside the window are projected onto the line and become part of the quasilattice. In figure 3.1, the points marked **A**, **B** and **C** are projected onto the line at  $A'$ ,  $B'$  and  $C'$ , respectively. Point **A** is outside the window, and hence is not projected. The height of the window has been selected so that its projection on  $a_{\perp}$  is the projection of the unit square. It turns out that all distances between neighbors on  $L$  are either  $a_0$  or  $\tau a_0$ , where  $a_0$  is the projection of  $\hat{y}$  and  $\tau a_0$  is the projection of  $\hat{x}$  on  $a_{\parallel}$ . Every point in the one-dimensional quasilattice along  $L$  can thus be described by a suitable integer linear combination of the two basis vectors, whose relative length is  $\tau$ :

$$a_{\parallel n,m} = (n + \tau m)a_0 \quad (3.8)$$

Because of the window,  $n$  and  $m$  are now restricted to a certain set of values. The set of points along  $L$  projected from within the window meet the conditions necessary for a real atomic system: a minimum distance between points  $a_0$ , and a finite number of different types of separations (i.e. 2). The set of points is thus a quasiperiodic ‘crystal’—a *quasicrystal*. The formal definition of a quasicrystal involves its rotational symmetry, which will be discussed below; for the one-dimensional case, rotational symmetry has no bearing so the definition still applies.

Without the window, the projected lattice would be a simple quasilattice and it follows immediately from section 3.1 that the reciprocal lattice and hence the diffraction pattern would be another quasilattice. Introducing the window fundamentally

changes little. The new diffraction pattern will depend on the Fourier transform of the window function. The directions in reciprocal space corresponding to  $a_{\parallel}$  and  $a_{\perp}$  in real space are  $Q_{\parallel}$  and  $Q_{\perp}$ , respectively;  $L$  transforms to  $L'$ . The window function  $W(a_{\parallel}, a_{\perp})$  is defined as:

$$W(a_{\parallel}, a_{\perp}) = 1 \quad (-\infty < a_{\parallel} < +\infty, \quad 0 < a_{\perp} < a_1) \quad (3.9)$$

$$= 0 \quad (\text{otherwise}) \quad (3.10)$$

where  $a_1$  is a constant. The two-dimensional Fourier transform has components in both  $Q_{\parallel}$  and  $Q_{\perp}$  directions. Along  $Q_{\parallel}$ , the window function is constant.

Along  $Q_{\perp}$ , the “top-hat” function will transform into a so-called “sinc” function.

Setting  $a_1 = 1$  for convenience:

$$\Phi(Q_{\perp}) = \int_{\infty}^{+\infty} W(a_{\perp}) e^{iQ_{\perp}a_{\perp}} da_{\perp} \quad (3.11)$$

$$= \int_0^1 e^{iQ_{\perp}a_{\perp}} da_{\perp} \quad (3.12)$$

$$= \frac{e^{iQ_{\perp}} - 1}{iQ_{\perp}} \quad (3.13)$$

The diffraction pattern observed will be proportional to  $|\Phi(Q_{\perp})|^2$ :

$$\left| \frac{e^{iQ_{\perp}} - 1}{iQ_{\perp}} \right|^2 = \frac{2 - 2 \cos Q_{\perp}}{Q_{\perp}^2} = \left( \frac{\sin \frac{Q_{\perp}}{2}}{\frac{Q_{\perp}}{2}} \right)^2 \equiv \left( \text{sinc} \frac{Q_{\perp}}{2} \right)^2 \quad (3.14)$$

Unlike the top hat function, the sinc function is smooth, continuous and has a relatively small number of zeroes.

A well-known theorem in Fourier analysis is that the Fourier transform of a convolution of two functions is the product of the Fourier transforms of those two functions. The final diffraction pattern of the set of square lattice points projected from within a window will be the product of the Fourier transforms of the window function and the lattice. The Fourier transform of the square lattice is simply another square lattice. The Fourier transform of the top hat window function is a smooth sinc function. The product of the two functions is a square lattice no longer with equal intensity at each point, but a modulation of intensities due to the sinc function. However,

there is finite magnitude of the delta functions in the reciprocal space all the way out to infinity in both  $Q_{\parallel}$  and  $Q_{\perp}$ . That is, the reciprocal space corresponds to having non-zero intensity at practically all points of a quasilattice. The real space—by our introduction of a window function with compact support—only has non-zero atomic density at a subset of quasilattice points. While the real-space projected set of points is a quasicrystal with a minimum separation between points, the reciprocal-space projected set of points is a quasilattice with no minimum separation. This asymmetry between real and reciprocal spaces has significant consequences for the point symmetry of quasicrystals, discussed in section 3.3.

### 3.2.2 Phonons and Phasons

The position of the window in figure 3.1 is arbitrary. When the window is moved to a different location, the set of points projected onto  $L$  will change. There are two possible movements: along  $a_{\parallel}$  and along  $a_{\perp}$ . Shifting the projected lattice along  $a_{\parallel}$  is merely a uniform displacement, called a *phonon shift* because it corresponds to the uniform shifts of regular lattices, essentially the action of a phonon. The lowest order phonon in the coupled oscillations of a real lattice is an equal translation of all points, identical to a shift along  $a_{\parallel}$  here. The atoms in a real system do not change their relative locations in a phonon shift.

Shifts along  $a_{\perp}$ , on the other hand, have no obvious counterpart in periodic crystals. By changing the location of the window function, different lattice points fall within the range selected for projection, altering the arrangement of points on the projected lattice. In a real structure with atoms actually in the lattice, this shift in  $a_{\perp}$  forces a rearrangement of those atoms, a diffusive process that may not happen even on laboratory timescales for many materials. The shift in  $a_{\perp}$  is called a *phason shift*.[24]

The diffraction pattern of a quasicrystal does not change if there is a phonon or phason shift. Finite wavelength phonon and phason excitations can reduce or

broaden a diffraction peak. Frozen-in phonon strains are not significant, since they relax rapidly. Frozen-in phason strains shift peak positions with greater shifts for greater  $a_{\perp}$ .

### 3.3 Symmetry and Quasiperiodicity

In considering the actions of symmetry group operations on quasiperiodic lattices, there is now a fundamental choice that has to be made: whether the definitions of symmetry based on group actions should apply to real or reciprocal space. In the crystallographic case, the answer was the same either way. In the quasiperiodic case, on the other hand, the window function has a dramatic effect. Group operations for a quasicrystal correspond to operations in the higher dimensional periodic lattice. Applying group operations such as rotation on the higher dimensional lattice can cause some points in that lattice that were originally inside a finite window to be transformed out of it. The result upon projection is a quasicrystal with the same symmetry, but not the same atomic positions. With the introduction of the window function, the phason symmetry could be said to be spontaneously broken.

The Fourier transform of the window function (unless specifically chosen to be otherwise) is a continuous function, non-zero for nearly all  $\vec{Q}$ . The window function itself has the same symmetry as the lattice, so its Fourier transform has the same symmetry as the quasilattice. Hence the convolution is invariant under group operations—that is, the reciprocal space has non-zero support at all the quasilattice points and is invariant under point symmetry group operations. On the other hand, the real space has support only on a subset of quasilattice points which will not in general be invariant under point symmetry operations. To distinguish the situation in real space from the periodic case, one sometimes refers to the quasicrystal as having *orientational symmetry* instead of rotational symmetry. In orientational symmetry, not every real space point has the same nearest neighbors; instead, there

is a long-range orientational correlation between nearest neighbors.

For a three-dimensional translationally ordered structure with real atoms, one, two or three dimensions can be quasiperiodic. For such a structure with only one quasiperiodic dimension, there will be no change from the possible symmetries of a periodic case, since these structures are essentially stackings of two-dimensional periodic lattices. This is the special case of an incommensurate crystal, defined below.

It is now clear that we can have a quasilattice with arbitrary symmetry. Begin with a star of  $d + n$  integer linear independent unit vectors, symmetric under a chosen symmetry and construct a lattice in  $d$  dimensions. Then, to construct selection window, lift to  $d + n$  dimensions and choose a window so that its cross section is the projection of the unit hypercube in  $d + n$  dimensions. From this we can consider quasicrystals with quasiperiodicity in one, two or three dimensions.

A translationally ordered structure quasiperiodic in one dimension and periodic in the other two is called an *incommensurate crystal*. For a quasicrystal with two quasiperiodic dimensions and periodic in the third, there are no restrictions on the rotational symmetry about an axis parallel to the third dimension. Octagonal, decagonal and dodecagonal phases are among those symmetries that have already been observed.[33]

In three dimensions, however, the only possible point symmetries are those for which a corresponding regular polyhedron (a Platonic solid) can be constructed. There are five such polyhedra: cube, tetrahedron, octahedron, dodecahedron and icosahedron. The first three are compatible with periodicity and are observed in nature. The last two, dual to each other and hence with the same point symmetry, both contain five-fold rotation axes and are therefore crystallographically forbidden. However, these five-fold rotation axes do occur in quasicrystals. Five-fold symmetry is shown in the lattice of an AlCuFe quasicrystal in figure 3.2. Because the icosahedral symmetry is so central to this thesis, the next section is devoted to its structure and calculation of its diffraction pattern.

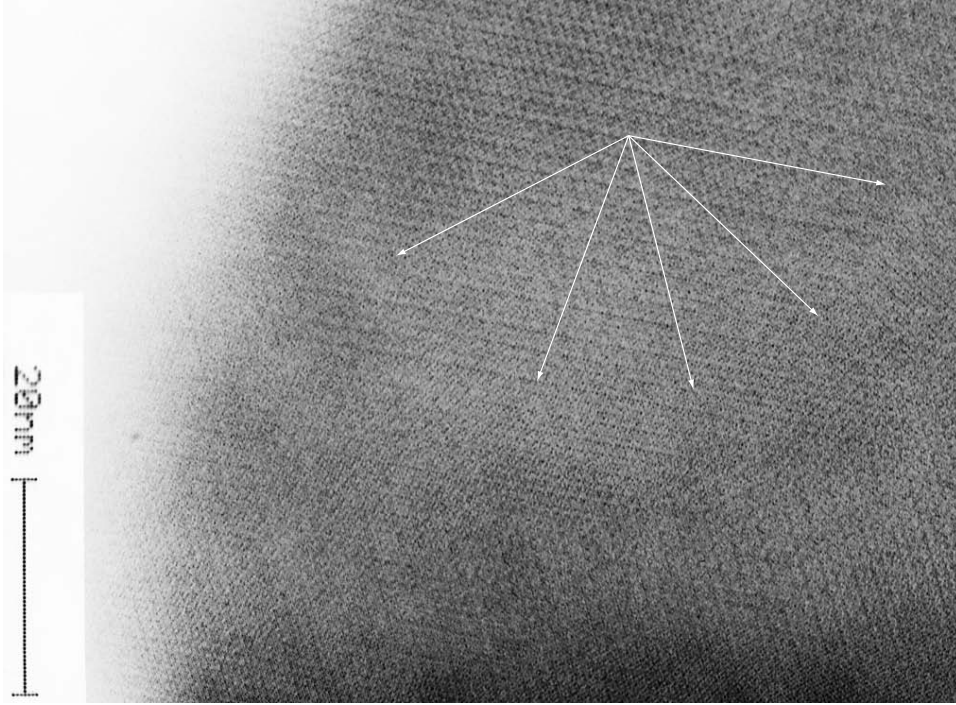


Figure 3.2: Transmission electron microscope image of the quasilattice of an AlCuFe quasicrystal, with the five planes of symmetry labeled with arrows.

### 3.4 The Icosahedral Quasicrystal

The icosahedral quasicrystal lattice can be constructed by projecting a six-dimensional hypercubic lattice, the six-dimensional analog of a three-dimensional cubic lattice. As a simple example, not meant to be realistic, consider the case of one type of atom at each lattice point, known as the *simple icosahedral* (SI) structure. The reciprocal lattice will be another six-dimensional hypercubic lattice. The position of any reciprocal lattice point in six dimensions can be described by the following relation:

$$\vec{Q} = \sum_{i=1}^6 n_i \vec{q}_i \quad (3.15)$$

where  $n_i$  are the coefficients for each  $\vec{q}_i$ , the six-dimensional basis vectors. Since this is a hypercubic lattice, the magnitude of all six basis vectors is the same.

When projecting the six basis vectors of the hypercubic lattice down to three

dimensions, there are several sets of vectors that can serve as the basis. The usual choice, however, are the six vectors that point along the six five-fold axes of the icosahedron. These vectors occur in three pairs so that the plane spanned by each pair is orthogonal to the planes spanned by the other pairs. This yields a set of coordinates that has all the advantages of orthogonal axes; moreover, since all six vectors have equal length, there is a symmetry between these three orthogonal axes. In selecting the order of the specific vectors of the icosahedron, the convention in [27] is used:

$$\begin{aligned}\vec{q}_1 &= (1, \tau, 0) \\ \vec{q}_2 &= (\tau, 0, 1) \\ \vec{q}_3 &= (0, 1, \tau) \\ \vec{q}_4 &= (-1, \tau, 0) \\ \vec{q}_5 &= (\tau, 0, -1) \\ \vec{q}_6 &= (0, -1, \tau)\end{aligned}$$

Any arbitrary vector can be expressed as a linear combination of these six basis vectors:

$$\vec{Q} = \sum_{i=1}^6 n_i \vec{q}_i \quad (3.16)$$

where  $\vec{q}_i$  in this equation is the basis vector  $\vec{q}_i$  in equation (3.15) projected into three dimensions, and the  $n_i$  are the same in both equations. Expressing these in a more convenient form in three-dimensional space using another set of indices:

$$\begin{aligned}h &= n_1 - n_4 \\ h' &= n_2 + n_5 \\ k &= n_3 - n_6 \\ k' &= n_1 + n_4 \\ l &= n_2 - n_5 \\ l' &= n_3 + n_6\end{aligned}$$

This yields two entirely equivalent definitions of  $\vec{Q}_{\parallel}$ , the length of the six-dimensional scattering vector  $\vec{Q}$  projected into three dimensions:

$$\vec{Q}_{\parallel} = \begin{bmatrix} h + \tau h' \\ k + \tau k' \\ l + \tau l' \end{bmatrix}$$

$$\vec{Q}_{\parallel} = \begin{bmatrix} 1 & \tau & 0 & -1 & \tau & 0 \\ \tau & 0 & 1 & \tau & 0 & -1 \\ 0 & 1 & \tau & 0 & -1 & \tau \end{bmatrix} \begin{bmatrix} n_1 \\ n_2 \\ n_3 \\ n_4 \\ n_5 \\ n_6 \end{bmatrix}$$

Similarly,  $\vec{Q}_{\perp}$  has two equivalent formulae:

$$\vec{Q}_{\perp} = \begin{bmatrix} h - \tau h' \\ k - \tau k' \\ l - \tau l' \end{bmatrix}$$

$$\vec{Q}_{\perp} = \begin{bmatrix} -\tau & 1 & 0 & \tau & 1 & 0 \\ 1 & 0 & -\tau & 1 & 0 & \tau \\ 0 & -\tau & 1 & 0 & \tau & 1 \end{bmatrix} \begin{bmatrix} n_1 \\ n_2 \\ n_3 \\ n_4 \\ n_5 \\ n_6 \end{bmatrix}$$

This convention is identical to that in Bancel [25] but for a trivial permutation of the ordering of the six vectors, so his  $n_i$  are the same but in a different order.

Janot also defines a one-dimensional indexing based on  $|\vec{Q}_{\parallel}|$ :

$$|\vec{Q}_{\parallel}|^2 \propto N + \tau M \quad (3.17)$$

where

$$N = 2 \sum_{i=1}^6 n_i^2 \quad (3.18)$$

$$M = h'^2 + k'^2 + l'^2 + 2(hh' + kk' + ll') \quad (3.19)$$

Because the primitive hypercubic lattice in six dimensions Fourier transforms into another six-dimensional hypercubic lattice, the indexing and basis vectors apply equally well to both real and reciprocal lattices.

### 3.4.1 Decorations of the Icosahedral Quasicrystal

In six-dimensions, the simple icosahedral (SI) structure is a primitive hypercubic lattice. Analogous to the face-centered cubic (FCC) and body-centered cubic (BCC) lattices in three dimensions, there can be face-centered and body-centered hypercubic lattices in six dimensions, which when projected down to three dimensions also yield quasicrystals with the icosahedral point symmetry. These are known as face-centered icosahedral (FCI) and body-centered icosahedral (BCI) quasicrystal lattices.

A primitive lattice with a basis can be described as a convolution of the lattice and the basis, so that the Fourier transform is simply the product of the Fourier transform of the lattice and the Fourier transform of the basis. In three-dimensional crystals, relative to that of the simple cubic structure, diffraction patterns of the face-centered and body-centered cubic structures will have peaks at the same values of  $|\vec{q}|$ , but those intensities will be modulated as a result of the structure factor (see section 1.x). Some of those peaks will have zero intensity (an “extinction”), canceled out by destructive interference as the result of the positions of atoms. Which peaks present in the simple cubic structure become extinct in the face-centered or body-centered structure is determined by the expression for the structure factor, leading to “extinction rules” that indicate which combinations of basis vectors will give to Bragg peaks in the diffraction spectrum.

Similarly, the quasicrystalline case has similar restrictions on allowed combinations of basis vectors, which can be expressed in the  $n_i$  or  $h, h', k, k', l, l'$  notation. The simple icosahedral case, like the simple cubic, will have no extinctions and all combinations of the  $n_i$  are allowed; by definition,  $h + k'$ ,  $k + l'$  and  $l + h'$  must be

even. In the face-centered case:

$$\sum_{i=1}^6 n_i = 2n \text{ (an even number)} \quad (3.20)$$

This creates the following additional restriction: both  $k + k + l$  and  $h' + k' + l'$  must be even. In the body-centered icosahedral case, all of the  $n_i$  must be even or odd, and the following three quantities must be multiples of four:  $h + l + h' + k'$ ,  $h + k + l' + k'$  and  $l + k + h' + l'$ .[27]

## 3.5 Powder Diffraction of an ideal Simple Icosahedral Quasicrystal

To construct a powder pattern for the simple icosahedral case, for each linear combination with each of the  $n_i$  varying through some range, a 6-dimensional vector in calculated using equation (3.16). Its  $|Q_{\parallel}|$  and  $|Q_{\perp}|$  are then calculated from matrix equations on page 51. Peak intensity  $I$ , related to the inverse of  $|\vec{Q}_{\perp}|$ , is estimated with the following formula employing the sinc function, the Fourier transform of a top hat window function:

$$I = 100 * \left( \frac{\sin(\frac{|\vec{Q}_{\perp}|}{2})}{\frac{|\vec{Q}_{\perp}|}{2}} \right)^2 \equiv \text{sinc}^2 \left( \frac{|\vec{Q}_{\perp}|}{2} \right) \quad (3.21)$$

Since  $|\text{sinc}^2| \leq 1$ , the factor of 100 automatically normalizes the intensities between 0 and 100, for convenience. This relation is only an idealized estimation of intensity, ignoring such factors as atomic form factors and other complications. The ideal pattern is plotted in figure 3.3, with  $-4 \leq n_i \leq +4$  and  $|Q_{\perp}| \leq 12$ .

### 3.5.1 Deviations from the ideal powder pattern

The ideal pattern in figure 3.3 is composed of a set of delta functions at points precisely determined by the structure of the lattice. In general, no such perfect pattern exists, as several effects can degrade the diffraction pattern of an otherwise good quasicrystal.

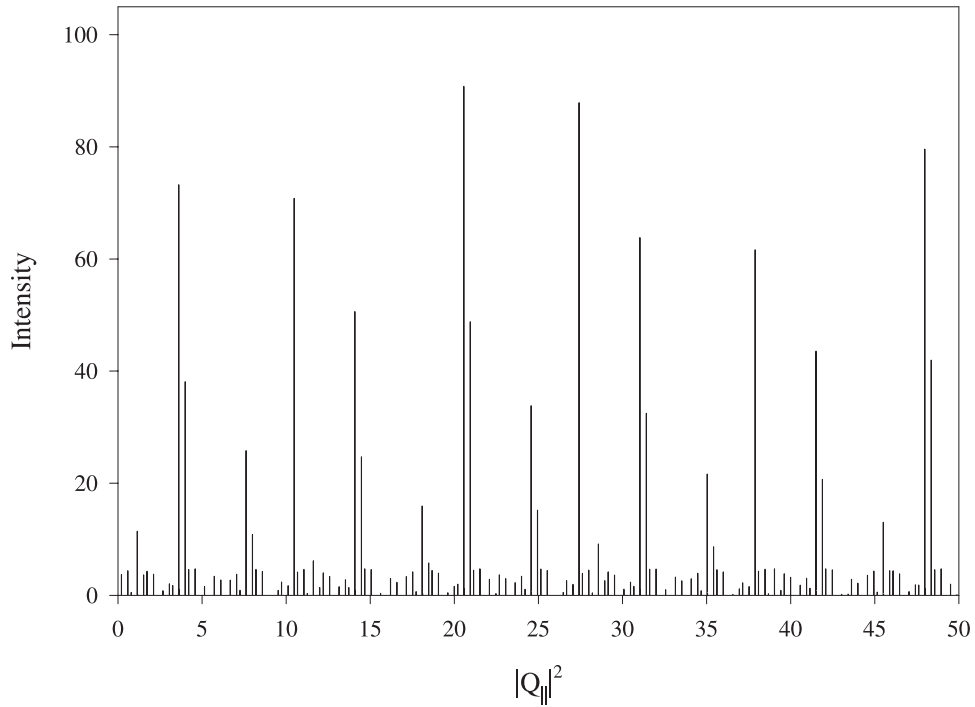


Figure 3.3: Powder pattern of ideal simple icosahedral quasicrystal for  $-4 \leq n_i \leq +4$  and  $|Q_{\perp}| \leq 12$ .

Point defects, multiple phases and other effects that commonly degrade the powder patterns of crystals will have similar effects in the quasicrystal case. However, unlike crystals, because the quasicrystals are projections from higher-dimensional lattices, their strains can reflect this higher-dimensional geometry. These are related to the phonon and phason strains present at the time of formation, as noted in section 3.2.2

Phonon strain, slight displacements along  $Q_{\parallel}$ , will cause displacements of atoms from the positions in a perfect lattice at the time of formation, somewhat lowering the symmetry. But phonon strains relax rather quickly (on the order of the speed of sound), and can usually be relaxed by further annealing. Furthermore, the atoms will vibrate at any finite temperature, creating a small amount of typical thermal broadening in a powder pattern that is invariably present in real materials. Both the phonon strain and thermal broadening occur in regular crystals, as well as quasicrystals.

A type of strain with no counterpart in the real crystals, however, is phason strain. Phasons are diffusive, so strains and quenched phasons are expected. Phason strain shifts peaks, while quenched phasons broaden. Thermal phasons reduce peak heights, but maintain the delta function form. Because phason magnitude is proportional to  $|\vec{Q}_\perp|$ , weaker peaks in the powder pattern are more likely to be broadened, reduced or shifted as a result of phasons.

# **Part II**

# **Original Work**



# Chapter 4

---

## The Program

A major focus of this thesis is to determine if and how powder diffraction patterns may be used to identify quasicrystallinity. The powder diffraction data for over 70,000 compounds are now available in the digital form of the Powder Diffraction File. To search these data, a computerized search scheme was devised to pull from the Powder Diffraction File a list of all minerals and other compounds that contain quasicrystalline features in their powder patterns but are not known to be quasicrystalline. Compounds from this list of “top candidates” for quasicrystallinity were then examined with electron microscopy in the laboratory to investigate their structure. This chapter describes the theory behind the computer searches and the searches themselves, while the next two detail the laboratory phase of the investigation. All of the computer code was written in the C++ programming language.

### 4.1 The Powder Diffraction File

The Powder Diffraction File (PDF) began as a series of published index cards with well vetted, high-quality powder diffraction patterns of several thousand materials. Sources for the data include the published literature, with some subsequent study of materials with single crystal diffractometry. The original criteria for inclusion of a pattern were stringent, and a committee would select the best data from among the reported data sets. The Powder Diffraction File was first printed on 3” x 5 ”

cards and in books; however, as it moved to digital format, the quantity of patterns rose dramatically while the individual quality deteriorated. The abundance of typographical errors (wrong formulae, references and other rather important pieces of information) in more recent data is inexcusable.

Every compound in the Powder Diffraction File is assigned a unique six-digit number and has a list of powder X-ray diffraction peaks. Each peak in the list has a *d*-spacing and an intensity at that *d*-spacing. In addition, each compound's entry usually contains the compound's formula and a reference and, when determined, crystallographic data (symmetry, lattice parameters, Miller indices of peaks, etc.). Because of the obvious importance of  $|Q_{\parallel}|^2$  to the quasicrystal case, particularly equation (3.17) ( $|\vec{Q}_{\parallel}|^2 \propto N + \tau M$ ), the *d*-spacing information was converted to  $|Q_{\parallel}|^2$ :

$$|\vec{Q}_{\parallel}|^2 = \frac{1}{d^2} \quad (4.1)$$

The final data set was composed of entries for a single compound, each entry with: PDF number, compound name, compound formula, total number of peaks in the powder pattern, and the list of peak data, containing for each peak  $|\vec{Q}_{\parallel}|^2$  and intensity. The program required a powder pattern to have at least twelve powder peaks in order to be included in the search; for patterns with fewer peaks, there was simply too little data to make an informed judgment on a compound's structure.

## 4.2 Search Strategies

A substantial effort was made to determine the most promising search strategies for identifying quasicrystals from powder diffraction data. The search in this theses has been confined to looking for the quasicrystal with the most distinctive diffraction pattern, the simple icosahedral structure. If this structure cannot be distinguished by its powder pattern, it would be futile to look for other quasicrystalline structures using powder data, particularly those involving a mixture of quasiperiodic and periodic peaks.

A major source of aid in the search program was the small list of published X-ray powder diffraction patterns of known quasicrystals that indexed each peak to a six-dimensional icosahedral basis vector. In several cases these index assignments were verified in the papers with two-dimensional electron diffraction. Our search program was therefore designed to index powder patterns to the six basis vectors of the icosahedron. For every peak with a scattering vector of  $|\vec{Q}|$  in a given published quasicrystal powder pattern, the calculated ideal icosahedral pattern described in section 3.5 was scaled so that the  $|\vec{Q}_{\parallel}|$  of the calculated (100000) peak coincided with  $|\vec{Q}|$ . For each scaling of the calculated pattern, every real peak was indexed to the closest peak in  $|\vec{Q}_{\parallel}|$  in the calculated pattern. Based on several criteria, the program then determined which scaling was the best fit to the real data; the program's peak assignments based on the best scaling could then be checked against the published data. The search procedure based on the criteria that automatically reproduced the published indexings was then applied to the full Powder Diffraction File, and those patterns with statistics similar to the real quasicrystals were then deemed to be “top candidates” for subsequent experimental investigation.

Several challenges must be met in designing a search procedure. Some of the patterns in the PDF were found to have errors, either because the original references had errors or because they were transcribed incorrectly. Some materials, clearly marked as a mixture of phases when published, were not so clearly marked in the Powder Diffraction File. Quenched defects like phason strain would cause some quasicrystal peaks to be shifted from their ideal positions. Finally, there is a wide variety in the number of peaks extracted in a pattern. A robust search procedure must take all of these factors into account, and more.

One thing is certain: because of the inherent difficulties mentioned above, there is no *single* screening criterion that can decide whether a given powder pattern corresponds to a quasicrystal or not. Instead, a battery of screening criteria are required, each with parameters that have to be adjusted. After extensive testing, it was found

that, while the choice of screening tests and parameters is not unique, different choices make little difference to the results, as long as there are enough different screening tests.

### 4.3 Screening Criteria

For every scaling of the ideal calculated pattern, each peak in the real data is assigned the closest calculated peak in terms of  $|\vec{Q}_{\parallel}|$ . Several features of the measured and closest-matching ideal peak proved to be effective screening criteria.

**% Deviation** The percent deviation between real and ideal peaks.

$$\Delta_{\%,j} = 100 * \left| \frac{|Q_{\parallel,j,\text{real}}| - |Q_{\parallel,j,\text{calc}}|}{|Q_{\parallel,j,\text{real}}|} \right| \quad (4.2)$$

A lower  $\Delta_{\%}$  obviously represents a closer match between real and calculated peaks.

**N** The length of the closest-matching 6-dimensional  $\vec{Q}$ . We use  $N$  following Janot's convention:

$$N_j \equiv 2 \sum_{i=1}^6 n_{i,j}^2 = 2|\vec{Q}|^2 \quad (4.3)$$

where  $j$  labels the peak. Any  $|Q_{\parallel}|$  can be approached to within any arbitrarily small distance by going to suitably high  $n_i$ . In reality, large  $n_i$  corresponds to scattering off planes in reciprocal space far from the origin. The likelihood of actually seeing such a Bragg peak approaches zero. A vector with low  $N$  is more likely to be observed.

**$Q_{\perp}$**  Magnitude of the  $Q_{\perp}$  vector  $|\vec{Q}_{\perp}|$ . As explained in section 3.5, a lower value of  $|Q_{\perp}|$  indicates greater intensity, and, therefore, likelihood of being observed. The powder patterns of real quasicrystals have a large fraction of low- $|\vec{Q}_{\perp}|$  peaks.

The three parameters above are calculated for each  $j$ th peak and each scaling. For a given scaling, these parameters were averaged over all  $K$  measured–ideal peak pairs in the pattern. Both an unweighted average  $\bar{P}_u$  and a weighted average  $\bar{P}_w$  were calculated for each parameter  $P$ :

$$\bar{P}_u = \frac{1}{K} \sum_{j=1}^K P_j \quad (4.4)$$

$$\bar{P}_w = \frac{\sum_{j=1}^K W_j P_j}{\sum_{j=1}^K W_j} \quad (4.5)$$

where  $W_j$  is the weighting factor in the weighted average  $\bar{P}_w$ . The two weighting factors used are the real intensity,  $I_j$ , and its square root,  $\sqrt{I_j}$ . Weighting by the real intensity  $I$  gives the brightest peaks up to two orders of magnitude more importance than the weakest, severely punishing bad matches of bright peaks but effectively discarding matching information among the weak ones. On the other hand, weighting with the square root or logarithm of the real intensity penalizes poor matches in bright peaks slightly less but still gives some importance to matches among weaker peaks. Both  $I$  and  $\sqrt{I}$  yielded correct indexings of published quasicrystals and thus were both used; weighting by  $\log I$ , on the other hand, gave spurious results and was discarded.

For the averages of the  $\Delta\%$  parameter only, the worst (largest)  $\Delta_{\%,j}$  was discarded to prevent a single displaced peak from compromising an otherwise good quasicrystal pattern.

Good quasicrystal patterns have low values of  $N$ ,  $\Delta\%$  and  $Q_\perp$ , and the best scaling factor leads to an indexing that has low values of these parameters. The program therefore minimized  $P$ , a combination of  $N$  and  $\Delta\%:$

$$P = N_w + W * \Delta_{\%,w} \quad (4.6)$$

where  $W$  is an adjustable weighting factor and  $N_w$  and  $\Delta_{\%,w}$  are weighted averages of  $N$  and  $\Delta\%$ , respectively. A weighting parameter of 100 was generally used, as it made the contributions to  $P$  from both  $N$  and  $\Delta\%$  approximately equal, but  $W$  could vary by a factor of 10 with little effect.

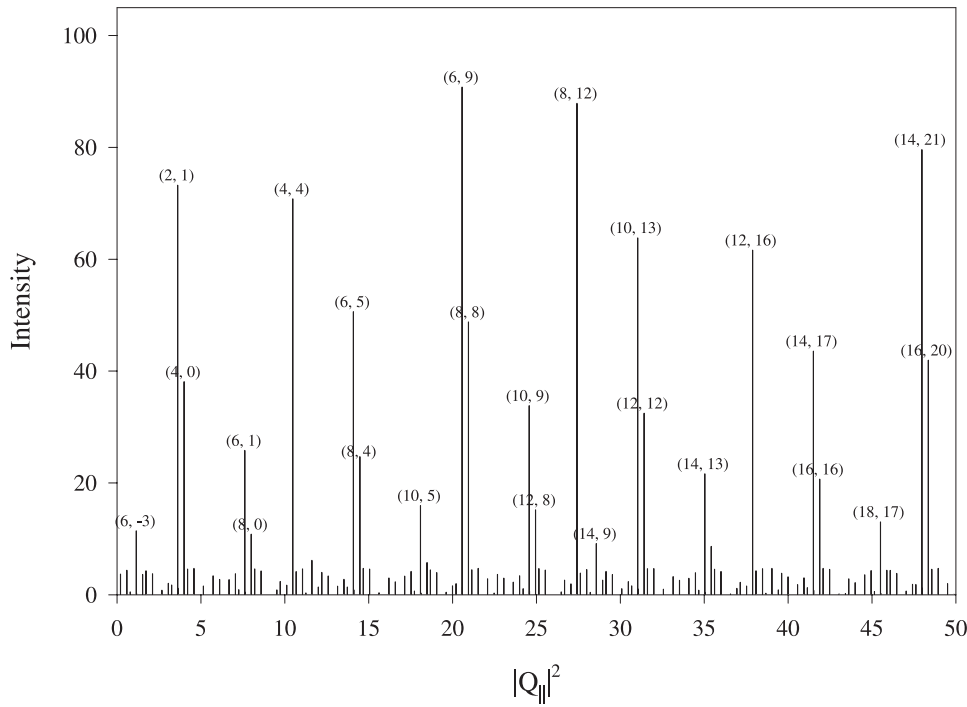


Figure 4.1: Powder pattern of ideal simple icosahedral lattice

After selecting the correct indexing, several more criteria were used:

**Number of Pairs** Number of  $(\Delta N, \Delta M) = (2, -1)$  pairs among the calculated peaks best matched to the real data. Checking this parameter is not *a priori* obvious, but a brief look at the calculated ideal icosahedral powder pattern in figure 4.1 (the same as figure 3.3, except that peaks with intensity greater than 10% have  $(N, M)$  indices indicated) should reveal that the brightest peaks occur in pairs of  $(\Delta N, \Delta M) = (2, -1)$ . A large percentage of the peaks in real quasicrystal patterns tend to occur in these  $(\Delta N, \Delta M) = (2, -1)$ , as well.

As is clear from figure 4.1, both peaks in a  $(2, -1)$  pair have similar intensity; this is also true in the real quasicrystals, where the measured intensities of the peaks in a  $(2, -1)$  pair did not differ by more than by a factor of eight. So in the matched data, the program required the real intensities of two peaks to

be within a factor of eight in order for the closest-matched calculated peaks to qualify as a  $(2, -1)$  pair.

**Pair %** Percentage of real peaks that are involved in a  $(\Delta N, \Delta M) = (2, -1)$  pair. This is simply defined as:

$$100 * \frac{\text{Number of Pairs}}{K} \quad (4.7)$$

**Double Count** Number of “double matches,” in which a single calculated peak was matched to more than one real peak, clearly not physical. Only patterns with at most one double match are allowed.

**Intensity** Intensity is never used directly as a matching criterion. Atomic decoration of the quasicrystal lattice will modulate intensities without affecting the underlying positions of the peaks in the reciprocal lattice. There is no way to account for these decoration effects ahead of time. Also, since the lengths of the vectors used are arbitrary, the intensity estimated by the  $\text{sinc}^2(|Q_\perp|/2)$  is prone to large variation, particularly near the zeroes of the sinc function; simply scaling  $Q_\perp$  slightly can result in large swings of the intensity for some peaks. The simplistic intensity formula ignores several other complications (weakening of the Bragg peak as a result of a longer  $Q_\parallel$  vector, degeneracy due to multiple points at the same  $|Q_\parallel|$  in reciprocal space, etc). Therefore, the program relies on the general notion that a lower  $Q_\perp$  will correlate with higher intensity, instead of any direct intensity formula.

There were several other tests that did not turn out to be very useful. Two examples are given:

**$\tau$  and other Ratios** Because of the importance of  $\tau \equiv (1 + \sqrt{5})/2$  in pentagonal geometry, it was thought that  $\tau$ -ratios would appear among the  $|Q_\parallel|$  of the quasicrystal peaks; for example, the peaks with  $(N, M) = (4, 0)$  and  $(4, 4)$  have  $|Q_\parallel|^2$  positions related by a factor of  $\tau^2$ . This did not turn out to be the case,

as thousands of patterns had peaks separated by  $\tau$  within as tight tolerances as the good quasicrystals.

**Match %** The percentage of calculated peaks which after scaling fell within the range of the real data that were matched to real peaks was called the match percentage. While one or two very good quasicrystals had high values of the match %, most were completely indistinguishable from regular crystals based on this parameter.

### 4.3.1 Hoaxes

Unfortunately, even the reasonably stringent set of screening criteria above could still be fooled by certain types of behavior within patterns, evident even before doing any investigation in the laboratory. One problem involves what are believed to be coincidental ratios in, for example, hexagonal crystals that mimic the icosahedral symmetry in a powder pattern. One of the samples with the best statistics, theophrastite  $\text{Ni(OH)}_2$ , may have hoaxed the program in this way. Table 4.1 presents the peak data from theophrastite's powder pattern, giving indexings and predicted values of  $|Q_{\parallel}|$  from both crystalline and quasicrystalline basis vectors.

There is essentially perfect agreement between all three values of  $|Q_{\parallel}|$ . Moreover, comparing the two indexings, it is immediately apparent that the two are scalings of each other; the six-dimensional peaks (100000), (200000) and (300000) correspond to the hexagonal peaks (001), (002), and (003). The degree of agreement is simply remarkable. But if the icosahedral pattern is just a simple scaling of a hexagonal pattern, it is unclear why the pattern passes all of the rest of the tests with good parameters. It may be simply that specific  $c/a$  ratios in hexagonal or other crystals can create a symmetry that mimics the icosahedral. In the specific case of theophrastite, its structure is currently being investigated.

6-D Indices	(N,M)	hkl	Real $ Q_{\parallel} $	Hex $ Q_{\parallel} $	QC $ Q_{\parallel} $
100000	(2,1)	001	2.172	2.172	2.172
110000	(4,4)	100	3.694	3.694	3.694
110100	(6,5)	101	4.284	4.285	4.285
200000	(8,4)	002	4.344	4.343	4.343
210001	(12,8)	102	5.701	5.702	5.702
210100	(12,12)	110	6.398	6.398	6.399
300000	(18,9)	003	6.515	6.515	6.515
211010	(14,13)	111	6.757	6.756	6.757
220000	(16,16)	200	7.386	7.388	7.389
310001	(22,13)	103	7.491	7.489	7.489
220100	(18,17)	201	7.698	7.700	7.701
310000	(20,16)	112	7.734	7.733	7.734
311010	(24,20)	202	8.569	8.570	8.571

Table 4.1: Theophrastite powder diffraction pattern from the Powder Diffraction File. The first two columns list the six-dimensional icosahedral indexing and Janot’s  $(N, M)$  indices (see section 3.4) as calculated by our program. The third column lists the hexagonal Miller indices from the Powder Diffraction File itself. The last three columns contain the value of  $|Q_{\parallel}|$  from the real data, the result from indexing with icosahedral vectors, and the result from indexing with the ordinary hexagonal vectors.

## 4.4 Comparison with the published data

There are 18 patterns marked as quasicrystals in the Powder Diffraction File, each listed as having more than a dozen peaks after removing duplicates and non-quasicrystal phases that were incorrectly marked. Ten compounds are simple icosahedral quasicrystals, of which seven have published indexing. Because 441195 and 461059 are based on the same original data, there are really only six unique patterns. Because of the high degree of symmetry present in the icosahedron, there are no unique vectors for a given  $|Q_{\parallel}|$ . Thus among the six patterns appear several different indexing schemes, usually the result of choosing different icosahedral basis vectors or scaling by a factor of  $\tau^3$ . As a result, the six-dimensional indices have been converted to  $N$  and  $M$  by Janot’s convention [27] (instead of a non-unique six-dimensional vector) for both the published data ( $N_{\text{pub}}, M_{\text{pub}}$ ) and our calculated output [ $N_{\text{calc}}, M_{\text{calc}}$ ].

The patterns for these six quasicrystals, with both the indexing from our program and the published indexing, are contained in Appendix A. The only pattern of the six best simple icosahedral patterns that did not index  $\geq 90\%$  correctly was the pattern 461056. Nevertheless, all except one of its brightest peaks with intensity greater than 20% match without error, so although a good many of the weaker peaks have shifted, perhaps due to phason strain or sample defect (the pattern itself is the worst of the six simple icosahedral quasicrystals by the other criteria), the program has nevertheless chosen the correct scaling factor. It is also common in the literature for weak peaks to have several possible assignments, indicating that the authors are not completely sure how to index them. Nevertheless, in all of these cases, the program has clearly scaled the icosahedral calculated pattern correctly; any other scaling factor would immediately cause *all* but maybe one peak to completely miss the correct assignment.

Based on these results, it is concluded that the method of minimizing  $P$  according to equation (4.6) leads to the correct scaling.

## 4.5 Key Search Results: Scatterplots

The final goal of the program is to identify which parameters can separate the known quasicrystals from the other tens of thousands of patterns. Scatterplots of various parameters were created to determine which parameters were useful and what numerical values of these parameters should be selected. After parameters that filter quasicrystals were determined, the program was set to recognize only those patterns with values within the correct range, creating a much shorter list of compounds that included both the known quasicrystals and a few surrounding patterns. These surrounding patterns then composed the list of top candidates of potential quasicrystals.

Every plot has the same symbol scheme. The red polygons are the known simple-icosahedral quasicrystals that the program indexes in agreement with, if extant, a published indexing. Each quasicrystal has a unique polygon, according to table 4.2,

which also lists numerical values for weighted average  $N$ , % Deviation and  $Q_{\perp}$ , as well as the pair percentage (see section 4.3 for definitions of these parameters).

PDF No.	Formula	Symbol	$N$	% Dev.	$Q_{\perp}$	Pair %
401158	$\text{Al}_6\text{CuLi}_3$	●	10.23	0.174	5.10	52.6
401285	$\text{Al}_{56.1}\text{Cu}_{10.2}\text{Li}_{33.7}$	●	8.22	0.0087	4.67	80.0
410928	$\text{Al}_6\text{CuLi}_3$	▼	7.90	0.082	4.42	47.1
441195	$\text{Al}_6\text{Mn}$	▼	4.79	0.059	3.15	47.6
441209	$\text{Al}_6\text{CuLi}_3$	■	10.00	0.198	5.01	50.0
451317	$\text{Al}_{70}\text{Pd}_{20}\text{Re}_{10}$	■	9.24	0.208	4.10	28.6
451318	$\text{Al}_{70}\text{Mn}_{10}\text{Pd}_{20}$	◆	6.43	0.148	3.86	57.1
461056	$\text{Al}_6\text{CuMg}_4$	◆	12.74	0.273	4.96	24.0
461059	$\text{Al}_{86}\text{Mn}_{14}$	▲	4.79	0.085	3.15	47.6

Table 4.2: Table of published simple icosahedral quasicrystals and the weighted average parameters  $N$ , % Deviation and  $Q_{\perp}$ .

- + The green square with a white cross is the original AlMn alloy found by Schechtman in which quasicrystallinity was first observed.
- ◆ The blue and yellow diamonds are other known, published quasicrystals that occur in a structure other than simple icosahedral, for example face-centered icosahedral.

The black dots are the 7,000 minerals in the Powder Diffraction File, the unknown data; this subset of the 70,000 total patterns in the Powder Diffraction File was plotted for convenience (fewer points), as both the mineral subset and the whole file have the same distributions in parameter space.

Figures 4.2, 4.3 and 4.4 show how the scatterplots were used to determine which parameters best separated quasicrystals and to set numerical limits on those parameters.  $A$ ,  $B$ ,  $C$  and  $D$  are all hypothetical parameters for the purposes of illustration; parameters  $A$  and  $B$  are effective screens for quasicrystals, while  $C$  and  $D$  are not. The region of the plot occupied by the group of known quasicrystals (red polygons) was encircled with a dotted blue ellipse, whose center was marked with a yellow cross:

+. The region of the plot with the majority of minerals (black dots) was similarly encircled by a blue ellipse, whose center was also marked with a yellow cross.

A greater distance between the two yellow crosses (marking the centers of the two ellipses) along a given axis represented a greater separation of the quasicrystals based on the parameter represented by that axis. There were three possible scenarios. Both parameters effectively separate the quasicrystals out, as depicted in 4.2: the centers of the two ellipses are far apart in both dimensions, and the ellipses themselves are distinct. If instead only one parameter is effective, as in figure 4.3, the crosses are far apart in one dimension (here the  $x$ -axis plotting parameter  $B$ ), while close together in the other (the  $y$ -axis plotting parameter  $C$ ). Finally, when neither parameter effectively separates the quasicrystals, as in figure 4.4, the crosses are close together and the ellipses overlap significantly.

The numerical limits set for each parameter were also determined by projecting the blue ellipse onto the axis representing that parameter; the range intercepted along this axis by the projection determined the numerical limits. When the quasicrystals had lower values of a given parameter than the rest of the patterns, the selected numerical range was extended to the origin, and the limit on the parameter thus represented an upper limit. This is shown in figure 4.3, where the thick solid green lines represent the numerical limits on the parameters  $A$  and  $B$  selected by projecting the ellipse onto the axes and extending to the origin.

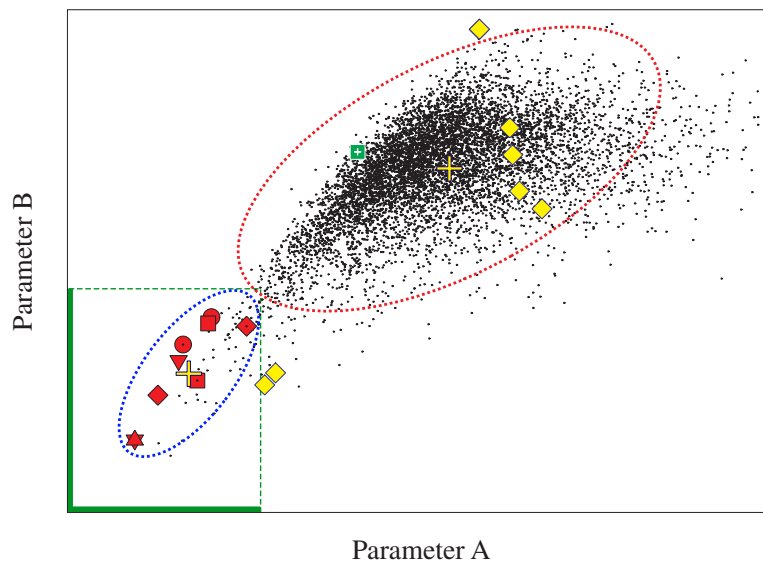


Figure 4.2: Scatterplot in which both parameters  $A$  and  $B$ , hypothetical parameters for the purpose of illustration, effectively separate the quasicrystals. Blue and red ellipses encompass the known quasicrystals and most of the minerals, respectively. Centers of the ellipses are marked with yellow crosses; the crosses are separated in both parameters, and the ellipses are distinct. The solid green lines near the origin represent the range intercepted by projecting the blue ellipse onto the two axes, then extending those projections to the origin.

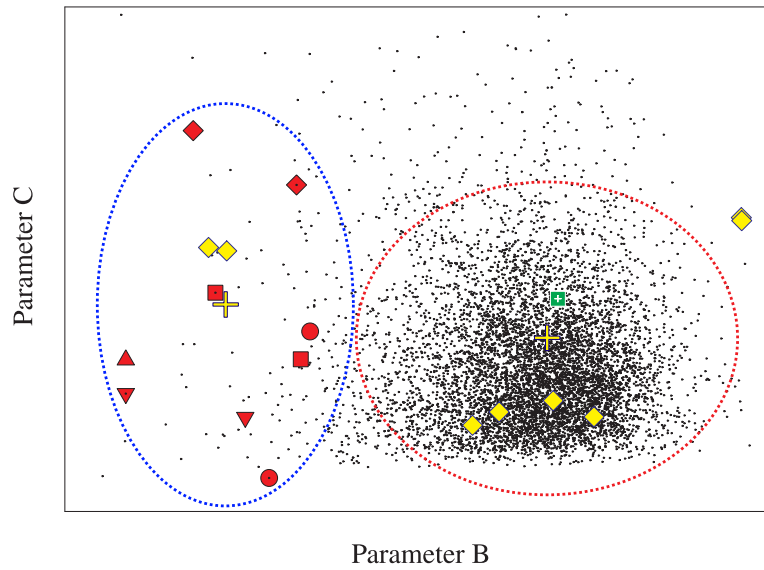


Figure 4.3: Scatterplot in which parameter  $B$  is effective at separation, but parameter  $C$  is not.  $B$  and  $C$  are hypothetical parameters for the purpose of illustration. The crosses are thus separated by a good distance along the  $x$ -axis, but are close together in  $y$ -axis position.

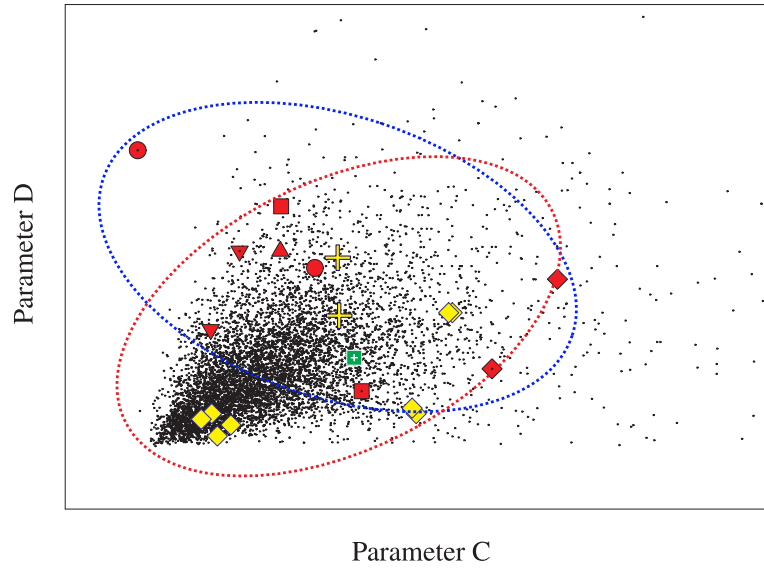


Figure 4.4: Both parameters  $C$  and  $D$  are ineffective at separation.  $C$  and  $D$  are hypothetical parameters for the purpose of illustration. The crosses are close together in both  $x$  and  $y$ , and the ellipses overlap significantly.

The set of parameters used to select the quasicrystals when weighted averages were weighted by intensity alone was:

$$N \leq 12 \quad (4.8)$$

$$\% \text{ Deviation} \leq 0.3 \quad (4.9)$$

$$|Q_{\perp}| \leq 5 \quad (4.10)$$

$$\text{Pair \%} \geq 10\% \quad (4.11)$$

Weighted averages were generally superior to simple unweighted averages in separating out quasicrystals; an example for % Deviation is given in figure 4.5. The number of  $(\Delta N, \Delta M) = (2, -1)$  pairs was highly dependent on the number of peaks in a powder X-ray diffraction pattern, as shown in figure 4.8 and hence not effective at separation. Normalizing for different data sizes among various patterns by dividing by the number of peaks, leading to a pair percentage which by contrast was an exceedingly good test at separating out the quasicrystals, as shown in 4.9. That match percentage is not a very effective parameter is demonstrated in figure 4.10. Weighting by the square root of the intensity  $\sqrt{I}$  led to very similar results as weighting by  $I$  alone, as the shapes of the distributions in both cases are nearly the same (see figure 4.11 for an example). Numerical parameters were determined from the scatterplots to be  $N \leq 18$ ,  $\% \text{ Deviation} \leq 0.4$ ,  $|Q_{\perp}| \leq 7$  and  $\text{Pair \%} \geq 10\%$ .

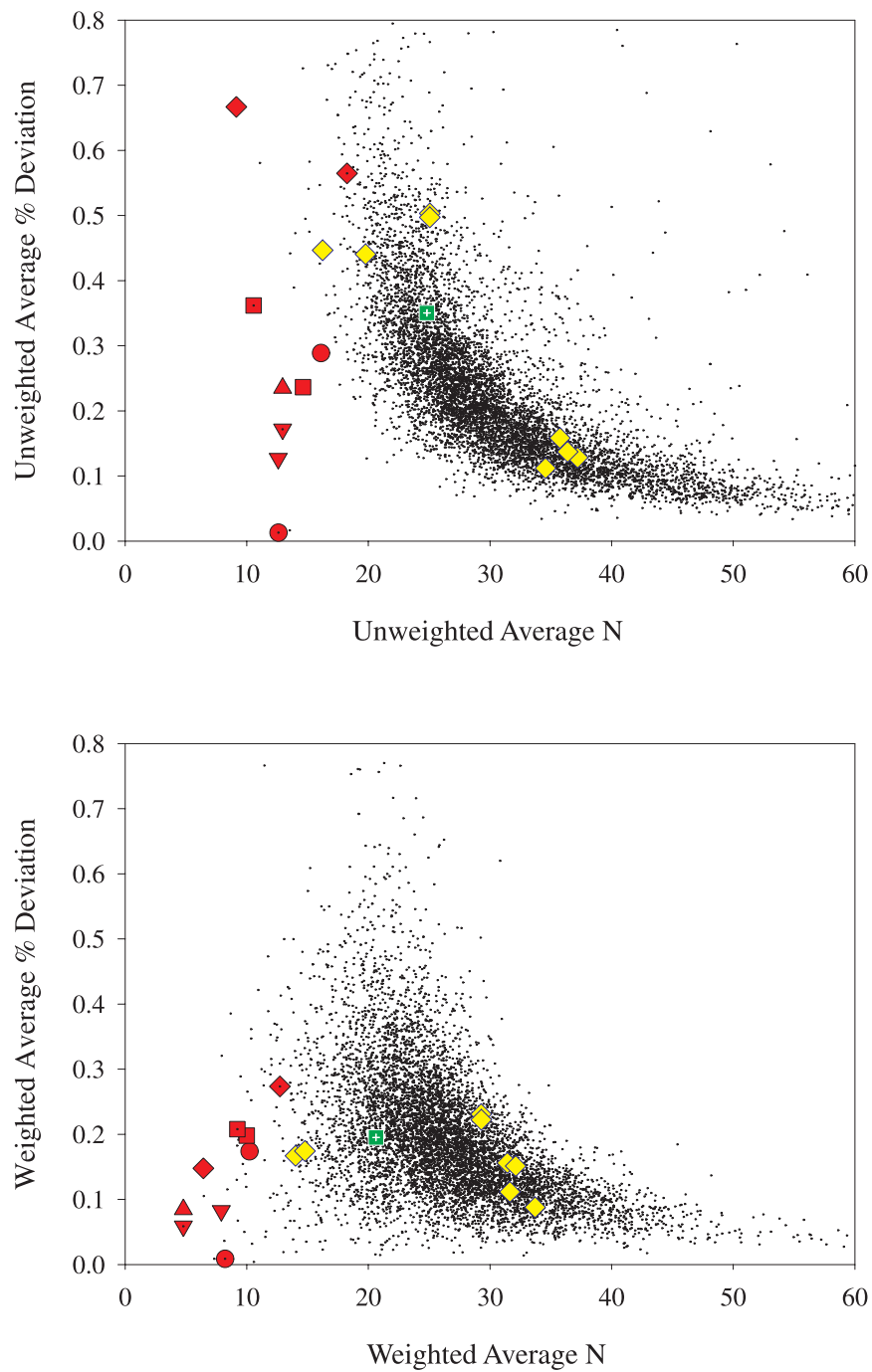


Figure 4.5: Scatterplots of  $N$  vs. % Deviation. Top plot based on unweighted averages, bottom plot based on averages weighted by intensity alone.  $N$  is the weighted average length of the the closest matching six-dimensional scattering vector  $|\vec{Q}|$ . The % Deviation is the average of percent deviations in  $|\vec{Q}_{||}|$  between real and closest matching ideal peaks.

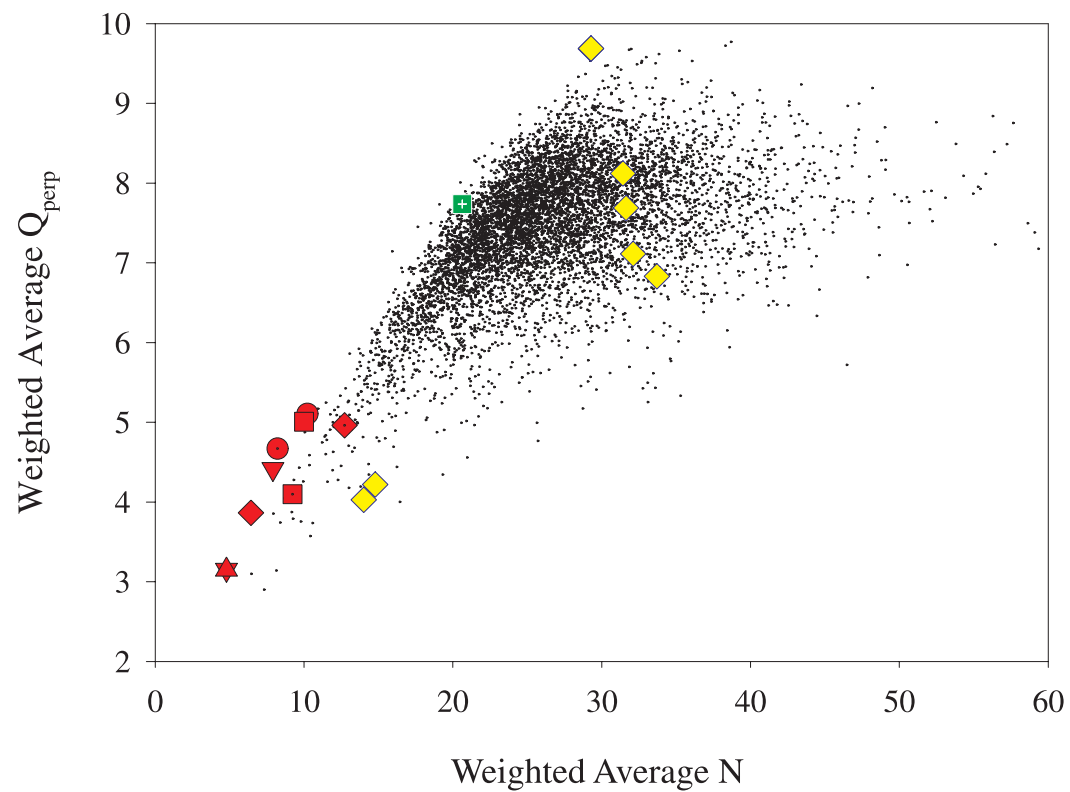


Figure 4.6: Scatterplots of  $N$  vs.  $|Q_{\perp}|$ , for averages weighted by intensity alone.  $|Q_{\perp}|$  is the magnitude of the  $\vec{Q}_{\perp}$  vector of the closest matching ideal peak.

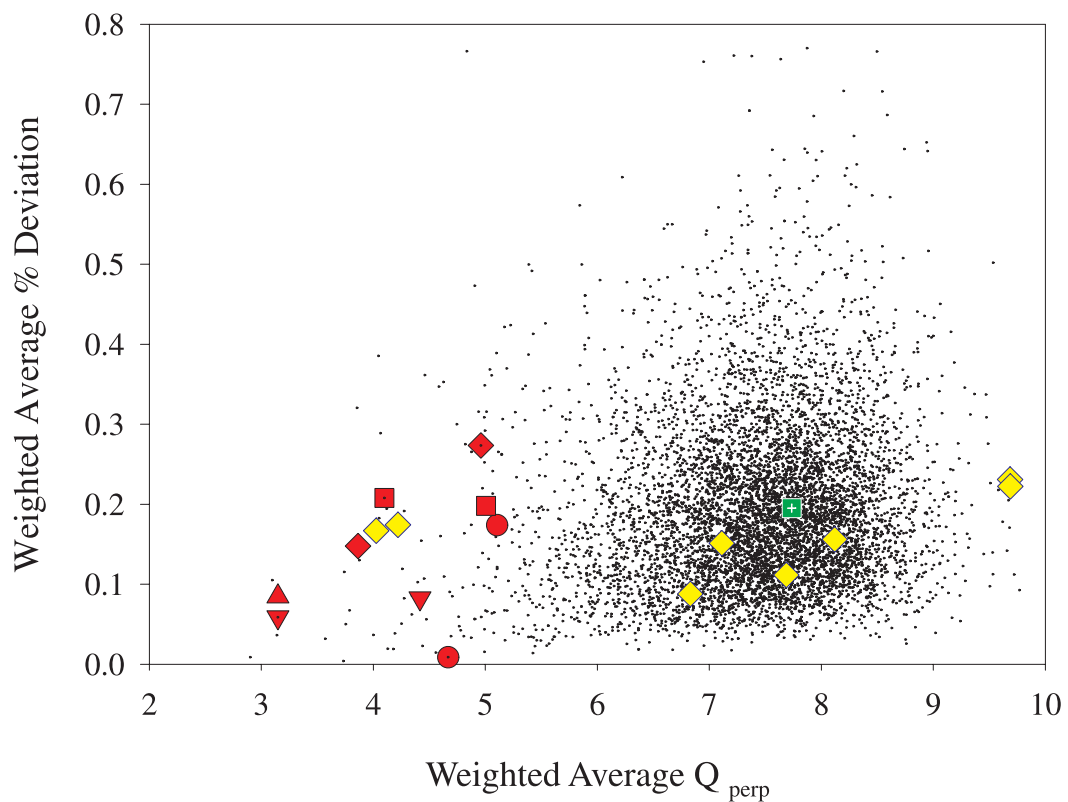


Figure 4.7: Scatterplot of  $|Q_{\perp}|$  vs. % Deviation, based on averages weighted by intensity alone.

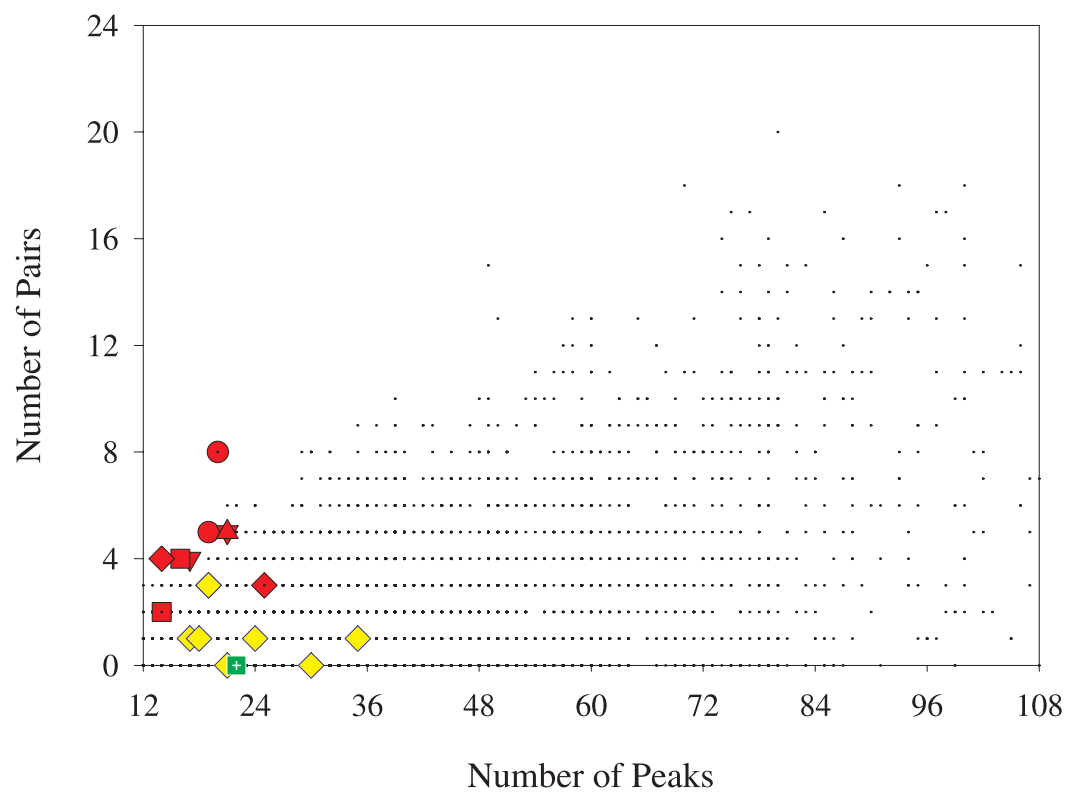


Figure 4.8: Number of peaks in the real data vs. the number of (2,1) pairs, per pattern. Only patterns with  $\geq 12$  peaks are checked by the programs.

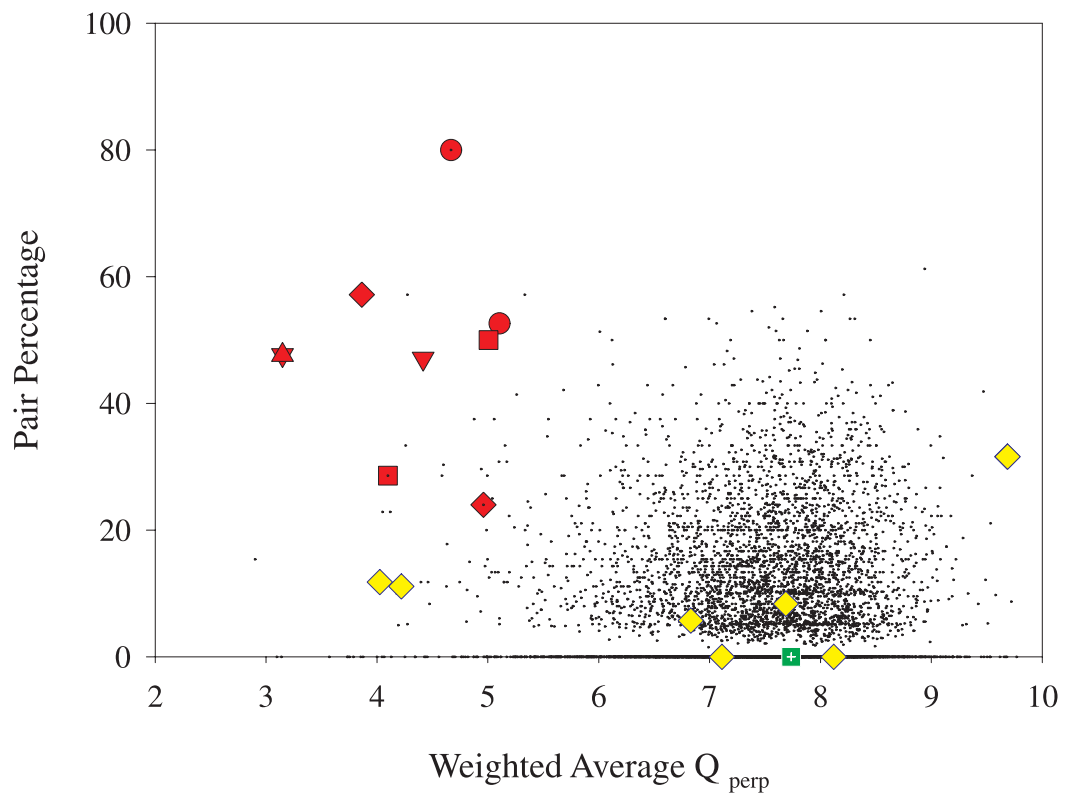


Figure 4.9: Average  $|Q_{\perp}|$  weighted by intensity alone vs. the percentage of peaks involved in a  $(\Delta N, \Delta M) = (2, -1)$  pair.

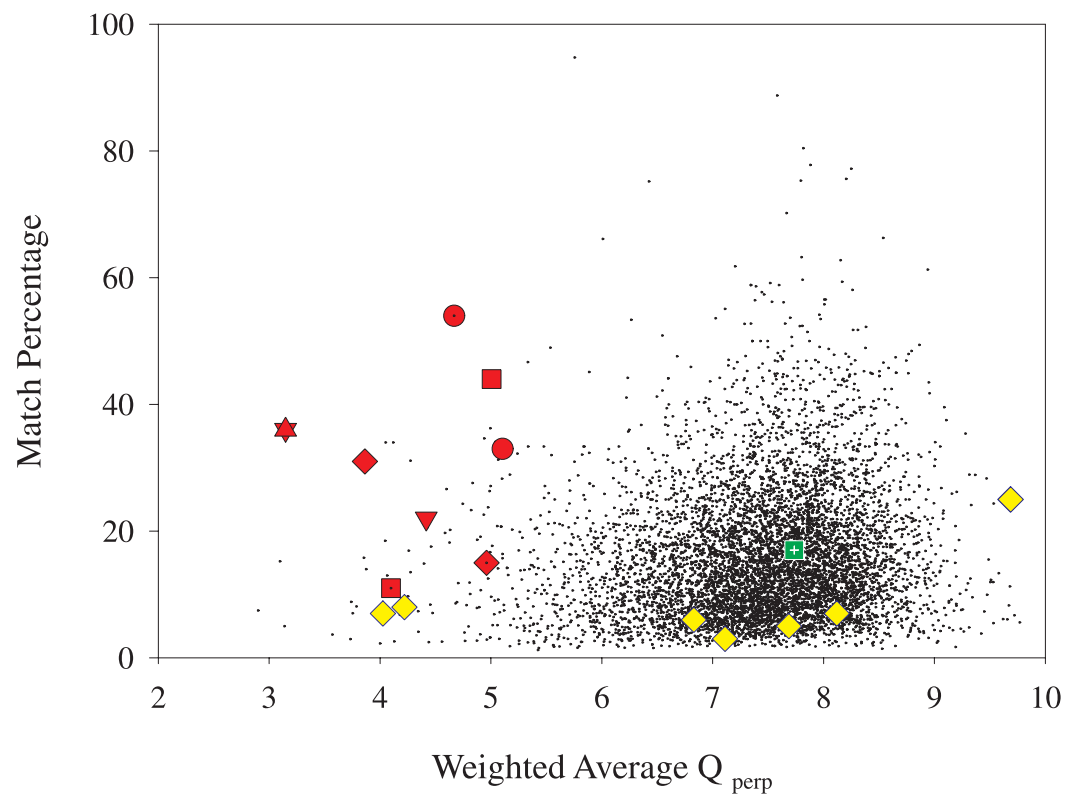


Figure 4.10: Average  $|Q_{\perp}|$  weighted by intensity alone vs. match percentage. The match percentage is the percentage of ideal calculated peaks which after scaling fell within the range of real data that were matched to real peaks.

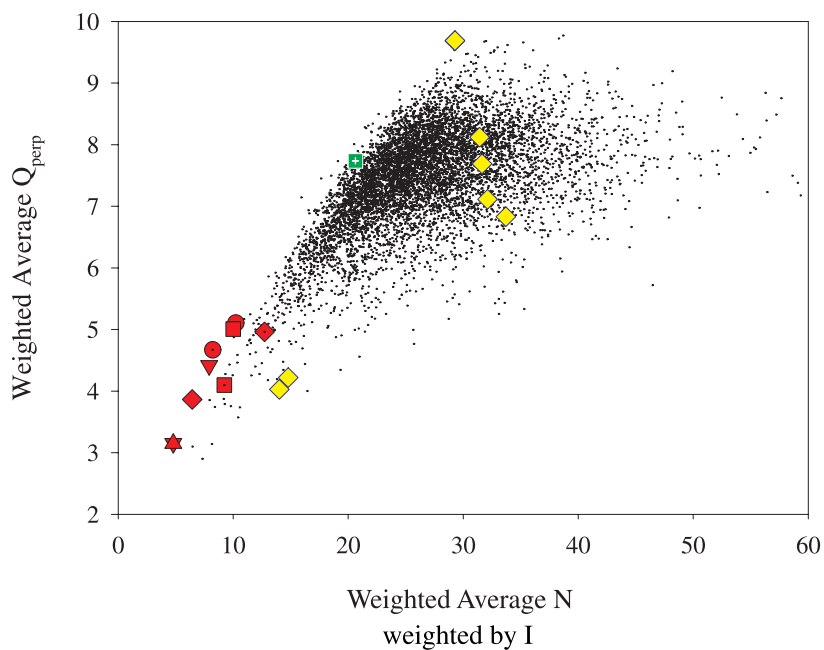
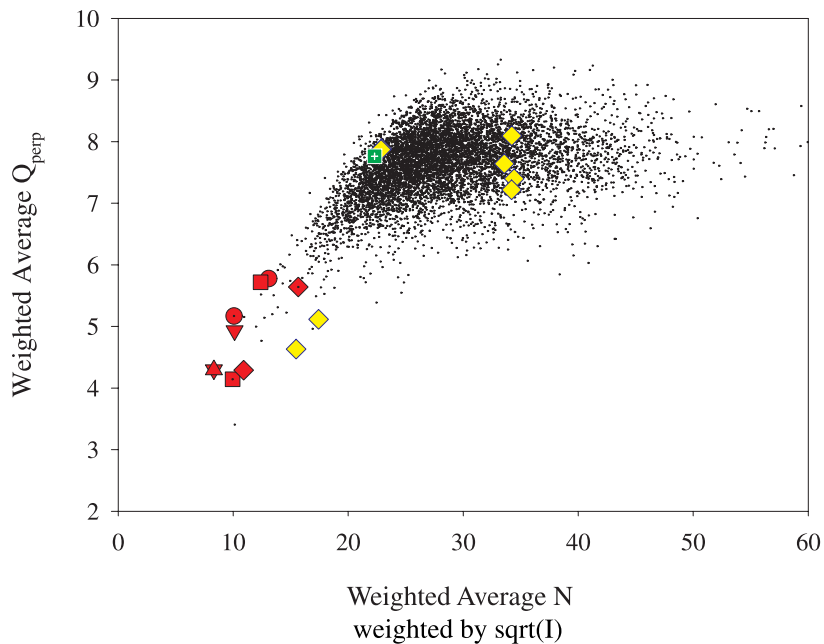


Figure 4.11: Scatterplots of  $N$  vs.  $|Q_{\perp}|$  based on averages weighted by  $\sqrt{I}$  (top) and  $I$  (bottom).

## 4.6 Key Search Results: The List

The ten best candidates among the minerals are listed in table 4.3. The PDF number, name and formula, the weighted averages of  $N$ , % Deviation, and  $|Q_{\perp}|$ , and the pair percentage are listed for all minerals. The rightmost column lists the weighting method, either  $I$  or  $\sqrt{I}$ , used to calculate the weighted average statistics. Of the 50 patterns or so generated by the programs using the numerical limits listed the previous section, those listed below are the most likely to be quasicrystalline. The full indexing data is given in Appendix B. The list of top fifty best candidates among all samples are given in Appendix C.

PDF No.	Formula	$N$	% Dev.	$Q_{\perp}$	Pair %	Weight
140117	Theophrastite, Ni(OH) <sub>2</sub>	7.331	0.008767	2.901	15.38	$I$
		10.14	0.01292	3.406	15.38	$\sqrt{I}$
020612	Krennerite, (Au,Ag)Te <sub>2</sub>	11.99	0.347	4.996	28.57	$\sqrt{I}$
181173	Volynskite, AgBiTe <sub>2</sub>	11.23	0.2999	4.747	11.76	$I$
461355	Miargyrite, AgSb(S,Se) <sub>2</sub>	9.898	0.1392	4.974	14.29	$I$
		12.42	0.2028	5.518	14.29	$\sqrt{I}$
250405	Haxonite, (Fe,Ni) <sub>23</sub> C <sub>6</sub>	13.88	0.3663	5.31	23.53	$\sqrt{I}$
011281	Covellite, CuS	10.06	0.2654	4.877	37.5	$I$
360387	Cabriite, Pd <sub>2</sub> SnCu	17.85	0.3972	6.612	21.05	$\sqrt{I}$
020318	Sulfohalite, 2Na <sub>2</sub> SO <sub>4</sub> ClF	14.3	0.3228	5.698	33.33	$\sqrt{I}$
021145	Allargentum, Ag-Sb	17.86	0.2849	6.505	28.57	$\sqrt{I}$
021293	Nicolite, NiAs	17.46	0.2706	6.513	25	$\sqrt{I}$

Table 4.3: Top ten mineral candidates for quasicrystallinity.  $N$  is the weighted average length of the scattering vector  $|\vec{Q}|$ . % Dev. is the weighted average of deviations between real and calculated values of  $|\vec{Q}_{\parallel}|$ .  $Q_{\perp}$  is the weighted average of  $|\vec{Q}_{\perp}|$ . Pair % is the percentage of real data peaks involved in a  $(2, -1)$  pair. Weight is the weighting factor used, either intensity  $I$  or its square root  $\sqrt{I}$ .



## Chapter 5

---

# Experimental Techniques: Electron Microscopy

Several samples from the list of natural quasicrystal candidates created by the computer (see chapter 4) were examined with electron microscopy to determine composition and structure. This investigation is ongoing, with only a few preliminary results to report thus far. Most of the minerals on the list are extremely rare and occur in a variety of forms. Some of the minerals are found only as small grains (micron scale) embedded in macroscopic pieces of host rock matrix (centimeter scale). For each of these minerals, a section of host rock about the size of a dime was placed in the scanning electron microscope. General imaging was accomplished by examining secondary electrons. The micron-sized grains of the desired phase were found and identified using a combination of backscattered electron detection and X-ray microanalysis. The diffraction pattern of electrons scattered from the surface was then imaged to investigate the underlying lattice structure. Other minerals could be isolated and pulverized into pure grains, which were examined in the transmission electron microscope. Traditional electron diffraction was performed on these samples.

To illustrate how we combined different techniques in the scanning electron microscope to locate and identify micron-sized mineral grains, example images of the mineral keithconnite are given. Keithconnite, a palladium telluride, was selected by an early version of the computer program, but did not ultimately make our final list

of top candidates. To illustrate electron diffraction, images of a real aluminum copper iron icosahedral quasicrystal are included.

Our brief treatment of electron microscopy will be limited to the devices and detectors actually used at the Princeton Materials Institute. While the author of this thesis performed all of the scanning electron microscopy, all work in the transmission electron microscope was performed by Dr. Nan Yao, Princeton Materials Institute.

## 5.1 Overview of Scanning Electron Microscopy

In a scanning electron microscope, an electron beam with a radius of a few nanometers strikes the surface of a sample. The beam electrons interact with the atoms in the sample to produce electrons and X-rays in several ways. Because of its small diameter, the electron beam acts as a local probe, and scanning over the surface creates a map of the various electron interactions. By selectively detecting and analyzing the electrons and X-rays that emerge, different types of maps can be constructed. The information in this discussion comes primarily from [45] and [43].

The basic geometry of a scanning electron microscope is shown in figure 5.1. Electrons released from the cathode (light blue) are accelerated toward the annular anodes (yellow) and pass through their center openings; subsequent electron optics, electromagnets that create magnetic fields (dark blue), direct and demagnify the beam (gray) until it is highly collimated (low divergence in the plane normal to the beam axis); by the time it hits the sample surface (rainbow of colors), the electron beam can be treated as a parallel column of electrons only a few nanometers in diameter. The beam can be precisely positioned over the surface by scan coils with fields perpendicular to the beam axis. Rapidly moving the beam over the surface and synchronizing it with the detector output display on a CRT like a traditional television screen creates a real-time “image,” a map of the detected interactions between beam electrons and the sample. The magnification is the ratio of the area of the TV

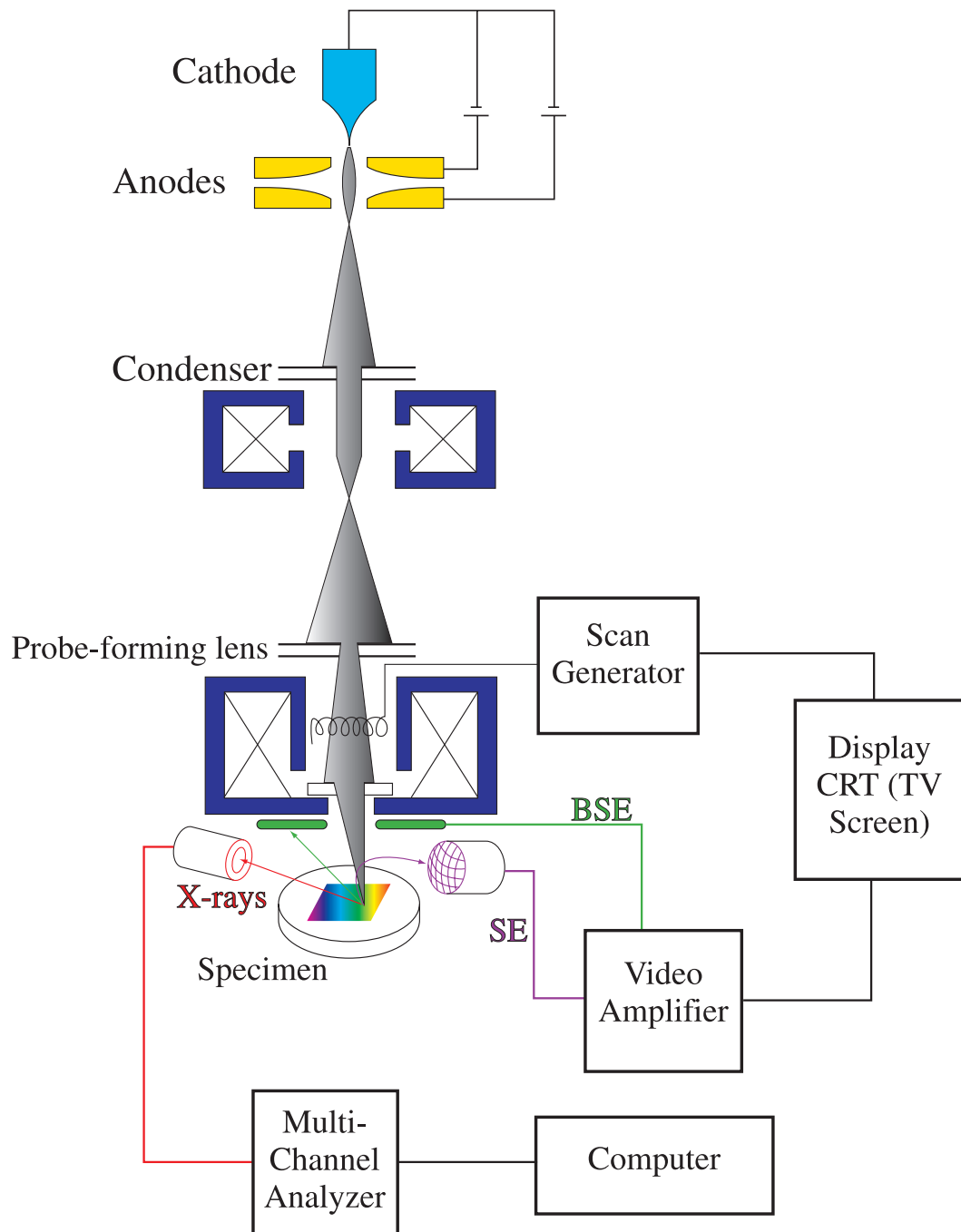


Figure 5.1: Diagram of the basic parts of a scanning electron microscope. Not to scale.

screen over the area scanned by the beam. Magnification can be increased simply by decreasing the area scanned by the beam; this is a tremendous advantage of scanning over traditional imaging techniques requiring complicated optics to change magnification. Resolution is limited by the electron beam radius. As in traditional optics, there are many important technical issues surrounding image distortion with electron optics, but their discussion is beyond the scope of this thesis.

There are several ways to generate the electron beam. The PMI machine employs *Schottky-emission*. An electric field is created between a tungsten cathode coated with ZrO and an annular anode by applying a voltage difference of a few kV. Coating the tungsten tip with ZrO reduces the effective work function  $\phi_{\text{eff}}$  from 4.5 eV to 2.7 eV. The applied field  $\vec{E}$  further decreases the effective cathode work function:

$$\phi_{\text{eff}} = \phi_{\text{W,ZrO}} - \Delta\phi = \phi_{\text{W,ZrO}} - e\sqrt{\frac{e|\vec{E}|}{4\pi\epsilon_0}} \quad (5.1)$$

where  $e$  is the charge of the electron. At the tip of the cathode with radius  $r \leq 1 \mu\text{m}$ , the field strength is:

$$|\vec{E}| = V/r$$

where  $V$  is the applied voltage. For  $V = 10 \text{ kV}$ , creating a potential gradient of  $10^6 \text{ V/cm}$ , the change in work function is  $\Delta\phi \approx 0.4 \text{ eV}$ . The cathode is heated to  $1800K$ , where electrons have enough thermal energy to overcome this effective work function and form the electron beam used for imaging (see figure 5.2). The typical energy range used for imaging and analysis is  $E = 10 - 20 \text{ keV}$ , while the energy spread for beams produced by Schottky emission is  $\Delta E \approx 0.7 \text{ eV}$ .

Numerous interactions take place when a 10-20 keV electron beam strikes a solid material. Their energies and interaction volumes are depicted in figures 5.3 and 5.4. The beam electrons can scatter essentially elastically, losing at most a few eV in the process of changing direction; these redirected electrons are called “backscattered electrons” (BSE) and are detected by an annular semiconductor detector (green system in figure 5.1). Their energies range from 50 eV to that of the incident beam

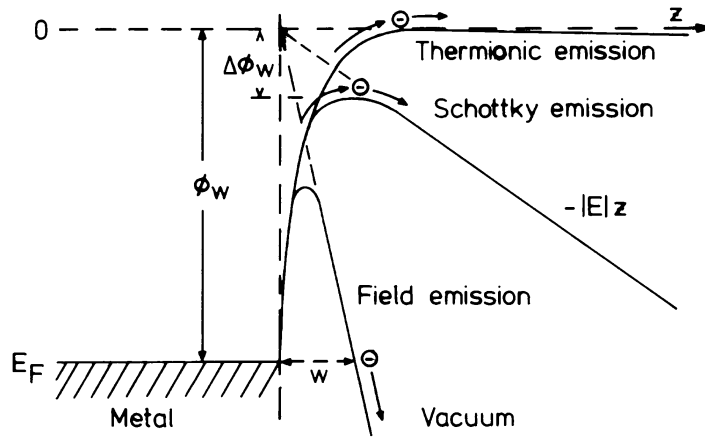


Figure 5.2: “Potential barrier (work function  $\phi_w$ ) at the metal-vacuum boundary and decrease of potential energy  $V(z)$  with increasing external field  $E$  for thermionic, Schottky and field emission.” [45]

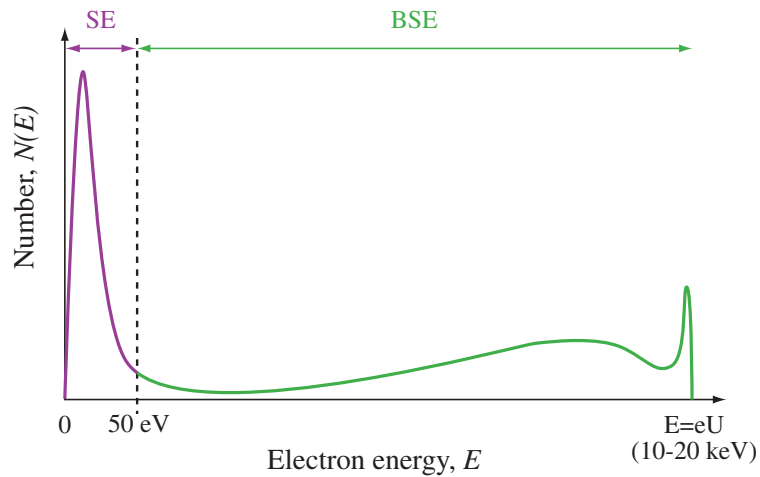


Figure 5.3: Energy distribution of electron interactions. Secondary electrons (SE), with a peak at 3-5 eV, are defined to be less than 50 eV. Backscattered electrons (BSE) have energies from 50 eV to the beam energy (usually 10-20 keV).

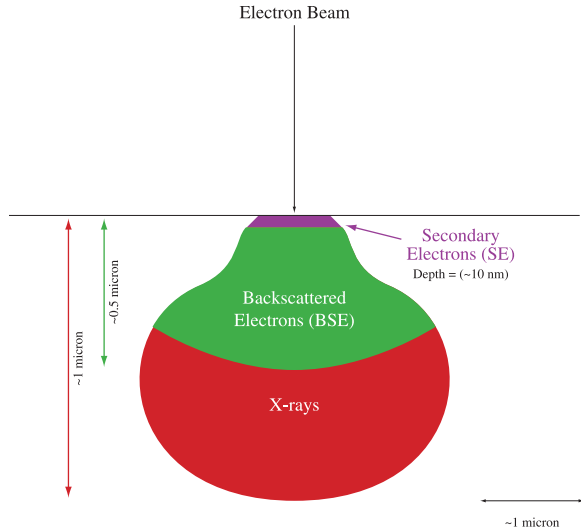


Figure 5.4: Interaction volumes for electron interactions.

(10-20 keV). The backscattered electrons can form diffraction patterns when emitted from the lattice, as discussed in subsection 5.1.4 below. Several inelastic processes involve a transfer of energy from beam to sample. Beam electrons can promote outer, more loosely-bound electrons from conduction to valence bands, creating “secondary electrons” (SE) with energies of a few eV which are detected by a combination of scintillator and photomultiplier tube (purple system in figure 5.1). If sufficiently energetic, beam electrons can ionize core electrons in the sample, causing other sample electrons to decay back to the ground state with concomitant emission of an X-ray photon with energy equal to that of the transition (usually keV). This discrete spectrum of X-ray peaks forms the basis for energy dispersive spectroscopy (EDS); the X-ray detection and analysis system is red in figure 5.1. Finally, beam electrons can simply be decelerated by Coulombic interactions with sample nuclei, creating a continuous spectrum of X-ray photons known as Bremsstrahlung radiation that provides an unwanted and unfortunately intrinsically unremovable background on any measurement of the discrete X-ray spectrum arising from electronic transitions. Any electrons and X-rays, including those generated by interactions, can in turn promote

or ionize other electrons, leading to multiple scattering and further complicating the resulting data. Independently observing the different interactions is not trivial, but because of the significant difference in energy scales of secondary and backscattered electrons (eV vs. keV), different types of interactions can be quantified independently by detectors built to be sensitive only to specific narrow energy ranges.

### 5.1.1 Secondary Electron (SE) Imaging

Secondary electrons are produced when beam electrons eject the weakest-bound outer valence electrons around sample nuclei. Because the beam electrons are so much more energetic (keV energy scale), they transfer energy inefficiently, and the resulting ionized secondary electrons have energies of only a few eV. Secondary electrons are defined to have a maximum of 50 eV; though backscattering produces a few electrons with energies this low, they are not numerous enough to be significant. Those secondary electrons with a kinetic energy greater than the work function of the sample can escape the surface and enter the vacuum chamber around the sample. Detecting these electrons forms the basis of the typical photograph-like scanning electron image. The fraction of beam electrons reemitted as secondary electrons is termed the secondary-electron yield and represented by the letter  $\delta$ .

The detector most commonly used to detect secondary electrons is quite similar to setups used in particle physics. The Everhart-Thornley (E-T) detector (see figure 5.5) consists of a scintillator coated with a few nanometers of conducting metal (to reflect any optical photons generated in the chamber by various luminescence processes), a light pipe and a photomultiplier tube (PMT). In front of the scintillator is a metal grid biased at +200 V relative to the sample; because the secondary electrons are of low energy ( $\leq 50$  eV), they can be redirected into the scintillator by the electric field created by the grid. With a much higher energy (into the ten keV range), the backscattered electrons emitted by the sample are not significantly deflected. Because the scintillator subtends a relatively small solid angle (compared to, for example,

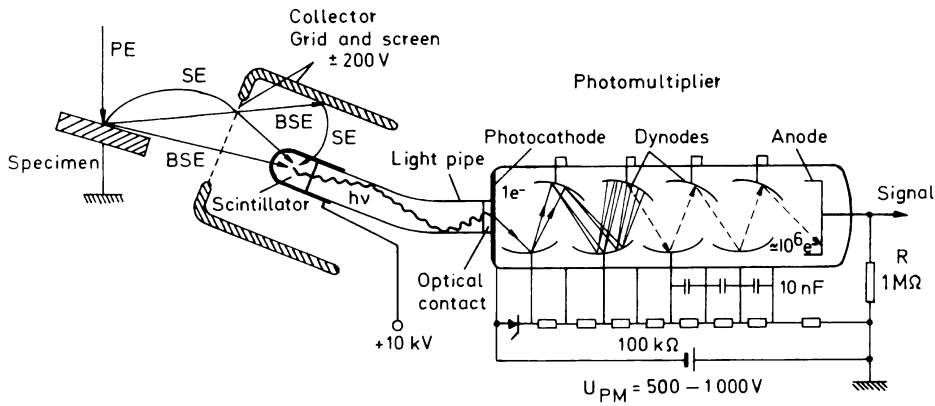


Figure 5.5: Everhart-Thornley detector for secondary electrons.[45]

the solid state backscattered electron detector described in subsection 5.1.2 below), few backscattered electrons contribute to the secondary electron count of the E-T detector. The conductive metal coating on the surface of the scintillator is biased at +10 kV relative to the grid to accelerate those secondary electrons passing through the grid into the keV energy range needed to activate the scintillator. This creates visible photons that propagate down the light pipe via total internal reflection, to be collected and further amplified by the photomultiplier tube. The final analog video signal detected and sent to the TV screen is a function of the number of secondary electrons collected (which is proportional to the secondary electron yield  $\delta$ ), as well as of more complicated intrinsic efficiency and yield factors for the detection system itself.

The secondary electron yield  $\delta$  is highly sensitive to the angle between beam current and sample, so imaging with secondary electrons provides a sensitive probe of sample topography. Although  $\delta$  depends on the atomic number  $Z$  of sample atoms, it does not vary with  $Z$  in a monotonic fashion (see figure 5.8) and is therefore not preferred to create maps of composition. Nevertheless, the combined advantages of easy high magnification and tremendous depth of field make secondary electron imaging the method of choice to produce “photograph-type” images of objects on the

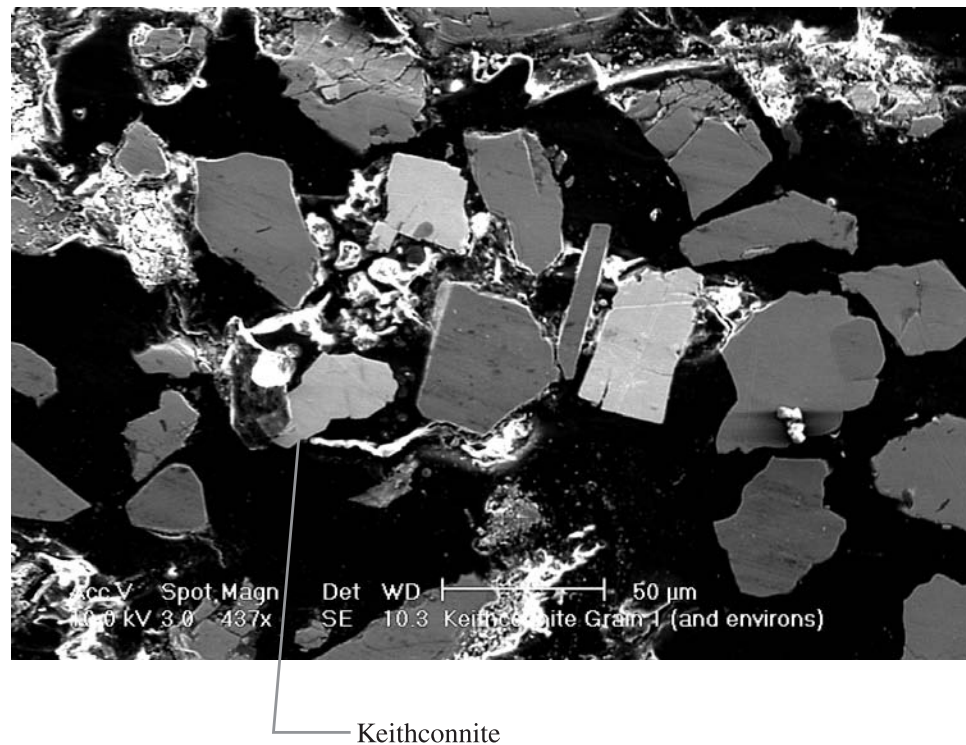


Figure 5.6: A secondary electron image of the mineral keithconnite.

micron scale or smaller, generally producing better images than even optical methods. Moreover, because the E-T detector is based on a photomultiplier tube, the typical response time of the system is on the order of tens of nanoseconds, making fast scan rates and real-time imaging possible.

As the most convenient general imaging technique, we used secondary electrons to quickly produce overall images of samples, for example the keithconnite in figure 5.6. Note that the central grain of keithconnite (marked with a gray line in the figure) is surrounded by a large number of other mineral grains.

### 5.1.2 Backscattered Electron (BSE) Imaging

A significant fraction of beam electrons undergo elastic scattering (single or multiple) and reemerge from the sample having scattered through a large net angle with negligible energy loss. They are detected with a crystal of doped silicon fashioned into a ring (see figure 5.7), essentially a giant biased p-n junction. The detector is situated so that the electron beam passes through the hole in its center, thereby detecting electrons that have scattered to an angle of nearly  $\pi$  radians. The surface area of a few  $\text{cm}^2$  gives a large solid angle. Because the band gap in silicon is about 3.6 eV, the dissipation of the 10 or so keV typically deposited by a backscattered electron will excite several thousand electrons in the silicon from valence to conduction band, created an equal number of holes. The silicon is biased to prevent recombination of holes and electrons; they drift to opposite ends of the crystal and collect on conducting electrodes. The total charge on the electrodes is then amplified and measured. Because detection of backscattered electrons relies on electrons drifting through a semiconductor, as opposed to the much faster movement of photons in the E-T detector for secondary electrons, the response time of the backscattered detector is much slower and thus requires a slower scan rate of the electron beam over a surface to produce an image.

Since the backscattered electrons have essentially the same energy as the beam, the current measured by the detector (and hence the intensity on the screen) is a function only of the number of electrons striking it, which itself is proportional to the fraction of the initial beam electrons that are backscattered. This fraction is called the backscattering coefficient  $\eta$  and is highly sensitive to both atomic number of the scattering nuclei and local sample topography. Because imaging with secondary electrons permits much faster scanning, it was used primarily for topographical imaging, with backscattered electron imaging reserved for looking at composition.

Over the full range of naturally occurring elements, the backscattering coefficient  $\eta$  increases monotonically overall, with a steeper slope for elements with atomic number

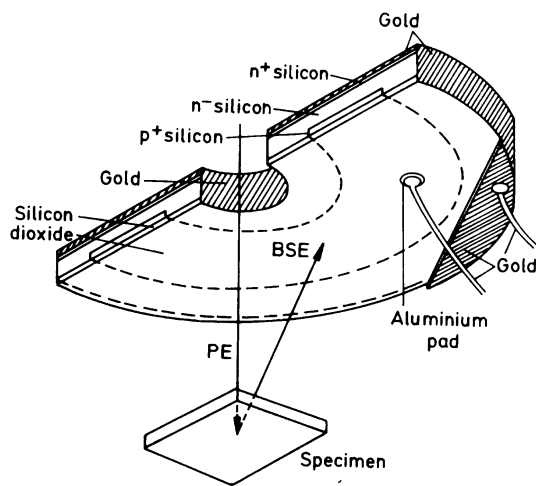


Figure 5.7: Annular silicon ring detector for backscattered electrons.[45]

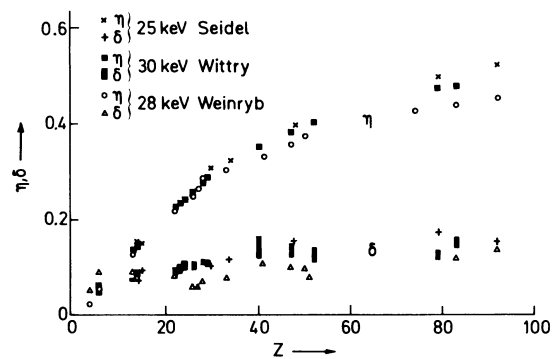


Figure 5.8: “Increase of the backscattering coefficient  $\eta$  and the secondary electron yield  $\delta$  of 25 – 30 keV electrons with increasing  $Z$ .”[45]

$Z < 50$  (see figure 5.8). The  $\eta$  vs.  $Z$  relation is not strictly monotonic, though, and a closer look reveals that occasionally an element has a slightly lower  $\eta$  than the adjacent lighter element. Very slight variations in  $Z$  are therefore somewhat unpredictable, though backscattered electron imaging is capable of distinguishing elements with atomic numbers separated by three or four. For compounds,  $\eta$  is proportional to a weighted average of the atomic numbers of the constituent elements. By polishing a surface the effects of topography can be removed; the backscattered image then represents a qualitative compositional map of a sample, with brightness proportional to atomic number. Using appropriate computer manipulations of the brightness and contrast, a selected range of elements can be visually highlighted as bright spots on screen, and their distribution throughout the sample can quickly be determined.

A backscattered electron image of keithconnite is given in figure 5.9, with brightness and contrast selected to display the palladium telluride as gray. The pair of bright white grains are the mineral galena ( $PbS$ ); because lead has a higher atomic number than palladium, the galena grains are brighter than the keithconnite. The remaining surrounding grains present in figure 5.6, composed primarily of lighter elements such as silicon and oxygen, have disappeared into the black background.

Backscattered electron imaging indicates only average atomic number through brightness information. To determine the elemental composition, the X-rays emitted by the sample can be examined using energy-dispersive scattering. This was used to identify the grains in figure 5.9.

### 5.1.3 Energy-Dispersive Spectroscopy (EDS)

Typical 10-20 keV beam electrons are sufficiently energetic to ionize an inner core electron from most elements. When this ionization occurs, another higher-energy electron falls back down to take its place, returning the atom to the ground state and emitting a photon with an energy equal to the transition. The photon is also in the keV range, and hence is an X-ray photon. Many different electronic transitions in an

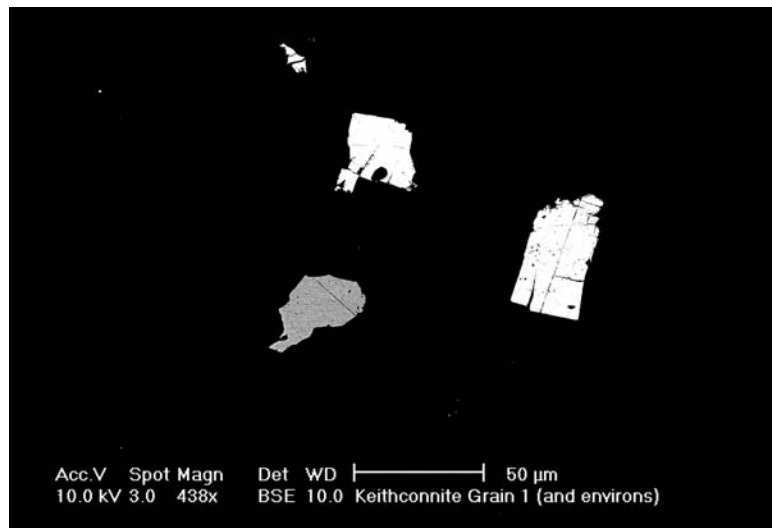


Figure 5.9: A backscattered electron image of the mineral keithconnite. The two brighter grains toward the upper right corner of the image are lead-bearing galena.

atom can produce these X-rays, and the ensemble of such transitions is unique to each element. Every element therefore has a unique spectrum of emitted X-rays, a spectral fingerprint, by which it can be identified. There are two ways to detect and characterize X-rays physically, based either on their wavelength or their energy. Like most SEMs, the Princeton machine relies on the latter method, called energy-dispersive spectroscopy (EDS). EDS can be performed either by fixing the electron beam over a spot in the sample, giving a compositional analysis of the X-ray interaction volume around that spot (see figure 5.4), or by scanning a field of view, giving an average composition for the whole field.

The X-ray detector used in energy-dispersive spectroscopy is a pure crystal of silicon which acts as an intrinsic semiconductor (see figure 5.10). Upon entering the Si crystal, an X-ray generates an electron via the photoelectric effect. This electron then transfers most of its energy in creating thousands of electron-hole pairs. Because backscattered electrons can also generate electron-hole pairs, a magnetic field is created in front of the EDS detector to deflect any incoming electrons; X-rays carry

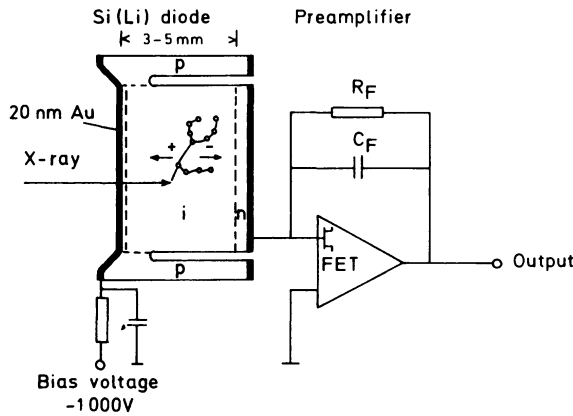


Figure 5.10: Silicon detector for energy-dispersive spectroscopy of X-rays.[45]

no charge and are unaffected by the field. The Si crystal is under an applied bias, so the electrons and holes are pulled in opposite directions and are collected at the edges of the crystal to form a charge pulse. The pulse is then converted into a voltage using a charge-to-voltage converter in the form of a field-effect transistor; the height of the output voltage pulse is therefore proportional to the incident photon energy. These voltage pulses are then fed into a computerized multi-channel analyzer, which histograms the pulses and outputs a spectrum of counts vs. incident photon energy.

When this histogram is plotted, the characteristic spectra of elements can be identified, and the relative heights of the tallest peaks give an approximate measure of the relative abundance of the elements present. Extracting quantitative data on elemental composition is complicated; the quick matter-of-minutes measurements are accurate to probably no better than 5%, but for our purposes of rough phase identification, exact composition information is unnecessary and the fast measurements are entirely sufficient. The EDS spectra for keithconnite is given in figure 5.11.

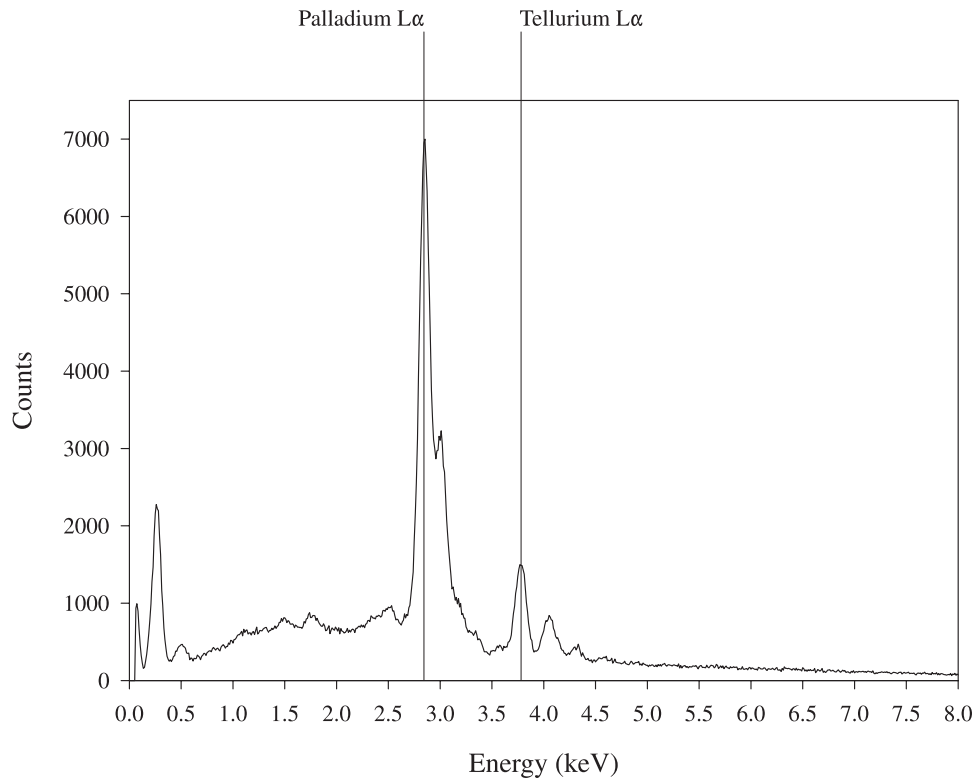


Figure 5.11: Energy-dispersive spectroscopy spectrum of keithconnite. The  $L\alpha$  lines for palladium and tellurium are marked. The peak around 0.3 keV originates from the carbon coat put over the sample to increase conductivity.

#### 5.1.4 Backscattered Electron Diffraction

By fixing the electron beam over a spot in the sample, the spatial distribution of backscattered electrons can be observed. This distribution is diffuse and continuous, except where the scattering vector (see figure 2.2 in chapter 2) is equal to a vector in the reciprocal lattice. Under these circumstances, the electron will Bragg scatter, creating a series of dark lines in the otherwise uniform electron backscattering pattern (EBSP). These lines are known as Kikuchi bands, and reflect the underlying symmetry of the lattice; an  $n$ -fold rotation axis is manifest as  $n$  lines intersecting at equal angles.

Inside the SEM, the sample is tilted to a large angle (often 70 degrees) so that the detector can image most of the backscattering pattern; the geometry of this setup is

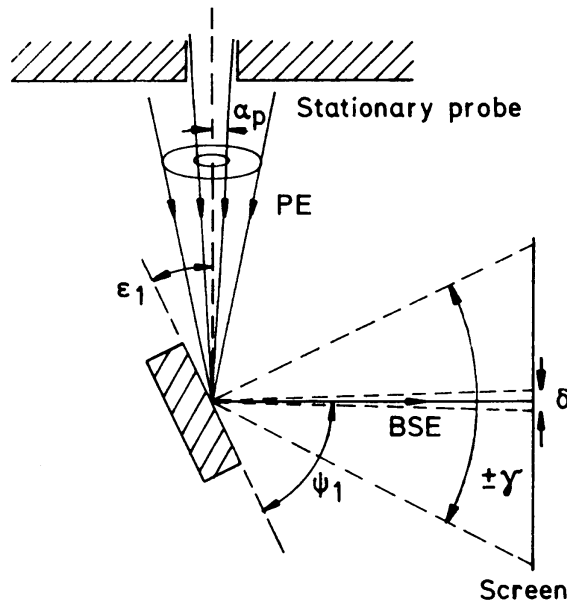


Figure 5.12: Electron backscattering diffraction pattern detector.[45]

shown in figure 5.12. The detector consists simply of a phosphor screen excited when electrons strike it and a low-level video camera to record the image. The electron backscattering pattern for an AlCuFe icosahedral quasicrystal is shown in figure 5.13. A secondary electron image of the surface from which the pattern was taken is shown in figure 5.14.

### 5.1.5 Combining Imaging Modes

The scanning electron microscope is a tremendously powerful tool for rapid identification and characterization of microscopic phases in macroscopic samples. Several of the minerals we examined occurred as  $10 \mu m$  grains in cm-sized samples. Under optical microscopy, these grains were exceedingly difficult to see, and probably impossible to characterize by traditional chemical means. With the SEM these grains could be located and identified quickly. When the backscattered electron detector

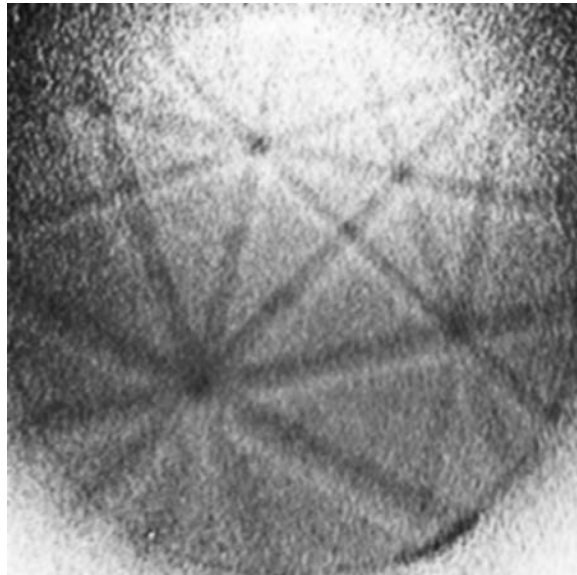


Figure 5.13: Electron backscattering diffraction from an AlCuFe icosahedral quasicrystal. A five-fold axis of symmetry is visible in the lower left-hand corner.

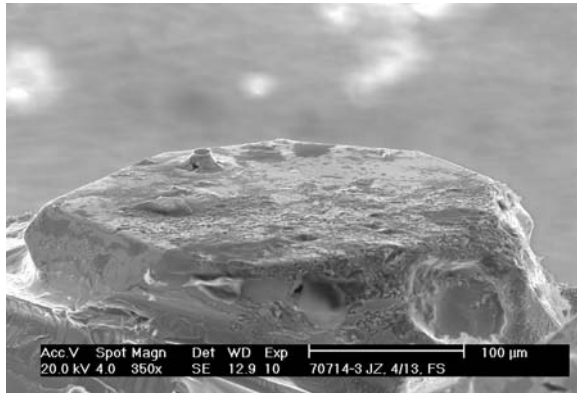


Figure 5.14: Secondary electron image of the surface of the AlCuFe icosahedral quasicrystal from which the diffraction pattern in figure 5.13 was taken.

was tuned to the appropriate brightness and contrast settings, all regions of a sample having an average composition with a high atomic number stood out as bright white dots on the screen. Each of these bright dots was analyzed with energy-dispersive spectroscopy to determine approximate elemental composition, in a few seconds indicating whether the desired compound had been located. Then, electron diffraction could be performed on the same region, yielding structure and symmetry information. Because all of the detectors are fixed in the microscope (only the beam and sample stage can move), the same area under the same conditions can be imaged and characterized with all of the techniques. There is perhaps no other combination of techniques quite so powerful and effective for the task of locating and characterizing micron-scale features in a macroscopic slice of host rock.

### **5.1.6 Artifacts: Charging**

A number of effects can distort an SEM image, including inherent limitations due to quantum mechanical or geometric effects, inhomogeneities in the microscope itself, contamination and sample problems. We encountered only one significant problem frequently in the course of our investigation, namely that of the buildup of electrons on the surface of a poorly conducting sample, creating the phenomenon known as “charging.”

Though imaging techniques are based on the relatively small fraction of reemitted charge created by beam electrons, most of the beam electrons lose their energy and are ultimately captured by the sample. If the sample conducts and a suitable conduction path is present, this charge will flow to ground; on the other hand, if there is no such path (either because the sample is insulating or the connection with ground is broken), charge will quickly build on the sample surface, creating an electric field which reflects beam electrons. Because successive sample regions are bombarded with electrons in the process of scanning, the local charging is a constantly changing phenomenon. Charging creates large high contrast regions in an image, which are

completely an artifact. Because the conductivity of the samples cannot be controlled (because we are examining natural materials), the only way to decrease or eliminate charging is to coat the sample with a thin layer of a conducting material. Because it is much lighter than the elements we were interested in detecting, we coated our samples with carbon as to not interfere with the EDS detection.

## 5.2 Transmission Electron Microscopy

In transmission electron microscopy, electrons penetrate a thin sample to form an image. A basic schematic of a transmission electron microscope (TEM) is shown in figure 5.15.

The TEM at the Princeton Materials Institute has an electron gun utilizing Schottky emission, similar to that in the SEM described above. Typical energies of the electrons at the cathode are 100 keV to 1 MeV. The electron beam from the electron gun is directed by various electron lenses *through* the thin sample, where it diffracts. Depending on the configuration of the objective and projector lenses below the sample, the final image on the viewing screen can represent either a direct image of the sample (usually at a high enough magnification to view the lattice directly), or a far-field diffraction pattern.

To prepare a sample for transmission electron microscopy, a macroscopic material is pulverized into micron-sized or smaller grains. Multiple scattering makes significantly thicker pieces of material opaque to the electron beam in the microscope. The grains are then spread out on a sample holder and inserted into the microscope. A diffraction pattern will best display the symmetry of a lattice when the electron beam axis is aligned with a lattice symmetry axis. This can be achieved by tilting the stage. An electron diffraction pattern taken in the TEM of the AlCuFe icosahedral quasicrystal shown in figure 5.14 is shown in figure 5.16.

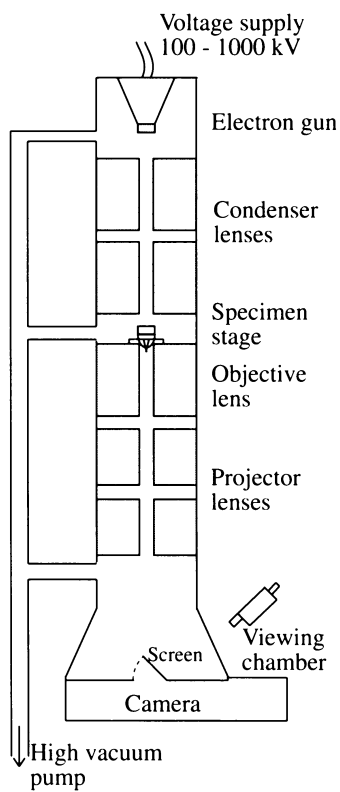


Figure 5.15: Diagram of the basic parts of a transmission electron microscope. Not to scale.[44]

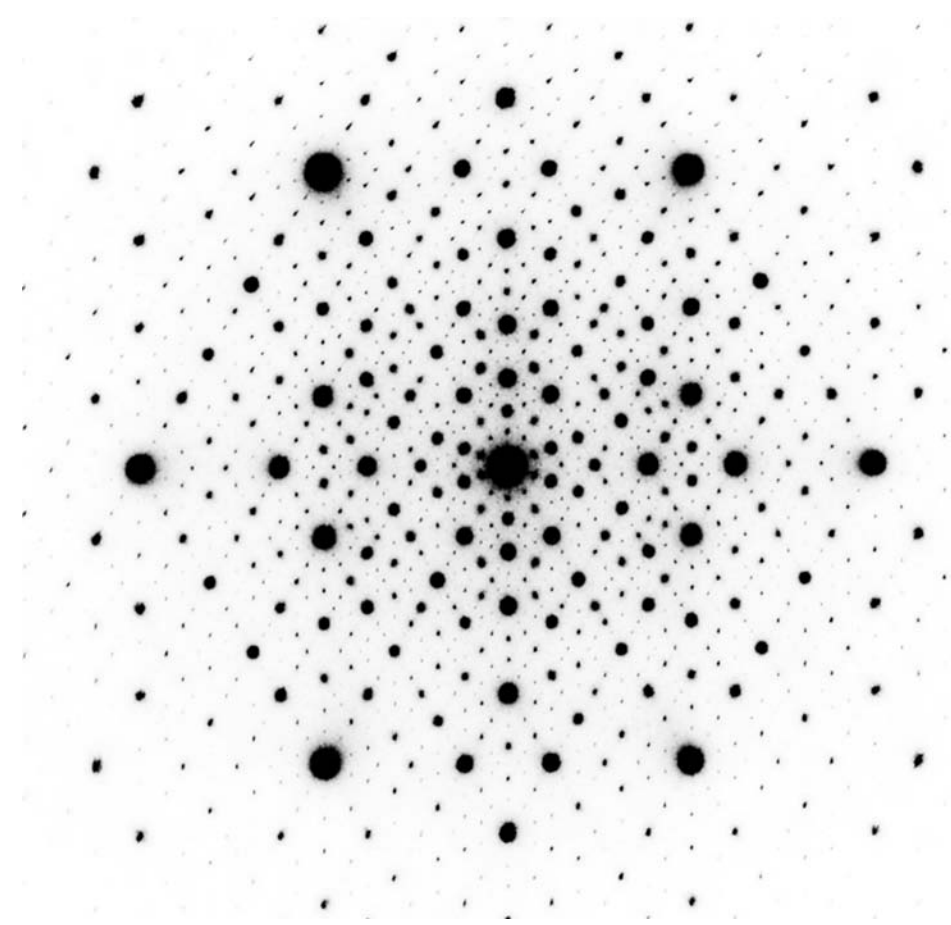


Figure 5.16: Electron diffraction pattern along a two-fold axis of an AlCuFe icosahedral quasicrystal.



# Chapter 6

---

## Experimental Results

The search through the Powder Diffraction File produces a list of the top quasicrystal candidates among natural minerals (see chapter 4). The top candidates are listed in table 6.1. The next step is to take samples of candidates into the laboratory to examine with electron microscopy, using the techniques described in chapter 5. A number of these minerals are exceedingly rare, and difficulties in acquiring samples has slowed the laboratory phase of our investigation. As a result, only four compounds have been analyzed: krennerite, theophrastite, its synthetic equivalent ( $\text{Ni(OH)}_2$ ), and volynskite.

Most of the experimental effort was devoted to krennerite, the most thoroughly analyzed of the four compounds. Electron diffraction strongly indicates that krennerite is incommensurately modulated in at least one dimension. Although this is not exactly what the program seeks, as true quasicrystals must have at least two incommensurately modulated dimensions, it is nonetheless quite significant. Only one other incommensurately modulated mineral is known, calaverite. Moreover, because the search program implicitly selects for the presence of certain specific irrational ratios present among powder pattern peaks, Krennerite may have an incommensurate ratio related to that in the icosahedral quasicrystals.

The remaining three minerals have only recently been acquired. Only very preliminary SEM and TEM studies have been performed on these.

PDF No.	Name	Formula
140117	Theophrastite	$\text{Ni}(\text{OH})_2$
020612	Krennerite	$(\text{Au},\text{Ag})\text{Te}_2$
181173	Volynskite	$\text{AgBiTe}_2$
461355	Miargyrite	$\text{AgSb}(\text{S},\text{Se})_2$
250405	Haxonite	$(\text{Fe},\text{Ni})_{23}\text{C}_6$
011281	Covellite	$\text{CuS}$
360387	Cabriite	$\text{Pd}_2\text{SnCu}$
020318	Sulfohalite	$2\text{Na}_2\text{SO}_4\text{ClF}$
021145	Allargentum	$\text{Ag-Sb}$
021293	Nicolite	$\text{NiAs}$

Table 6.1: Top ten mineral candidates for quasicrystallinity.

## 6.1 Krennerite, $(\text{Au},\text{Ag})\text{Te}_2$

Krennerite was the first mineral on the list analyzed, primarily because macroscopic samples from Cripple Creek, Colorado were already available in the Princeton University mineral collection. Samples were first analyzed quickly in the scanning electron microscope using energy-dispersive spectroscopy to confirm approximate stoichiometry. Then imaging and diffraction were performed in the transmission electron microscope. An image of our krennerite sample, in which the lattice is visible, is provided in figure 6.1.

Electron diffraction strongly suggests that krennerite is an incommensurate crystal. To the best of our knowledge, it is second known incommensurate mineral, after calaverite, a related gold telluride.

Indexing the faces of calaverite was an outstanding problem in crystallography for nearly a century. A number of papers in the first decade of the twentieth century detailed the large number of forms adopted by calaverite, of which only a small fraction could be indexed with three indices unless a complicated twinned structure of no less than four interpenetrating lattices was assumed. An exhaustive examination

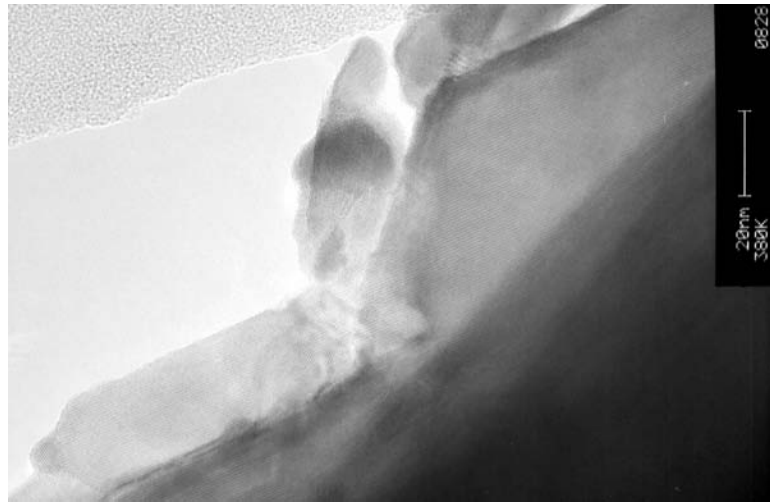


Figure 6.1: Transmission electron microscope image of the Krennerite lattice. The material in the upper left corner is amorphous carbon on the sample holder.

of 105 different high quality crystals by Goldschmidt, Palache and Peacock in 1931 confirmed the four penetrating lattice requirement, and even then, not all crystal forms could be indexed.[47] The problem remained unsolved until the mid-1980s, when the notions of incommensurate lattices suggested that the crystal may be a projection of a higher dimensional lattice. In a 1985 *Physical Review Letter*, Dam, Janner and Donnay proposed a four-dimensional structure for calaverite, and were able to index all of the faces of a calaverite crystal using four basis vectors.[46] This fourth basis vector is an irrational linear combination of two lattice vectors. Janner and Dam extended their work in 1989 to index all 105 calaverite crystals in the 1931 paper by Goldschmidt et al. using the four basis vectors; they could thus reconstruct the entire higher-dimensional reciprocal space of calaverite.[48]

One of the most distinctive features of the calaverite diffraction pattern indicating incommensurability is the presence of a large number of so-called “satellite peaks,” smaller less intense peaks surrounding each of the main peaks in the pattern (see figure 6.2).

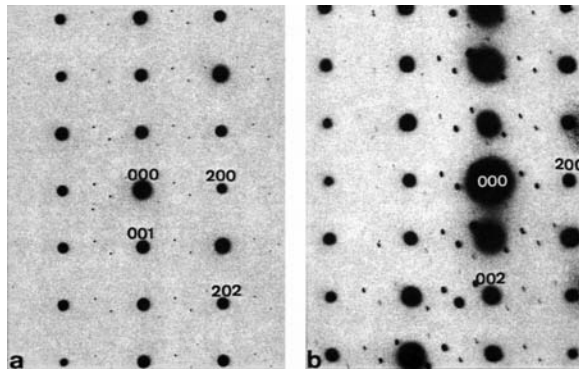


Figure 6.2: Electron diffraction pattern of calaverite, with several satellite peaks surrounding each major crystal peak. From [50], inverted (light and dark reversed) for clarity.

Krennerite was previously thought to be commensurate.[52] Our electron diffraction patterns seem to indicate otherwise. Much in the same way as calaverite (compare figure 6.2), krennerite's likely incommensurability is manifest in the diffraction pattern as a series of “satellite” peaks surrounding each main peak (see figures 6.3, 6.4 and 6.5). Because of the finite density range of the film and scanner, only a finite number of satellite peaks are visible, but in theory, the process of decreasing brightness and increasing contrast should allow an infinite number of progressively weaker satellite peaks to become visible. Figures 6.3, 6.4 and 6.5 are three different images of the same scan of an electron diffraction pattern taken of a two-fold rotation axis in the krennerite lattice, each figure printed with different brightness and contrast settings for the whole image. Figure 6.3 is closest to the original film in brightness and contrast, and the main peaks are visible as black dots arranged in parallel rows. Satellite peaks are visible as lighter dots around each of the main peaks. In 6.4, more satellite peaks become visible as the original peaks blur out. The effect is further intensified in figure 6.5. The reciprocal space thus appears to be a quasilattice. However, until a fourth vector is determined and the entire reciprocal space mapped, the conclusion that krennerite is an incommensurately modulated structure must remain

preliminary.

Krennerite does not have crystallographically forbidden symmetry, and its modulation appears to be in one dimension only. It is therefore an incommensurate crystal, as opposed to a quasicrystal, which requires at least two incommensurately modulated dimensions. However, because the search program implicitly targets only a certain finite set of incommensurate ratios, not all incommensurately modulated crystals will be identified as top candidates. The incommensurate ratio must be close to one of these special cases, which suggests that Krennerite may be a system attempting to be quasicrystalline and that under slightly different conditions the incommensurability might extend to two dimensions and create a quasicrystal. This is potentially interesting and worthy of further investigation.

## 6.2 Other Studies

The other three samples have only recently arrived. Analysis has begun but the current results are very preliminary.

### 6.2.1 Ni(OH)<sub>2</sub>: Synthetic and Natural Theophrastite

The diffraction pattern in the Powder Diffraction File for theophrastite was taken from a synthetic sample of Ni(OH)<sub>2</sub>. We performed electron diffraction on synthetic Ni(OH)<sub>2</sub> from Aldrich Chemical Company, Inc. (catalog number 28,362-2). The compound occurred as a light green powder, which when examined in the TEM, was seen to be polycrystalline, with extremely small crystalline domains with sizes in the tens of nanometers range (see figure 6.6). In order to image a clear diffraction pattern, a single crystalline domain must have a volume of at least (100 nm)<sup>3</sup>. An electron diffraction image could not be obtained from a single grain, since these grains were too small. Instead, the image reflects contributions from grains spanning many different orientations. As a result, the electron diffraction image from synthetic Ni(OH)<sub>2</sub> is

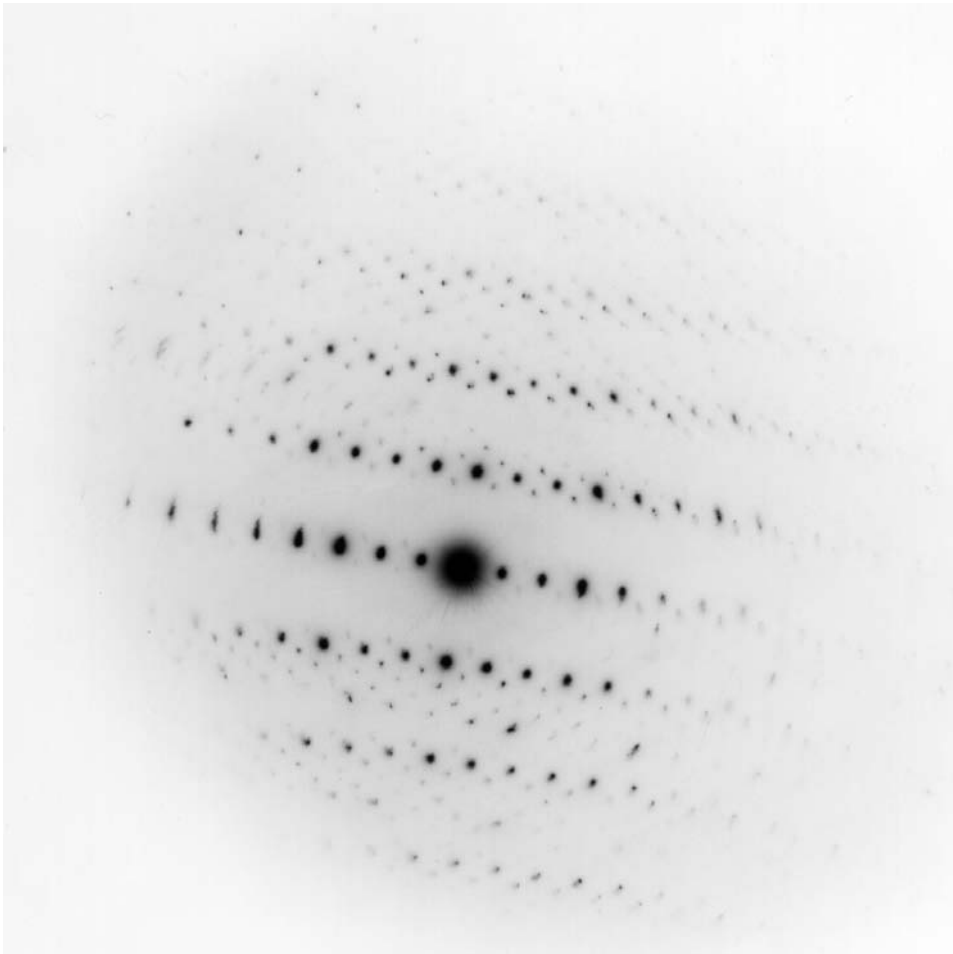


Figure 6.3: Electron diffraction pattern from the Krennerite lattice.

effectively a powder pattern, with rings instead of spots (see figure 6.7).

We also examined natural Theophrastite from the Vermion district, Macedonia, Greece in the TEM. There appears to be a mixture of phases within the sample, though some early electron diffraction results seem to indicate that one of these phases is hexagonal, in agreement with the published structure. A clear diffraction pattern demonstrating the hexagonal symmetry has not yet been obtained. Theophrastite is an important phase to investigate because it seems to be “hoaxing” the program. It passes several of our screening criteria, some as well or better than the known

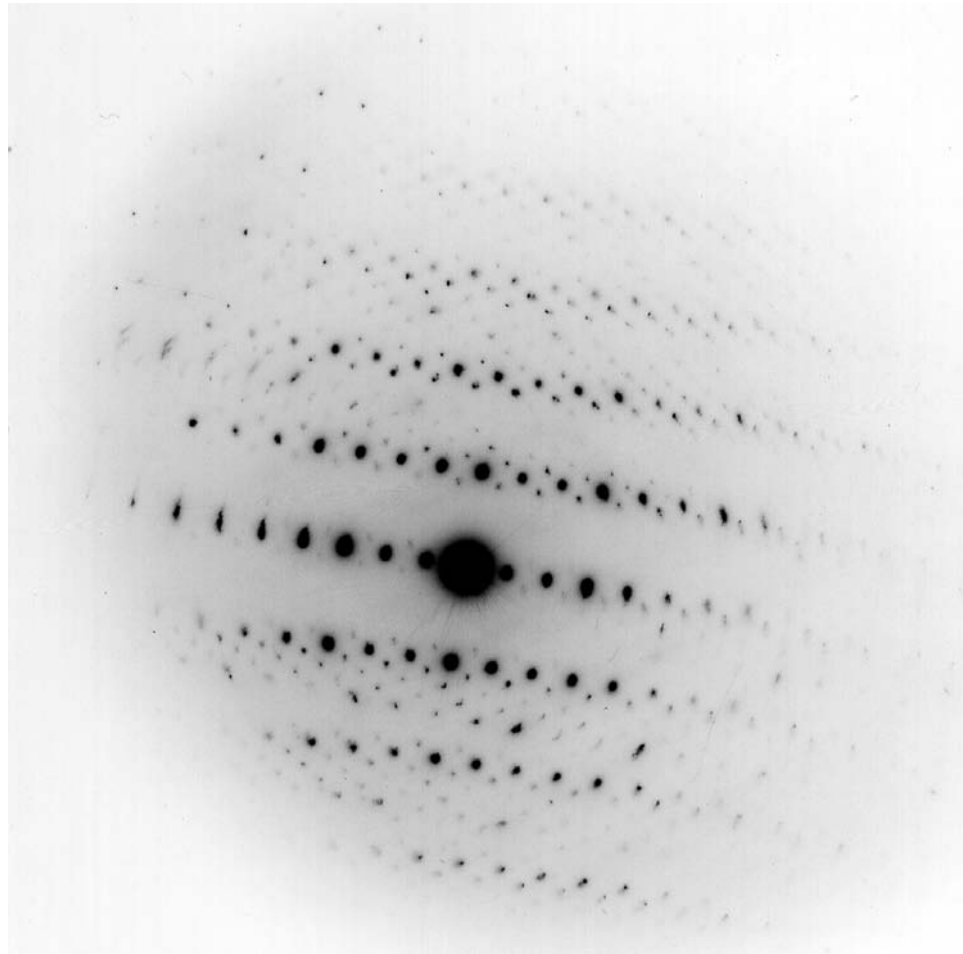


Figure 6.4: Electron diffraction pattern from the Krennerite lattice. This is the same original image as figure 6.3, except that the brightness has been decreased and contrast increased to highlight weaker peaks.

quasicrystals (compare tables 4.3 and 4.2). However, both three-dimensional hexagonal basis vectors (a periodic lattice) and six-dimensional icosahedral basis vectors (a quasiperiodic lattice) index the powder pattern equally well. It may be that theophrastite is a completely normal hexagonal crystal that happens to mimic an icosahedral phase in its powder diffraction to better than 0.05% between ideal icosahedral  $|\vec{Q}_{\parallel}|$  and real  $|\vec{Q}_{\parallel}|$  for *every* peak in its pattern. The search program simply cannot determine whether theophrastite is a better crystal or quasicrystal using the

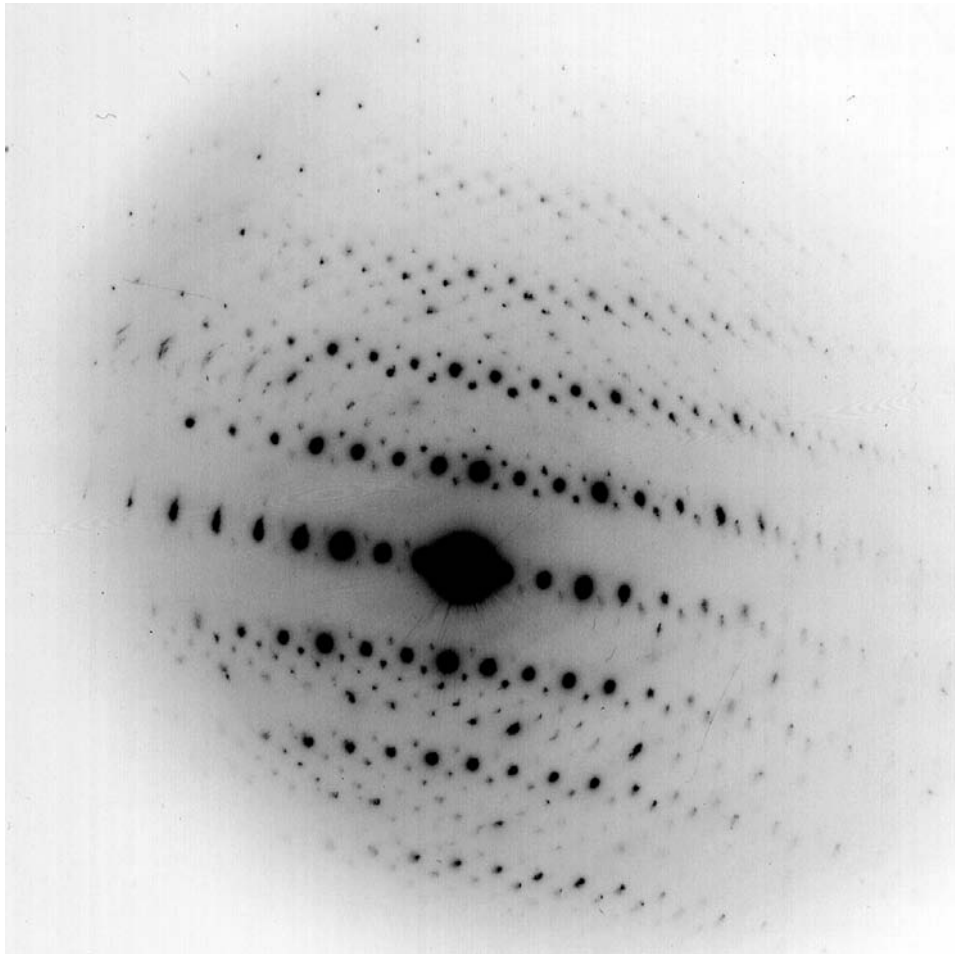


Figure 6.5: Electron diffraction pattern from the Krennerite lattice. Relative to figure 6.4, the brightness has been further decreased and contrast further increased.

current set of tests, and it may be that in this case a crystal phase is hoaxing the program into thinking that it is a quasicrystal. Given a sample size of only 7000 minerals, the existence of a pattern with this level of mimicry is certainly not expected. Further examination with electron diffraction may clarify the situation by determining the structure and chemical composition of the unknown phase, as well as determining if theophrastite itself is truly hexagonal.



Figure 6.6: Transmission electron microscope image of synthetic  $\text{Ni}(\text{OH})_2$  from Aldrich Chemical Company. The typical grain size is  $\approx 10 - 50 \text{ nm}$ .

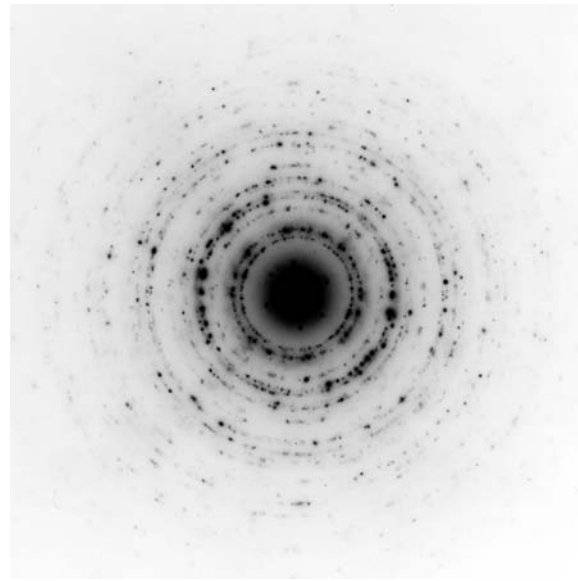


Figure 6.7: Electron diffraction image of synthetic  $\text{Ni}(\text{OH})_2$ . The diffraction pattern could not be obtained from individual crystal grains, since they were too small. The image reflects contributions from grains spanning a number of orientations. Consequently, there are rings instead of a set of discrete points.

### 6.2.2 Volynskite, AgBiTe<sub>2</sub>

Volynskite from Baiwa, New Zealand was examined in the scanning electron microscope. The mineral occurred as a 5 by 10  $\mu\text{m}$  grain embedded in a much larger grain of silver telluride. In the secondary electron image (figure 6.8), the grain of volynskite is indistinguishable from the surrounding silver telluride. In the backscattered secondary image (figure 6.9), however, the volynskite is clearly visible and distinct. The presence of bismuth ( $Z = 83$ ) increases its average atomic number, so it is brighter in the backscattered electron image. The spectra from the energy-dispersive spectroscopy analysis are included in figures 6.10 and 6.11. Preliminary attempts were made to perform electron diffraction from the volynskite, but it has not yet been successfully imaged due either to sample charging, surface roughness, or both. The sample was coated with a thin layer of amorphous carbon to reduce charging, and the next step is simply to continue attempting to produce a backscattered electron diffraction pattern.

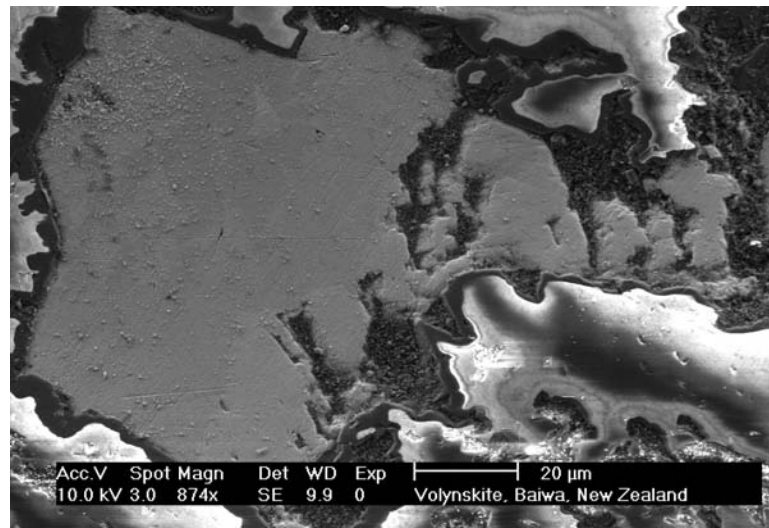


Figure 6.8: Secondary electron image of a silver telluride grain in host rock from Baiwa, New Zealand. No volynskite grain can be seen using this imaging technique (compare figure 6.9). The rounded features in the upper and lower right corners of the image are artifacts of charging.

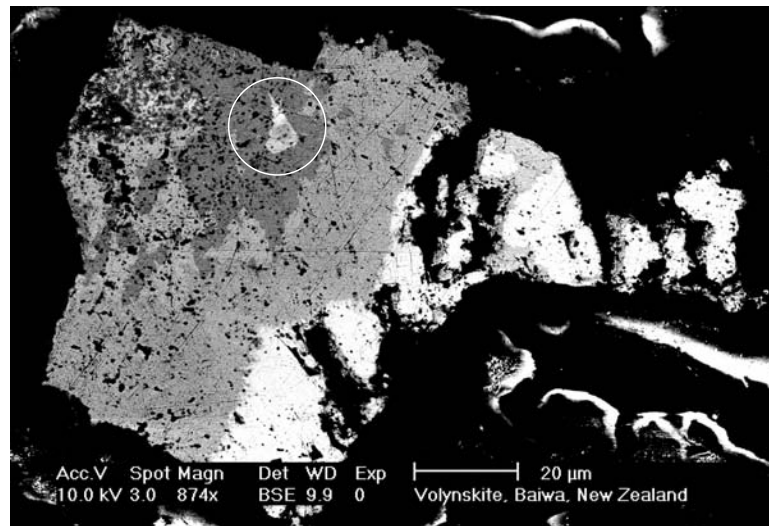


Figure 6.9: Backscattered electron microscope image of volynskite (circled in white) embedded in a silver telluride grain in host rock from Baiwa, New Zealand.

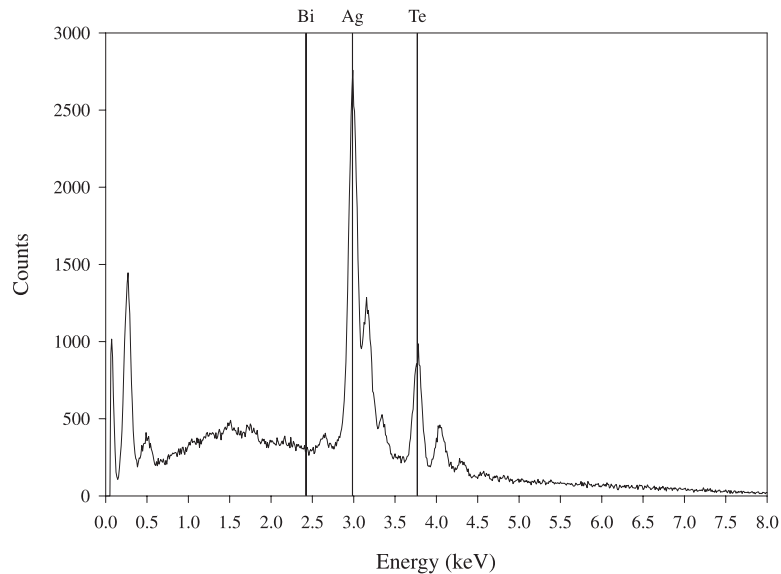


Figure 6.10: Spectrum from energy-dispersive spectroscopy analysis of the large silver telluride grain in figure 6.9. *Bi*, *Ag*, and *Te* mark the positions of the Bi- $\text{M}\alpha$ , Ag- $\text{L}\alpha$  and Te- $\text{L}\alpha$  transition lines. There is no peak around the *Bi* line.

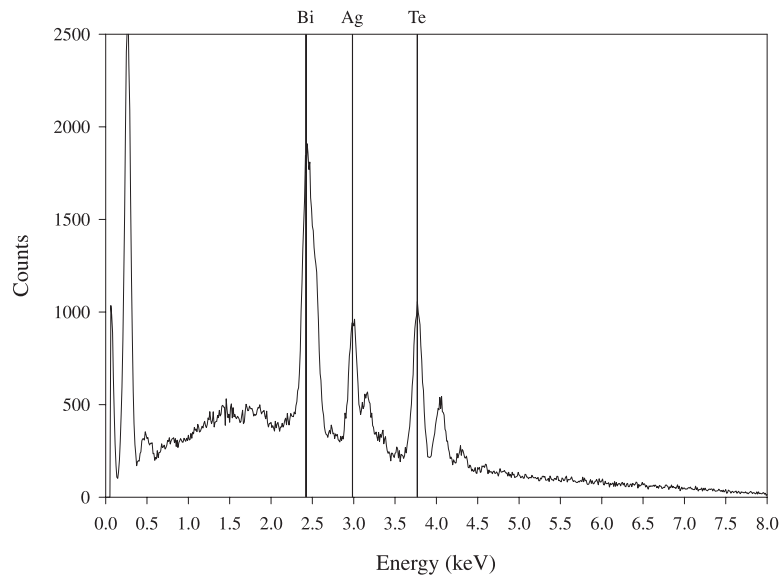


Figure 6.11: Spectrum from energy-dispersive spectroscopy analysis of the small volynskite grain circled in figure 6.9. *Bi*, *Ag*, and *Te* mark the positions of the Bi- $\text{M}\alpha$ , Ag- $\text{L}\alpha$  and Te- $\text{L}\alpha$  transition lines.

## Chapter 7

---

# Conclusions and Directions for Future Research

Historically, the known quasicrystals have been found by serendipity. This thesis is aimed at developing a more informed, systematic approach by utilizing the known quasicrystals diffraction properties to design a computerized search for new quasicrystals based on powder diffraction data. The project takes advantage of the Powder Diffraction File, a collection of about 70,000 x-ray powder diffraction patterns. A list of top candidate minerals and synthetic compounds were identified which most closely match the powder patterns of an ideal simple icosahedral quasicrystal.

One goal of the investigation is to determine if there are any natural minerals which are quasicrystals. Perhaps previously unknown quasicrystals may be found among synthetic materials, as well. Even if quasicrystals are not found, the search may reveal systems and compounds which form good approximants to quasicrystals. Among the known quasicrystals, slight variations in stoichiometry cause the solid to transform from a quasicrystal to an approximant phase. Identifying near-approximants in the Powder Diffraction File provides a list of systems that warrant further investigation in the laboratory where a range of stoichiometries near the listed one can investigated to look for new quasicrystal phases.

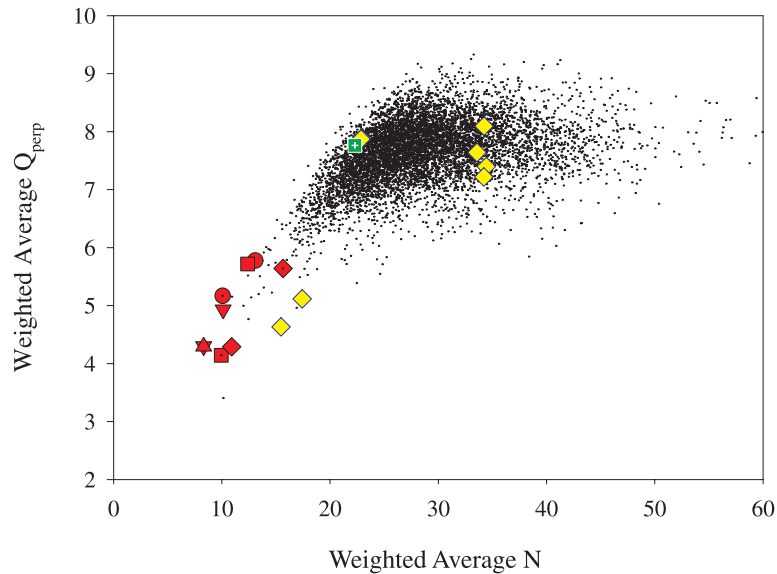


Figure 7.1: Scatterplots of  $N$  vs.  $|Q_{\perp}|$  based on averages weighted by  $\sqrt{I}$ .

## 7.1 Conclusions

### 7.1.1 Computer Programs

A key issue in developing a search for quasicrystals in the Powder Diffraction File is to determine just what can be learned about quasicrystals from their powder diffraction patterns. That quasicrystals can be identified based on their powder patterns is not *a priori* obvious. Because powder diffraction averages the reciprocal lattice over all orientations, the crystallographically-forbidden symmetry that most distinguishes the quasicrystals cannot be observed directly. Nevertheless, for the case of the simple icosahedral quasicrystal, based on both the automated reproduction of the published indexings of early quasicrystals (see Appendix A) and the separation of quasicrystals in the scatterplots of data generated by our program (see e. g. figure 7.1, a copy of the top plot in figure 4.11), we believe that we have developed a reliable test for identifying quasicrystals and the most promising near-quasicrystals based on powder patterns alone.

The current program still has several weaknesses. It may be vulnerable to crystal “hoaxing,” crystal phases whose powder patterns accidentally match the icosahedral quasicrystal powder pattern. Theophrastite is an interesting example because its powder pattern indexes as a hexagonal crystal and as an icosahedral quasicrystal equally well. An experimental investigation is underway to decide which phase is the correct description. If it is a hoax, it is worth close study to determine the best methods of distinguishing hoaxes from real quasicrystals.

All of the perfect or nearly perfect simple icosahedral quasicrystals can pass our battery of tests with excellent statistics as shown in table 4.2. Mediocre or strained quasicrystals, on the other hand, are inseparable from the rest of the compounds in the powder data; see, for example, the positions of the majority of the yellow diamonds and green square in figure 7.1. Our program would have completely missed Schechtman’s discovery pattern from the original aluminum manganese alloy (the green square in figure 7.1) because the sample quality was poor.[38]

### 7.1.2 Experimental Investigation

The combination of secondary electron imaging, backscattered electron imaging and energy dispersive spectroscopy is a powerful and effective method for locating micron-sized grains. The lattice structure of these grains can then be probed *in situ* by electron diffraction within the scanning electron microscope, a phase of the investigation just beginning. For pure isolated samples, electron diffraction in the transmission electron microscope is the technique of choice for lattice structure analysis, and has already turned up several interesting results.

At present, there are no known naturally-formed quasicrystals. The search based on powder diffraction data relies on checking leading candidates in the laboratory and finding the three-dimensional diffraction pattern. Since the experimental tests require samples of materials which are often rare, only a few leading candidates have been examined thus far. Among these, krennerite has proven to be an interesting case

since our experimental investigation suggests that it is an incommensurately modulated crystal, a quasiperiodic solid closely related to quasicrystals. Up to this point, only one example of an incommensurate crystal was known among the natural minerals, calaverite. Systematically investigated in the mid-1980s, its four-dimensional reciprocal lattice and basis vectors have been fully determined.[46][48] Its diffraction patterns have a distinctive group of weaker satellite peaks around each bright crystal peak. Similar features occur in our electron diffraction patterns of krennerite, compositionally similar to calaverite. Although krennerite was previously thought to be commensurate,[52] our electron diffraction results (see, for example, figure 6.3) strongly suggest that krennerite is incommensurately modulated, only the second natural mineral to be identified as such.

By comparing with the simple icosahedral quasicrystal pattern, the search program automatically selects for certain specific irrational ratios involving  $\tau$  among the peaks of a powder pattern. Because there are no constraints on the ratios in a one-dimensional incommensurately modulated crystal, there is no reason to expect the search program in general to select incommensurate phases. In the case of the krennerite, that the program did identify it as a top candidate indicates that the relations among its peaks include at least some of the specific ratios of the icosahedral case. This suggests that Krennerite may be a system attempting to be quasicrystalline and that under slightly different conditions, the incommensurability might potentially extend to two or three dimensions resulting in a proper quasicrystal.

## 7.2 Directions for Future Research

There are several clear directions for future research, both in search program development and laboratory investigation.

A successful computer search method has not yet been developed for any type

of quasicrystal structure other than the simple icosahedral case. Whether an effective search can be done outside the simple icosahedral case is still an open question. Because the basis vectors for the face-centered and body-centered icosahedral quasicrystals are linear combinations of the basis vectors of the simple icosahedral case, modifying the code of the current program to accommodate other icosahedral quasicrystalline structures should be relatively straightforward. However, there are very few published indexings of face-centered icosahedral reciprocal lattices and even fewer in the case of body-centered icosahedral. Checking the search program results with the published indexings was an exceedingly valuable guide in developing the screening criteria for the simple icosahedral case, and the absence of published indexings for other structures is likely to complicate the development of accurate screening criteria.

Moreover, the search for a decagonal phase and other phases with two quasiperiodic dimensions and one periodic dimension may or may not be feasible with the current strategy. The powder patterns of these quasicrystals have two sets of peaks, one periodically spaced and the other quasiperiodically spaced. The relative scalings between these two sets of peaks is unconstrained, so such a program will have to fit two superimposed sets of peaks independently without knowing *a priori* which peaks belong to which set. With the introduction of broadening and small shifts in position due to defects or phason strain, it is unclear if the current method of searching the powder patterns can be successful in these cases. Other two-dimensional quasicrystals, such as octagonal or dodecagonal, should be investigated, though the search for those phases, too, will likely encounter difficulties similar to those in the decagonal case.

A natural extension of the present experimental study would be to investigate the silver-gold-telluride system fully by laboratory synthesis. Two of the natural minerals in this class, calaverite and now probably krennerite, are incommensurate crystals, and sylvanite may be. Determining the full reciprocal lattice and the basis vectors for krennerite is an obvious next step. Then it is conceivable that, by synthesizing

different stoichiometries in the laboratory, a quasicrystal region in the phase diagram may be found. Furthermore, since tellurium has been postulated to be responsible for incommensurability in calaverite by modulating the valences around gold atoms,[49] studies of other tellurium compounds may be worthwhile. Several tellurides, notably volynskite, are among top candidates fingered by our search programs (and keithconnite,  $Pd_{3-x}Te$  ( $x = 0.14 - 0.43$ ))[9] and kurilite  $AgTe$  were in lists generated by variants of this program).

In sum, our investigation to date suggests that powder diffracton data can be used to screen for quasicrystals. As figure 7.1 shows, the known quasicrystals have been successfully separated from the bulk of known minerals and synthetic materials. What is unclear at this stage is whether the small set of minerals and synthetic materials separated along with the quasicrystals include any previously unknown quasicrystals. Less than a handful of samples have been gathered and tested experimentally. However, the fact that a previously unknown incommensurate crystal has been uncovered by the investigation is noteworthy in itself, and suggests that other new quasiperiodic and perhaps quasicrystalline solids may be found as the investigation continues in the coming months.

## Appendix A

---

### Published Quasicrystal Indexings

Data are presented from the published papers and our computer results of the  $(N, M)$  indexing, following Janot's convention[27] and as described in equations (3.18) and (3.19). Although all of the authors presented their data using the six-dimensional icosahedral basis vectors, the set of basis vectors chosen varied among papers; by collapsing to the one-dimensional representation, all results could be compared directly (permutations of the same basis vectors all lead to the same  $(N, M)$  indexing). On several occasions, the authors of the papers did not explicitly define their basis vectors, and while some of their indexings could be converted to our notation, others could not be. In those situations, the published peak is marked as an 'X.' Where the published and our calculated peak indexings do not agree, an asterisk is placed in the column marked "Disagree."

**401158 Aluminum Copper Lithium ( $\text{Al}_6\text{CuLi}_3$ ) [34]**

$Q^2_{\parallel \text{real}}$ ( $\text{\AA}^{-2}$ )	$I_{\text{real}}$	Icosahedral	$(N, M)_{\text{calc}}$	$[N, M]_{\text{pub}}$	Disagree
0.02902	20	2 0 -1 -1 -2 0	(20, -12)	[20, -12]	
0.05615	80	1 0 0 -1 -1 0	(6, -3)	[6, -3]	
0.07305	15	1 1 -1 0 -1 0	(8, -4)	[8, -4]	
0.08353	10	2 1 -2 0 -2 0	(26, -15)	[26, -15]	
0.1041	5	3 -1 -1 -1 -1 1	(28, -16)	[28, -16]	
0.1765	35	1 0 0 0 0 0	(2, 1)	[2, 1]	
0.1958	85	1 0 0 0 0 1	(4, 0)	[4, 0]	
0.2518	100	1 1 0 -1 -1 -1	(10, -3)	[10, -3]	
0.2696	25	2 0 0 -1 -1 0	(12, -4)	[12, -4]	
0.3225	5	2 0 0 -1 -2 0	(18, -7)	[18, -7]	
0.3424	5	2 1 -1 0 -2 0	(20, -8)	[20, -8]	
0.3727	15	3 1 -2 -1 -2 1	(40, -20)	[40, -20]	
0.5109	30	1 1 0 0 0 0	(4, 4)	[4, 4]	
0.5176	5	2 1 0 -1 -2 -1	(22, -7)	[56, -28]	*
0.5696	5	2 0 0 0 0 1	(10, 1)	[10, 1]	
0.638	5	2 1 -1 1 -1 1	(18, -3)	[18, -3]	
0.6741	10	3 1 -1 -2 -2 0	(38, -15)	[6, 5]	*
0.7062	10	2 0 0 0 0 0	(8, 4)	[8, 4]	
0.9002	15	2 1 0 0 -1 0	(12, 4)	[12, 4]	

**401285 Aluminum Copper Lithium ( $\text{Al}_{56.1}\text{Cu}_{10.2}\text{Li}_{33.7}$ ) [37]**

$Q^2_{\parallel \text{real}}$ ( $\text{\AA}^{-2}$ )	$I_{\text{real}}$	Icosahedral	$(N, M)_{\text{calc}}$	$[N, M]_{\text{pub}}$	Disagree
0.009831	2	2 -1 -1 -1 -1 1	(18, -11)	[18, -11]	
0.02846	13	2 0 -1 -1 -2 0	(20, -12)	[20, -12]	
0.05586	73	1 0 0 -1 -1 0	(6, -3)	[6, -3]	
0.0745	10	1 1 -1 0 -1 0	(8, -4)	[8, -4]	
0.08437	15	2 1 -2 0 -2 0	(26, -15)	[26, -15]	
0.1304	4	2 0 -1 0 -1 1	(14, -7)	[14, -7]	
0.1764	20	1 0 0 0 0 0	(2, 1)	[2, 1]	
0.1951	99	1 0 0 0 0 1	(4, 0)	[4, 0]	
0.251	100	1 1 0 -1 -1 -1	(10, -3)	[10, -3]	
0.2695	19	2 0 0 -1 -1 0	(12, -4)	[12, -4]	
0.3256	4	2 0 0 -1 -2 0	(18, -7)	[18, -7]	
0.3442	1	2 1 -1 0 -2 0	(20, -8)	[20, -8]	
0.3716	10	1 1 0 0 -1 0	(6, 1)	[6, 1]	
0.39	2	1 1 0 0 -1 -1	(8, 0)	[8, 0]	
0.446	3	2 1 -1 0 -1 0	(14, -3)	[14, -3]	
0.4647	1	2 1 -1 0 -1 1	(16, -4)	[16, -4]	
0.5107	34	1 1 0 0 0 0	(4, 4)	[4, 4]	
0.539	2	3 0 -1 0 -1 1	(24, -8)	[24, -8]	
0.5667	5	2 0 0 0 0 1	(10, 1)	[10, 1]	
0.5853	12	2 0 0 0 -1 1	(12, 0)	[12, 0]	

**410928 Aluminum Copper Lithium ( $\text{Al}_6\text{CuLi}_3$ ) [35]**

$Q^2_{  \text{real}}$ ( $\text{\AA}^{-2}$ )	$I_{\text{real}}$	Icosahedral	$(N, M)_{\text{calc}}$	$[N, M]_{\text{pub}}$	Disagree
0.02883	8	2 0 -1 -1 -2 0	(20, -12)	[20, -12]	
0.05586	57	1 0 0 -1 -1 0	(6, -3)	[6, -3]	
0.07388	15	1 1 -1 0 -1 0	(8, -4)	[8, -4]	
0.08392	10	2 1 -2 0 -2 0	(26, -15)	[26, -15]	
0.1761	45	1 0 0 0 0 0	(2, 1)	[2, 1]	
0.1954	100	1 0 0 0 0 1	(4, 0)	[4, 0]	
0.2505	78	1 1 0 -1 -1 -1	(10, -3)	[10, -3]	
0.2696	15	2 0 0 -1 -1 0	(12, -4)	[12, -4]	
0.3258	3	2 0 0 -1 -2 0	(18, -7)	[18, -7]	
0.3709	6	1 1 0 0 -1 0	(6, 1)	[6, 1]	
0.5109	22	1 1 0 0 0 0	(4, 4)	[4, 4]	
0.5662	4	2 0 0 0 0 1	(10, 1)	[56, -28]	*
0.5845	6	2 0 0 0 -1 1	(12, 0)	X	
0.7038	8	2 0 0 0 0 0	(8, 4)	X	
0.8817	7	4 0 -1 -1 -2 0	(44, -16)	X	
0.8985	5	2 1 0 0 -1 0	(12, 4)	X	
1.216	5	2 1 0 0 0 1	(12, 8)	X	

**441195 Aluminum Manganese ( $\text{Al}_6\text{Mn}$ ) [25]**

$Q^2_{  \text{real}}$ ( $\text{\AA}^{-2}$ )	$I_{\text{real}}$	Icosahedral	$(N, M)_{\text{calc}}$	$[N, M]_{\text{pub}}$	Disagree
0.06746	22	1 0 0 -1 -1 0	(6, -3)	[6, -3]	
0.08916	8	1 1 -1 0 -1 0	(8, -4)	[8, -4]	
0.1226	2	3 -1 -1 -1 -1 1	(28, -16)	[28, -16]	
0.1571	3	2 0 -1 0 -1 1	(14, -7)	[14, -7]	
0.2124	100	1 0 0 0 0 0	(2, 1)	[2, 1]	
0.2345	78	1 0 0 0 0 1	(4, 0)	[4, 0]	
0.2659	1	2 1 -1 -1 -2 -1	(24, -12)	[24, -12]	
0.3239	2	2 0 0 -1 -1 0	(12, -4)	[12, -4]	
0.3892	1	2 0 0 -1 -2 0	(18, -7)	[18, -7]	
0.4468	11	1 1 0 0 -1 0	(6, 1)	[6, 1]	
0.4699	3	1 1 0 0 -1 -1	(8, 0)	[8, 0]	
0.536	1	2 1 -1 0 -1 0	(14, -3)	[14, -3]	
0.5596	1	2 1 -1 0 -1 1	(16, -4)	[16, -4]	
0.6151	20	1 1 0 0 0 0	(4, 4)	[4, 4]	
0.6307	1	2 1 0 -1 -2 -1	(22, -7)	[56, -28]	*
0.7691	1	2 1 -1 1 -1 1	(18, -3)	[18, -3]	
0.8252	5	1 1 0 1 0 0	(6, 5)	[6, 5]	
0.8491	7	2 0 0 0 0 0	(8, 4)	[8, 4]	
0.861	3	2 2 -1 0 -2 0	(26, -7)	[26, -7]	
0.9303	1	2 1 0 -1 -1 -1	(16, 0)	[16, 0]	
1.08	1	2 1 0 0 -1 0	(12, 4)	[12, 4]	

**441209 Aluminum Copper Lithium ( $\text{Al}_6\text{CuLi}_3$ ) [39]**

$Q_{\parallel \text{real}}^2 (\text{\AA}^{-2})$	$I_{\text{real}}$	Icosahedral	$(N, M)_{\text{calc}}$	$[N, M]_{\text{pub}}$	Disagree
0.02895	30	2 0 -1 -1 -2 0	(20, -12)	[20, -12]	
0.05616	100	1 0 0 -1 -1 0	(6, -3)	[6, -3]	
0.07424	30	1 1 -1 0 -1 0	(8, -4)	[8, -4]	
0.08289	20	2 1 -2 0 -2 0	(26, -15)	X	
0.1311	20	2 0 -1 0 -1 1	(14, -7)	[14, -7]	
0.1764	100	1 0 0 0 0 0	(2, 1)	[2, 1]	
0.1963	100	1 0 0 0 0 1	(4, 0)	X	
0.2047	20	2 1 -1 -1 -2 0	(22, -11)	X	
0.2222	20	2 1 -1 -1 -2 -1	(24, -12)	[24, -12]	
0.2513	30	1 1 0 -1 -1 -1	(10, -3)	X	
0.2687	50	2 0 0 -1 -1 0	(12, -4)	X	
0.3268	20	2 0 0 -1 -2 0	(18, -7)	X	
0.3727	20	3 1 -2 -1 -2 1	(40, -20)	X	
0.4468	20	2 1 -1 0 -1 0	(14, -3)	X	
0.5116	50	1 1 0 0 0 0	(4, 4)	X	
0.5663	20	2 0 0 0 0 1	(10, 1)	X	

**461056 Aluminum Copper Magnesium ( $\text{Al}_6\text{CuMg}_4$ ) [36]**

$Q_{\parallel \text{real}}^2 (\text{\AA}^{-2})$	$I_{\text{real}}$	Icosahedral	$(N, M)_{\text{calc}}$	$[N, M]_{\text{pub}}$	Disagree
0.01006	20	2 -1 -1 -1 -1 1	(18, -11)	[52, -32]	*
0.02815	20	2 0 -1 -1 -2 0	(20, -12)	[20, -12]	
0.05073	20	1 0 0 -1 -1 0	(6, -3)	[6, -3]	
0.06712	10	1 1 -1 0 -1 0	(8, -4)	[6, -3]	*
0.1639	80	1 0 0 0 0 0	(2, 1)	[2, 1]	
0.1811	100	1 0 0 0 0 1	(4, 0)	[4, 0]	
0.2334	50	1 1 0 -1 -1 -1	(10, -3)	[10, -3]	
0.3019	10	2 0 0 -1 -2 0	(18, -7)	[18, -7]	
0.4756	80	1 1 0 0 0 0	(4, 4)	[4, 4]	
0.5569	10	3 0 -1 0 -1 2	(30, -11)	[10, 1]	*
0.5917	10	2 1 -1 1 -1 1	(18, -3)	[18, -3]	
0.6504	50	2 0 0 0 0 0	(8, 4)	[8, 4]	
0.7305	50	3 1 -1 -1 -2 1	(34, -11)	[16, 0]	*
0.8264	10	4 0 -1 -1 -2 0	(44, -16)	[96, -48]	*
0.89	10	2 1 0 0 -2 0	(18, 1)	[14, 5]	*
0.9612	10	3 1 -1 0 -1 1	(26, -3)	[12, 16]	*
1.132	50	2 1 0 0 0 1	(12, 8)	[12, 8]	
1.235	10	1 1 1 1 0 0	(8, 12)	[8, 12]	
1.417	10	2 1 0 1 0 0	(12, 12)	[12, 12]	
1.452	20	3 1 0 -1 -2 1	(32, 0)	[18, 9]	*
1.731	10	3 2 -1 0 -1 0	(30, 5)	[12, 16]	*
1.778	10	2 2 0 1 -1 0	(20, 12)	[26, 9]	*
1.877	10	2 1 1 0 0 1	(14, 17)	[16, 16]	*
2.1	10	4 0 0 0 0 2	(40, 4)	[20, 16]	*
2.367	10	2 2 1 0 -1 0	(20, 20)	[38, 9]	*

**461059 Aluminum Manganese ( $\text{Al}_{86}\text{Mn}_{14}$ ) [25]**

$Q_{\parallel\text{real}}^2 (\text{\AA}^{-2})$	$I_{\text{real}}$	Icosahedral	$(N, M)_{\text{calc}}$	$[N, M]_{\text{pub}}$	Disagree
0.06746	22	1 0 0 -1 -1 0	(6, -3)	[6, -3]	
0.08916	8	1 1 -1 0 -1 0	(8, -4)	[8, -4]	
0.1223	2	3 -1 -1 -1 -1 1	(28, -16)	[28, -16]	
0.1575	3	2 0 -1 0 -1 1	(14, -7)	[14, -7]	
0.2124	100	1 0 0 0 0 0	(2, 1)	[2, 1]	
0.2345	78	1 0 0 0 0 1	(4, 0)	[4, 0]	
0.2657	1	2 1 -1 -1 -2 -1	(24, -12)	[24, -12]	
0.3228	2	2 0 0 -1 -1 0	(12, -4)	[12, -4]	
0.3906	1	2 0 0 -1 -2 0	(18, -7)	[18, -7]	
0.4468	11	1 1 0 0 -1 0	(6, 1)	[6, 1]	
0.4698	3	1 1 0 0 -1 -1	(8, 0)	[8, 0]	
0.5328	1	2 1 -1 0 -1 0	(14, -3)	[14, -3]	
0.5569	1	2 1 -1 0 -1 1	(16, -4)	[16, -4]	
0.6151	20	1 1 0 0 0 0	(4, 4)	[4, 4]	
0.6299	1	2 1 0 -1 -2 -1	(22, -7)	[56, -28]	*
0.7695	1	2 1 -1 1 -1 1	(18, -3)	[18, -3]	
0.8249	5	1 1 0 1 0 0	(6, 5)	[6, 5]	
0.8417	7	2 0 0 0 0 0	(8, 4)	[8, 4]	
0.8573	3	2 2 -1 0 -2 0	(26, -7)	[26, -7]	
0.9299	1	2 1 0 -1 -1 -1	(16, 0)	[16, 0]	
1.081	1	2 1 0 0 -1 0	(12, 4)	[12, 4]	



## Appendix B

---

### Top Ten Mineral Candidates

The full indexing data is given for the top ten mineral candidates. Each mineral entry has title information, a table of peaks with indexings, and summary statistics. The title information includes a mineral's PDF number, name, chemical formula and weighting factor used, either intensity ( $I$ ) or its square root ( $\sqrt{I}$ ). Each table contains the following data

$Q_{\parallel \text{real}}^2$  Real value of  $|\vec{Q}_{\parallel}|^2 = 1/d^2$  from the Powder Diffraction File data.

$(Q_{\parallel \text{calc}}^2)$  Calculated value of  $|\vec{Q}_{\parallel}|^2$  based on the closest-matching ideal peak.

$\Delta\%$  Percentage difference in  $|\vec{Q}_{\parallel}|^2$  between real and ideal peaks.

$I_{\text{real}}$  Real intensity from the Powder Diffraction File.

$I_{\text{calc}}$  Calculated intensity based on the  $I \approx \text{sinc}^2 Q_{\perp}$  for the closest-matching ideal peak.

$Q_{\perp}$   $|\vec{Q}_{\perp}|$  for the closest-matching ideal peak.

$n_i$  Six icosahedral indices as defined by [27] and used in equation 3.16.

$N$  One dimensional indexing vector of [27] defined in equation 3.18.

$M$  One dimensional indexing vector of [27] defined in equation 3.19.

**Pair** Indicates whether peak is a member of a  $(2, -1)$  pair. If it has the lower  $Q_{\parallel}$  of the two, it is marked with a ‘\’; if it has the higher, ‘/’.

The summary statistics listed for each pattern are the same as those in table 4.3: averages for  $N$ ,  $\Delta\%$  and  $Q_{\perp}$  as defined above weighted by the factor listed in the mineral title information, as well as the number of peaks in a  $(\Delta N, \Delta M) = (2, -1)$  pair and percentage of real data peaks involved in a  $(2, -1)$  pair. The *Doubles* entry lists the number of “double matches,” in which a single calculated peak matches to more than one real data peak.

**140117 Theophrastite, Ni(OH)<sub>2</sub> (*I*)**

$Q_{\parallel \text{real}}^2$	$(Q_{\parallel \text{calc}}^2)$	$\Delta\%$	$I_{\text{real}}$	$I_{\text{calc}}$	$Q_{\perp}$	$n_i$	$N$	$M$	Pair
0.04716	0.04716	0.0006881%	100	73	1.902	1 0 0 0 0 0	2	1	
0.1365	0.1365	0.006971%	45	71	2	1 1 0 0 0 0	4	4	
0.1836	0.1836	0.01895%	100	51	2.76	1 1 0 1 0 0	6	5	\
0.1887	0.1886	0.02252%	2	25	3.804	2 0 0 0 0 0	8	4	/
0.325	0.3251	0.0108%	35	15	4.298	2 1 0 0 0 1	12	8	
0.4093	0.4095	0.01579%	25	32	3.464	2 1 0 1 0 0	12	12	
0.4244	0.4244	0.0007349%	1	0.99	5.706	3 0 0 0 0 0	18	9	
0.4565	0.4566	0.008411%	16	22	3.952	2 1 1 0 -1 0	14	13	
0.5455	0.546	0.04554%	4	21	4	2 2 0 0 0 0	16	16	
0.5611	0.5609	0.01859%	8	0.15	6.047	3 1 0 0 0 1	22	13	
0.5926	0.5931	0.0407%	10	13	4.429	2 2 0 1 0 0	18	17	\
0.5981	0.5981	0.003645%	2	4.4	5.145	3 1 0 0 0 0	20	16	/
0.7343	0.7346	0.02042%	8	1.8	5.52	3 1 1 0 -1 0	24	20	

Weighted Avg N: 7.33

Weighted Avg  $\Delta\%$ : 0.00877%Weighted Avg  $Q_{\perp}$ : 2.9

(+2, -1) Pairs: 1 = 15.4%

Doubles: 0

**140117 Theophrastite, Ni(OH)<sub>2</sub> ( $\sqrt{I}$ )**

$Q_{\parallel \text{real}}^2$	$(Q_{\parallel \text{calc}}^2)$	$\Delta\%$	$I_{\text{real}}$	$I_{\text{calc}}$	$Q_{\perp}$	$n_i$	$N$	$M$	Pair
0.04716	0.04716	0.0006881%	100	73	1.902	1 0 0 0 0 0	2	1	
0.1365	0.1365	0.006971%	45	71	2	1 1 0 0 0 0	4	4	
0.1836	0.1836	0.01895%	100	51	2.76	1 1 0 1 0 0	6	5	\
0.1887	0.1886	0.02252%	2	25	3.804	2 0 0 0 0 0	8	4	/
0.325	0.3251	0.0108%	35	15	4.298	2 1 0 0 0 1	12	8	
0.4093	0.4095	0.01579%	25	32	3.464	2 1 0 1 0 0	12	12	
0.4244	0.4244	0.0007349%	1	0.99	5.706	3 0 0 0 0 0	18	9	
0.4565	0.4566	0.008411%	16	22	3.952	2 1 1 0 -1 0	14	13	
0.5455	0.546	0.04554%	4	21	4	2 2 0 0 0 0	16	16	
0.5611	0.5609	0.01859%	8	0.15	6.047	3 1 0 0 0 1	22	13	
0.5926	0.5931	0.0407%	10	13	4.429	2 2 0 1 0 0	18	17	\
0.5981	0.5981	0.003645%	2	4.4	5.145	3 1 0 0 0 0	20	16	/
0.7343	0.7346	0.02042%	8	1.8	5.52	3 1 1 0 -1 0	24	20	

Weighted Avg N: 10.1

Weighted Avg  $\Delta\%$ : 0.0129%Weighted Avg  $Q_{\perp}$ : 3.41

(+2, -1) Pairs: 1 = 15.4%

Doubles: 0

**020612 Krennerite, (Ag,Au)Te<sub>2</sub> ( $\sqrt{I}$ )**

$Q_{\parallel \text{real}}^2$	$(Q_{\parallel \text{calc}}^2)$	$\Delta\%$	$I_{\text{real}}$	$I_{\text{calc}}$	$Q_{\perp}$	$n_i$	$N$	$M$	Pair
0.1075	0.1075	0.0006881%	100	73	1.902	1 0 0 0 0 0	2	1	\
0.1149	0.1188	1.699%	80	38	3.236	1 0 0 0 0 1	4	0	/
0.1993	0.1983	0.2559%	50	2.7	7.645	2 0 0 -1 -2 0	18	-7	
0.2225	0.2263	0.8577%	90	26	3.754	1 1 0 0 -1 0	6	1	\
0.2334	0.2377	0.9194%	30	11	4.576	1 1 0 0 -1 -1	8	0	/
0.2551	0.255	0.011%	20	4.3	9.629	2 1 0 -2 -2 -1	28	-12	
0.3121	0.3111	0.1552%	50	71	2	1 1 0 0 0 0	4	4	
0.346	0.3452	0.1206%	50	6.2	4.956	2 0 0 0 0 1	10	1	
0.4328	0.43	0.3285%	50	25	3.804	2 0 0 0 0 0	8	4	
0.4565	0.464	0.8164%	30	0.37	5.919	2 1 0 -1 -1 0	14	1	
0.5487	0.5488	0.01241%	30	5.8	4.994	2 1 0 0 -1 0	12	4	
0.5739	0.5662	0.6788%	30	4	9.835	3 1 -1 0 -2 1	32	-8	
0.62	0.6223	0.1824%	20	49	2.828	1 1 1 0 0 -1	8	8	
0.683	0.685	0.1464%	30	3	10.35	3 1 0 -2 -2 0	36	-8	

Weighted Avg N: 12

Weighted Avg  $\Delta\%$ : 0.347%Weighted Avg  $Q_{\perp}$ : 5

(+, -) Pairs: 2 = 28.6%

Doubles: 0

**181173 Volynskite, AgBiTe<sub>2</sub> ( $I$ )**

$Q_{\parallel \text{real}}^2$	$(Q_{\parallel \text{calc}}^2)$	$\Delta\%$	$I_{\text{real}}$	$I_{\text{calc}}$	$Q_{\perp}$	$n_i$	$N$	$M$	Pair
0.06999	0.07739	5.158%	10	0.83	6.927	2 0 -1 0 -1 1	14	-7	
0.07716	0.07739	0.1503%	5	0.83	6.927	2 0 -1 0 -1 1	14	-7	\
0.08858	0.08845	0.07224%	5	2.1	7.405	2 0 -1 -1 -1 1	16	-8	/
0.1047	0.1047	0.0006881%	100	73	1.902	1 0 0 0 0 0	2	1	
0.1249	0.1216	1.308%	10	4.6	8.683	2 1 -1 -1 -2 0	22	-11	
0.2047	0.2042	0.1246%	35	3.8	8.081	2 1 -1 0 -2 0	20	-8	
0.2163	0.2205	0.9609%	30	26	3.754	1 1 0 0 -1 0	6	1	
0.2551	0.2485	1.305%	10	4.3	9.629	2 1 0 -2 -2 -1	28	-12	
0.3019	0.3031	0.204%	20	71	2	1 1 0 0 0 0	4	4	
0.3341	0.3363	0.3263%	10	6.2	4.956	2 0 0 0 0 1	10	1	
0.4162	0.4189	0.323%	20	25	3.804	2 0 0 0 0 0	8	4	
0.4756	0.48	0.4622%	10	2.3	10.66	3 0 0 -2 -2 1	36	-12	
0.4959	0.4963	0.03862%	5	3.4	7.903	3 0 0 -1 -1 0	22	-3	
0.5328	0.5347	0.1803%	10	5.8	4.994	2 1 0 0 -1 0	12	4	
0.5917	0.5952	0.2947%	10	91	1.07	1 1 1 0 0 0	6	9	
0.62	0.6232	0.2556%	10	4.7	8.932	3 1 -1 -1 -1 1	28	-4	
0.661	0.6563	0.3532%	10	3.6	10.02	2 2 0 -1 -2 -2	34	-7	

Weighted Avg N: 11.2

Weighted Avg  $\Delta\%$ : 0.3%Weighted Avg  $Q_{\perp}$ : 4.75

(+, -) Pairs: 1 = 11.8%

Doubles: 1

**461355 Miargyrite, selenian, AgSb(S,Se)<sub>2</sub> (I)**

$Q_{\parallel \text{real}}^2$	$(Q_{\parallel \text{calc}}^2)$	$\Delta\%$	$I_{\text{real}}$	$I_{\text{calc}}$	$Q_{\perp}$	$n_i$	$N$	$M$	Pair
0.02342	0.02616	5.706%	1	11	4.535	1 0 0 -1 -1 0	6	-3	
0.08262	0.08262	0.0006881%	59	73	1.902	1 0 0 0 0 0	2	1	
0.09651	0.09594	0.2942%	20	4.6	8.683	2 1 -1 -1 -2 0	22	-11	\
0.1021	0.1047	1.231%	1	4.7	9.069	2 1 -1 -1 -2 -1	24	-12	/
0.1174	0.1175	0.06062%	100	1.6	5.571	1 1 0 -1 -1 -1	10	-3	\
0.1268	0.1262	0.2351%	59	0.043	6.155	2 0 0 -1 -1 0	12	-4	/
0.1958	0.196	0.05536%	1	4.3	9.629	2 1 0 -2 -2 -1	28	-12	
0.2047	0.2089	0.9978%	1	0.061	6.443	2 1 -1 0 -1 0	14	-3	
0.2356	0.2391	0.736%	1	71	2	1 1 0 0 0 0	4	4	
0.2403	0.2391	0.2419%	30	71	2	1 1 0 0 0 0	4	4	
0.2986	0.3002	0.2656%	15	1.5	7.21	2 1 -1 1 -1 1	18	-3	
0.3236	0.3222	0.2045%	2	0.89	11.43	3 1 -1 -2 -2 -1	40	-16	
0.3906	0.3915	0.1159%	3	3.4	7.903	3 0 0 -1 -1 0	22	-3	
0.4351	0.4351	0.002826%	1	4	9.835	3 1 -1 0 -2 1	32	-8	

Weighted Avg N: 9.9

Weighted Avg  $\Delta\%$ : 0.139%Weighted Avg  $Q_{\perp}$ : 4.97 $(+2, -1)$  Pairs: 1 = 14.3%

Doubles: 1

**461355 Miargyrite, selenian, AgSb(S,Se)<sub>2</sub> ( $\sqrt{I}$ )**

$Q_{\parallel \text{real}}^2$	$(Q_{\parallel \text{calc}}^2)$	$\Delta\%$	$I_{\text{real}}$	$I_{\text{calc}}$	$Q_{\perp}$	$n_i$	$N$	$M$	Pair
0.02342	0.02616	5.706%	1	11	4.535	1 0 0 -1 -1 0	6	-3	
0.08262	0.08262	0.0006881%	59	73	1.902	1 0 0 0 0 0	2	1	
0.09651	0.09594	0.2942%	20	4.6	8.683	2 1 -1 -1 -2 0	22	-11	\
0.1021	0.1047	1.231%	1	4.7	9.069	2 1 -1 -1 -2 -1	24	-12	/
0.1174	0.1175	0.06062%	100	1.6	5.571	1 1 0 -1 -1 -1	10	-3	\
0.1268	0.1262	0.2351%	59	0.043	6.155	2 0 0 -1 -1 0	12	-4	/
0.1958	0.196	0.05536%	1	4.3	9.629	2 1 0 -2 -2 -1	28	-12	
0.2047	0.2089	0.9978%	1	0.061	6.443	2 1 -1 0 -1 0	14	-3	
0.2356	0.2391	0.736%	1	71	2	1 1 0 0 0 0	4	4	
0.2403	0.2391	0.2419%	30	71	2	1 1 0 0 0 0	4	4	
0.2986	0.3002	0.2656%	15	1.5	7.21	2 1 -1 1 -1 1	18	-3	
0.3236	0.3222	0.2045%	2	0.89	11.43	3 1 -1 -2 -2 -1	40	-16	
0.3906	0.3915	0.1159%	3	3.4	7.903	3 0 0 -1 -1 0	22	-3	
0.4351	0.4351	0.002826%	1	4	9.835	3 1 -1 0 -2 1	32	-8	

Weighted Avg N: 12.4

Weighted Avg  $\Delta\%$ : 0.203%Weighted Avg  $Q_{\perp}$ : 5.52 $(+2, -1)$  Pairs: 1 = 14.3%

Doubles: 1

**250405 Haxonite,  $(\text{Fe},\text{Ni})_{23}\text{C}_6$  ( $\sqrt{I}$ )**

$Q^2_{\parallel \text{real}}$	$(Q^2_{\parallel \text{calc}})$	$\Delta\%$	$I_{\text{real}}$	$I_{\text{calc}}$	$Q_{\perp}$	$n_i$	$N$	$M$	Pair
0.09951	0.09951	0.0006881%	20	73	1.902	1 0 0 0 0 0	2	1	\
0.1082	0.11	0.8344%	20	38	3.236	1 0 0 0 0 1	4	0	/
0.1446	0.1415	1.058%	30	1.6	5.571	1 1 0 -1 -1 -1	10	-3	
0.1802	0.1836	0.9381%	100	2.7	7.645	2 0 0 -1 -2 0	18	-7	
0.2161	0.22	0.8987%	100	11	4.576	1 1 0 0 -1 -1	8	0	
0.2881	0.288	0.01715%	60	71	2	1 1 0 0 0 0	4	4	
0.3247	0.3195	0.7925%	50	6.2	4.956	2 0 0 0 0 1	10	1	
0.3594	0.3616	0.298%	20	1.5	7.21	2 1 -1 1 -1 1	18	-3	
0.3867	0.3875	0.101%	30	51	2.76	1 1 0 1 0 0	6	5	\
0.3971	0.398	0.1255%	30	25	3.804	2 0 0 0 0 0	8	4	/
0.5757	0.576	0.03314%	30	49	2.828	1 1 1 0 0 -1	8	8	
0.6123	0.6076	0.383%	40	2.9	5.344	2 1 0 0 -1 1	14	5	
0.6483	0.6496	0.1024%	60	2.3	7.482	3 0 0 0 -1 1	22	1	
0.6741	0.6756	0.1113%	50	34	3.409	2 1 0 0 0 0	10	9	
0.747	0.7442	0.1918%	40	2	10.85	3 2 -1 -1 -2 -1	40	-8	
0.819	0.8121	0.4186%	20	3.6	10.04	3 2 -1 0 -2 0	36	-4	
0.89	0.8956	0.3148%	50	0.99	5.706	3 0 0 0 0 0	18	9	

Weighted Avg N: 13.9

Weighted Avg  $\Delta\%$ : 0.366%Weighted Avg  $Q_{\perp}$ : 5.31

(+2, -1) Pairs: 2 = 23.5%

Doubles: 0

**011281 Covellite, CuS (I)**

$Q^2_{\parallel \text{real}}$	$(Q^2_{\parallel \text{calc}})$	$\Delta\%$	$I_{\text{real}}$	$I_{\text{calc}}$	$Q_{\perp}$	$n_i$	$N$	$M$	Pair
0.04414	0.04085	3.792%	2	0.23	11.98	3 -1 -1 -2 -2 1	40	-24	
0.05005	0.05348	3.367%	2	3.6	5.236	1 1 -1 0 -1 0	8	-4	
0.06345	0.06054	2.32%	4	4.3	9.609	2 1 -2 0 -2 0	26	-15	\
0.07226	0.0739	1.127%	4	3.8	9.96	3 -1 -1 -1 -1 1	28	-16	/
0.09409	0.09358	0.2714%	12	0.83	6.927	2 0 -1 0 -1 1	14	-7	\
0.1089	0.107	0.9074%	20	2.1	7.405	2 0 -1 -1 -1 1	16	-8	/
0.1266	0.1266	0.0006881%	60	73	1.902	1 0 0 0 0 0	2	1	\
0.1362	0.14	1.404%	14	38	3.236	1 0 0 0 0 1	4	0	/
0.2799	0.28	0.01396%	100	11	4.576	1 1 0 0 -1 -1	8	0	
0.3341	0.3335	0.09246%	10	0.9	6.954	2 1 -1 0 -1 1	16	-4	
0.4109	0.4067	0.5178%	30	6.2	4.956	2 0 0 0 0 1	10	1	
0.6104	0.6135	0.2603%	4	4.2	8.325	3 0 0 -1 -1 1	24	-4	
0.683	0.6867	0.2694%	4	0.46	6.746	2 1 0 0 -2 0	18	1	
0.8417	0.8401	0.09603%	8	3.4	7.927	3 1 -1 0 -1 0	24	0	
0.89	0.8936	0.2005%	4	4.4	9.5	3 1 0 -1 -2 -1	32	-4	
0.9803	0.9801	0.009699%	4	4.5	8.562	3 1 -1 1 -1 1	28	0	

Weighted Avg N: 10.1

Weighted Avg  $\Delta\%$ : 0.265%Weighted Avg  $Q_{\perp}$ : 4.88

(+2, -1) Pairs: 3 = 37.5%

Doubles: 0

**360387 Cabriite, Pd<sub>2</sub>SnCu ( $\sqrt{I}$ )**

$Q_{\parallel \text{real}}^2$	$(Q_{\parallel \text{calc}}^2)$	$\Delta\%$	$I_{\text{real}}$	$I_{\text{calc}}$	$Q_{\perp}$	$n_i$	$N$	$M$	Pair
0.1924	0.1924	0.0006881%	80	73	1.902	1 0 0 0 0 0	2	1	\
0.2085	0.2127	0.9957%	100	38	3.236	1 0 0 0 0 1	4	0	/
0.259	0.2736	2.781%	10	1.6	5.571	1 1 0 -1 -1 -1	10	-3	
0.2718	0.2736	0.3223%	10	1.6	5.571	1 1 0 -1 -1 -1	10	-3	\
0.296	0.2939	0.3573%	20	0.043	6.155	2 0 0 -1 -1 0	12	-4	/
0.3825	0.3859	0.4431%	20	0.92	11.41	3 1 -2 0 -2 1	38	-19	
0.4559	0.4564	0.04775%	10	4.3	9.629	2 1 0 -2 -2 -1	28	-12	
0.4856	0.4863	0.06707%	10	0.061	6.443	2 1 -1 0 -1 0	14	-3	
0.5124	0.5173	0.4774%	10	2.4	10.64	3 0 0 -2 -2 0	34	-15	
0.5528	0.5568	0.3598%	10	71	2	1 1 0 0 0 0	4	4	
0.6009	0.5985	0.2014%	20	0.34	11.86	4 -1 -1 -1 -1 1	42	-19	
0.6578	0.6487	0.6906%	50	4	9.815	3 0 -1 0 -1 2	30	-11	\
0.6741	0.669	0.3737%	10	3.4	10.16	3 1 -1 -1 -2 0	32	-12	/
0.7133	0.7193	0.4136%	10	2.8	7.67	2 1 0 -1 -2 0	20	-4	
0.7735	0.7695	0.2638%	10	25	3.804	2 0 0 0 0 0	8	4	
0.8417	0.8507	0.5346%	20	0.085	6.472	2 1 0 -1 -1 -1	16	0	
0.8686	0.8614	0.4124%	10	3	10.33	3 1 -1 -1 -2 1	34	-11	
0.9335	0.9319	0.085%	10	4.2	8.325	3 0 0 -1 -1 1	24	-4	
0.9784	0.9821	0.1928%	10	5.8	4.994	2 1 0 0 -1 0	12	4	

Weighted Avg N: 18.1

Weighted Avg  $\Delta\%$ : 0.419%Weighted Avg  $Q_{\perp}$ : 6.7

(+2, -1) Pairs: 3 = 31.6%

Doubles: 1

**020318 Sulfohalite, 2Na<sub>2</sub>SO<sub>4</sub>ClF ( $\sqrt{I}$ )**

$Q_{\parallel \text{real}}^2$	$(Q_{\parallel \text{calc}}^2)$	$\Delta\%$	$I_{\text{real}}$	$I_{\text{calc}}$	$Q_{\perp}$	$n_i$	$N$	$M$	Pair
0.06925	0.06925	0.0006881%	100	73	1.902	1 0 0 0 0 0	2	1	
0.08117	0.08042	0.4646%	50	4.6	8.683	2 1 -1 -1 -2 0	22	-11	
0.1446	0.1458	0.4259%	90	26	3.754	1 1 0 0 -1 0	6	1	\
0.1514	0.1531	0.5666%	100	11	4.576	1 1 0 0 -1 -1	8	0	/
0.2204	0.2224	0.4437%	30	6.2	4.956	2 0 0 0 0 1	10	1	\
0.2268	0.2297	0.6445%	30	1.4	5.605	2 0 0 0 -1 1	12	0	/
0.2685	0.2697	0.2271%	40	51	2.76	1 1 0 1 0 0	6	5	
0.2799	0.2809	0.1634%	40	4.7	8.91	2 2 -1 0 -2 0	26	-7	
0.3228	0.3282	0.8245%	30	3.4	7.903	3 0 0 -1 -1 0	22	-3	
0.4504	0.4521	0.1809%	20	2.3	7.482	3 0 0 0 -1 1	22	1	
0.4628	0.4632	0.05033%	20	1.1	11.3	3 1 0 -1 -3 -1	42	-11	
0.5739	0.5759	0.1757%	10	1.1	7.036	2 2 0 -1 -1 -1	22	5	

Weighted Avg N: 14.3

Weighted Avg  $\Delta\%$ : 0.323%Weighted Avg  $Q_{\perp}$ : 5.7

(+2, -1) Pairs: 2 = 33.3%

Doubles: 0

**021145 Allargentum, Ag-Sb ( $\sqrt{I}$ )**

$Q_{\parallel \text{real}}^2$	$(Q_{\parallel \text{calc}}^2)$	$\Delta\%$	$I_{\text{real}}$	$I_{\text{calc}}$	$Q_{\perp}$	$n_i$	$N$	$M$	Pair
0.1562	0.1473	2.909%	60	0.83	6.927	2 0 -1 0 -1 1	14	-7	
0.1765	0.1794	0.8141%	60	1.8	10.94	3 -1 -1 -1 -1 2	34	-19	
0.1993	0.1993	0.0006881%	100	73	1.902	1 0 0 0 0 0	2	1	
0.3303	0.3366	0.9555%	40	2.7	10.47	3 0 -1 -1 -2 1	32	-16	
0.4691	0.4728	0.3902%	80	4.3	9.629	2 1 0 -2 -2 -1	28	-12	
0.5487	0.557	0.7508%	80	1.7	10.96	3 1 -2 0 -2 0	36	-16	
0.64	0.64	0.002659%	60	6.2	4.956	2 0 0 0 0 1	10	1	\
0.661	0.661	0.002473%	60	1.4	5.605	2 0 0 0 -1 1	12	0	/
0.6944	0.6931	0.09334%	20	3.4	10.16	3 1 -1 -1 -2 0	32	-12	
0.7972	0.7972	0.0008132%	20	25	3.804	2 0 0 0 0 0	8	4	
0.8573	0.8603	0.1716%	20	0.37	5.919	2 1 0 -1 -1 0	14	1	
1.02	1.018	0.1363%	40	5.8	4.994	2 1 0 0 -1 0	12	4	
1.132	1.133	0.03987%	40	91	1.07	1 1 1 0 0 0	6	9	\
1.156	1.154	0.1099%	40	49	2.828	1 1 1 0 0 -1	8	8	/

Weighted Avg N: 17.9

Weighted Avg  $\Delta\%$ : 0.285%Weighted Avg  $Q_{\perp}$ : 6.5

(+2, -1) Pairs: 2 = 28.6%

Doubles: 0

**021293 Nicolite, NiAs ( $\sqrt{I}$ )**

$Q_{\parallel \text{real}}^2$	$(Q_{\parallel \text{calc}}^2)$	$\Delta\%$	$I_{\text{real}}$	$I_{\text{calc}}$	$Q_{\perp}$	$n_i$	$N$	$M$	Pair
0.1034	0.1034	0.0006881%	20	73	1.902	1 0 0 0 0 0	2	1	
0.1173	0.1201	1.176%	20	4.6	8.683	2 1 -1 -1 -2 0	22	-11	
0.1457	0.147	0.4672%	80	1.6	5.571	1 1 0 -1 -1 -1	10	-3	
0.2143	0.2177	0.7779%	20	26	3.754	1 1 0 0 -1 0	6	1	
0.263	0.2614	0.3108%	100	0.061	6.443	2 1 -1 0 -1 0	14	-3	
0.3086	0.305	0.5913%	80	4.2	8.302	2 1 0 -1 -2 -1	22	-7	
0.4444	0.4463	0.2075%	60	0.37	5.919	2 1 0 -1 -1 0	14	1	\
0.4565	0.4572	0.07474%	60	0.085	6.472	2 1 0 -1 -1 -1	16	0	/
0.5653	0.5606	0.4182%	70	0.46	6.746	2 1 0 0 -2 0	18	1	
0.6299	0.6313	0.1086%	40	2.9	5.344	2 1 0 0 -1 1	14	5	
0.7182	0.7186	0.02596%	30	4.7	9.132	3 1 0 -1 -2 0	30	-3	
0.7432	0.7455	0.1601%	70	0.003	6.248	2 1 1 -1 -1 -1	18	5	\
0.7561	0.7565	0.02176%	70	0.52	6.774	3 0 0 0 0 1	20	4	/
0.8573	0.8598	0.1463%	70	1.1	7.036	2 2 0 -1 -1 -1	22	5	
0.907	0.9035	0.1949%	40	4.7	8.771	3 1 0 -2 -1 0	30	1	
0.9246	0.9305	0.3208%	60	0.99	5.706	3 0 0 0 0 0	18	9	

Weighted Avg N: 17.5

Weighted Avg  $\Delta\%$ : 0.271%Weighted Avg  $Q_{\perp}$ : 6.51

(+2, -1) Pairs: 2 = 25%

Doubles: 0

## Appendix C

---

### Top Fifty Overall Candidates

Top fifty candidates for quasicrystallinity, both natural and synthetic, extracted from the 70,000 patterns of the Powder Diffraction File are listed in the table on the next page. Each table entry has the following headings:

**PDF No.** Six digit number from the Powder Diffraction File.

**Formula** Compound formula.

**N** the weighted average length of the scattering vector  $|\vec{Q}|$

**% Dev.** the weighted average of deviations between real and calculated values of  $|\vec{Q}_{\parallel}|$ .

**Q<sub>⊥</sub>** the weighted average of  $|\vec{Q}_{\perp}|$ .

**Pair %** percentage of real data peaks involved in a (2, -1) pair.

**QC?** If the compound is a known quasicrystal, this column is marked with an asterisk.

The table includes the 50 patterns that met the following criteria. Averages were weighted by intensity  $I$  alone.

Weighted average  $N \leq 12$ .

Weighted average %Dev  $\leq 0.3$ .

Weighted average  $Q_{\perp} \leq 5$ .

Pair %  $\geq 25\%$ .

PDF No.	Formula	<i>N</i>	% Dev.	<i>Q</i> <sub>⊥</sub>	Pair %	QC?
010734	Isatin	10.11	0.2889	4.965	30.77	
010767	Boron Hydrogen Oxide	9.318	0.1914	4.276	57.14	
011281	Copper Sulfide	10.06	0.2654	4.877	37.5	
050553	5-Bromotetrazole	9.022	0.1948	4.017	31.58	
080455	Barium Molybdenum Oxide	10.68	0.1517	4.369	25.64	
100080	Lithium Chromium Fluoride	11.75	0.2851	4.934	33.33	
180118	Ammonium Molybdenum Oxide	11.49	0.1247	4.706	28.57	
190734	Lithium Vanadium Oxide	11.75	0.1649	4.807	33.33	
211242	Sodium Azide	9.376	0.2314	4.297	25	
230153	Cesium Gallium Selenate Hydrate	10.52	0.1634	4.805	28.57	
231077	Thallium Fluoride	9.41	0.1802	4.268	37.5	
241164	Zirconium Oxide	11.26	0.1838	4.822	28.57	
241702	Copper chloride 2(1H)-tetrahydropyrimidinone	10.1	0.2167	4.675	35.29	
260174	Barium Ruthenium Oxide	9.88	0.2616	4.477	36.36	
260527	Copper Iron Germanium Sulfide	9.948	0.1193	4.259	33.33	
261475	Potassium Copper Strontium Nitrite	11.44	0.2037	4.796	26.67	
280034	Aluminum Silver	9.463	0.2498	4.336	37.04	
281395	Niobium Tin Carbide	7.06	0.2704	3.802	30.77	
281930	m-Toluic acid	10.78	0.1504	4.64	25	
290193	Barium Molybdenum Oxide	10.5	0.1538	4.331	25.64	
290653	Hafnium Lead Carbide	8.91	0.2419	4.243	26.67	
290795	Lithium Ammonium Sulfate	11.78	0.07548	4.45	28.57	
310647	Iron Phosphate	10.11	0.2024	4.467	33.33	
311382	Thallium Fluoride	10.69	0.1119	4.575	31.37	
320238	Cesium Indium Arsenate	7.579	0.246	3.795	40	
321665	1,4-Diphenyl-1,3-butadiene	6.867	0.1135	3.34	25.81	
321768	1-Methylthiolanium iodide	11.18	0.2954	4.931	33.33	
330630	Indium Phosphorus Sulfide	11.08	0.1123	4.539	26.09	
331014	Potassium Chromium Hydrogen Phosphate	7.071	0.2684	3.723	40	
341278	Aluminum Nickel Tantalum	9.259	0.2498	4.252	33.33	
351460	Aluminum Nickel Tantalum	9.063	0.2449	4.19	33.33	
351491	Bismuth Molybdenum Oxide	11.54	0.1577	4.924	30.3	
351530	2-(N-Carbamoylmethylamino) ethanesulfonic acid	7.696	0.1168	3.527	33.33	
371135	Germanium Niobium	10.06	0.185	4.68	28.57	
371709	4,4'-Dichlorobiphenyl	9.931	0.2845	4.73	30.77	
381007	Lead Bismuth Oxide Iodide	9.529	0.221	4.309	31.58	
381024	Thallium Antimony Sulfide	7.027	0.1841	3.542	28.57	
390691	Ammonium Cyanide	8.986	0.2374	4.308	40	
391271	Cobalt Europium Germanium	8.592	0.2595	4.26	31.58	
400903	Aluminum Magnesium	5.898	0.2012	3.437	50	
401285	Aluminum Copper Lithium	8.224	0.008655	4.669	80	*
401320	Barium Tritide	11.59	0.1769	4.802	26.09	
401321	Sodium Boron Fluoride	8.714	0.1908	3.917	30.77	
410928	Aluminum Copper Lithium	7.904	0.08229	4.416	47.06	*
421261	Hydrogen Tungsten Oxide	8.406	0.1392	4.277	46.15	
430558	Barium Titanium Oxide	11.86	0.2312	4.923	30	
431154	Aluminum Titanium Vanadium	6.764	0.2155	3.722	28.57	*
431159	Aluminum Titanium Vanadium	6.162	0.1824	3.507	30.77	*
440539	Ammonium Zinc Fluoride Phosphate	9.475	0.2102	4.72	25	
441195	Aluminum Manganese	4.794	0.05882	3.149	47.62	*
451317	Aluminum Palladium Rhenium	9.235	0.2078	4.099	28.57	*
451318	Aluminum Manganese Palladium	6.43	0.1478	3.863	57.14	*
461059	Aluminum Manganese	4.794	0.08463	3.149	47.62	*

# Bibliography

[1] H. Weyl. *Symmetry*. Princeton (1952).

## History of Crystallography

[2] M. A. Bravais. *On the Systems Formed by Points Regularly Distributed on a Plane or in Space*. Trans. by A. J. Shaler. Cryst. Soc. Amer. (1949).

[3] Pliny. *Natural History*. Vol. X. Trans. by D. E. Eichholz. Harvard (1962).

[4] Pliny. *Natural History*. Vol. VI. Trans. by J. Bostock and H. T. Riley. London: Bohm (1857).

[5] M. Senechal. “Brief history of geometrical crystallography” in *Historical Atlas of Crystallography*. J. Lima-de-Faria, ed. Int’l Union of Cryst. (1990).

[6] N. Steno. *The Prodromus*. Trans. by J. Winter. Hafner (1968).

[7] Theophrastus. *De Lapidibus*. Trans. by D. E. Eichholz. Oxford (1965).

[8] A. E. H. Tutton. *The Natural History of Crystals* Dutton (1924).

## Mathematical Crystallography, Diffraction and Scattering

[9] J. W. Anthony, R. A. Bideaux, K. W. Bladh, M. C. Nichols. *Handbook of Mineralogy*. Mineral Data Publishing (1990).

[10] N.W. Ashcroft and N.D. Mermin. *Solid State Physics* Saunders (1976).

- [11] F.D. Bloss. *Crystallography and Crystal Chemistry*. MSA, 1994.
- [12] M. Born and E. Wolf. *Principles of Optics*. 6th ed. Cambridge (1980).
- [13] B. H. Bransden and C. J. Joachain. *Introduction to quantum mechanics*. Longman (1989).
- [14] P. M. Chaikin and T. C. Lubensky. *Principles of condensed matter physics*. Cambridge (1995).
- [15] J.M. Cowley. *Diffraction Physics*. North-Holland (1984).
- [16] R. Feynman, R. Leighton and M. Sands. *The Feynman Lectures on Physics*. Vol. 1. Addison-Wesley (1963).
- [17] S. Gasiorowicz. *Quantum Physics*. 2nd Ed. Wiley (1996).
- [18] J. Goodman. *Introduction to Fourier Optics*. 2nd Ed. McGraw-Hill (1996).
- [19] A. Hellemans and B. Bunch. *The Timetables of Science*. Simon and Schuster (1988).
- [20] C. Huygens *Traite de la Lumiere*. Leyden (1690), Eng. transl. *Treatise on Light* by S. P. Thompson. London (1912), as quoted in M. Born and E. Wolf. *Principles of Optics*. 6th ed. Cambridge (1980).
- [21] J.F. James. *A student's guide to Fourier transforms*. Cambridge (1995).
- [22] L.D. Landau and E.M. Lifshitz *Statistical Physics, Part 1*, 3rd ed. (Course of Theoretical Physics; Volume 5). Butterworth-Heinemann, 1980.
- [23] J. Mathews and R. L. Walker. *Mathematical Methods of Physics*. Addison-Wesley (1970).

## Theory of Quasicrystals

- [24] P. Bak and A. Goldman. "Quasicrystallography." *Introduction to Quasicrystals*. M. Jarić, ed. Academic Press (1988).
- [25] P. A. Bancel, P. A. Heiney, P. W. Stephens, A. I. Goldman and P. M. Horn. "Structure of Rapidly Quenched Al-Mn." *Physical Review Letters*. **54** 2422-2425 (1985).
- [26] V. Elser. "Indexing problems in quasicrystal diffraction." *Physical Review B*. **32** 4892-4898 (1985).
- [27] C. Janot. *Quasicrystals: a primer*. Oxford (1994).
- [28] D. Levine and P. Steinhardt. "Quasicrystals: A New Class of Ordered Structures." *Physical Review Letters*. **53** 2477-2480 (1984).
- [29] N. D. Mermin. *Reviews of Modern Physics*. **64** 3-49 (1992).
- [30] M. Senechal. *Quasicrystals and Geometry*. Cambridge (1995).
- [31] D. Schectman, I. Blech, D. Gratias and J. W. Cahn. "Metallic Phase with Long-Range Orientational Order and No Translational Symmetry." *Physical Review Letters* **53** 1951-1953 (1984).
- [32] P. J. Steinhardt and S. Ostlund. *The Physics of Quasicrystals*. World Scientific (1987).
- [33] P. J. Steinhardt and D. P. DiVicenzo. *Quasicrystals: The State of the Art*. 2nd Ed. World Scientific (1999).

### Simple Icosahedral Quasicrystals

- [34] F. Gayle. *Journal of Materials Research*. **2** 1 (1987).

- [35] Z. R. Huang, G. Z. Pan, D. Y. Yang and X. S. Chen. “T<sub>2</sub> AlLiCu Structure and its Phase Transition under Heat Treatment.” *Solid State Communications.* **63** 951-954 (1987).
- [36] V. V. Rao and T. R. Anantharaman. “Icosahedral Al<sub>6</sub>Mg<sub>4</sub>Cu: Interpretation of X-ray Reflections and Electron Micrographs.” *Phase Transitions.* **16/17** 609-613 (1989).
- [37] Y. Shen, S. J. Poon, W. Dmowski, T. Egami and G. J. Shiflet. “Structure of Al-Li-Cu Icosahedral Crystals and Penrose Tiling.” *Physical Review Letters.* **58** 1440-1443 (1987).
- [38] M. Tanaka, M. Terauchi and T. Kaneyama. *Convergent-Beam Electron Diffraction II.* Jeol (1988).
- [39] N. Yu, R. Portier, D. Gratias, K. Yu-Zhang and J. Bigot. “Al<sub>6</sub>CuLi<sub>3</sub>-T2: A Stable Icosahedral Phase?” *Materials Science Forum.* **22-24** 579-590 (1987).

### **Quasicrystal Properties and Applications**

- [40] P. C. Gibbons and K. F. Kelton. “Toward Industrial Applications.” *Physical Properties of Quasicrystals.* Z. M. Stadnik, Ed. Springer-Verlag (1998).
- [41] O. Rapp. “Electronic Transport Properties of Quasicrystals – Experimental Results.” *Physical Properties of Quasicrystals.* Z. M. Stadnik, Ed. Springer-Verlag (1998).
- [42] M. E. Zoorob, M. D. B. Charlton, G. J. Parker, J. J. Baumberg, and M. C. Netti. “Complete photonic bandgaps in 12-fold symmetric quasicrystals.” *Nature.* **404** 740-743 (2000).

### **Electron Microscopy and Microanalysis**

- [43] J. I. Goldstein, D. E. Newbury, P. Echlin, D. C. Joy, A. D. Romig, Jr., C. E. Lyman, C. Fiori and E. Lifshin. *Scanning Electron Microscopy and X-Ray Microanalysis*. 2nd Ed. Plenum (1992).
- [44] A. Putnis. *Introduction to Mineral Sciences*. Cambridge (1992).
- [45] L. Reimer. *Scanning Electron Microscopy: Physics of Image Formation and Microanalysis*. 2nd Ed. Springer (1998).

### Incommensurate Minerals

- [46] B. Dam, A. Janner and J. D. H. Donnay. "Incommensurate Morphology of Calaverite ( $\text{AgTe}_2$ ) Crystals." *Physical Review Letters*. **55** 2301-2304 (1985).
- [47] V. Goldschmidt, C. Palache and M. Peacock. *Neues Jahrbuch Fur Mineralogie*. **63** 1-58 (1931).
- [48] A. Janner and B. Dam. "The Morphology of Calaverite ( $\text{AuTe}_2$ ) from Data of 1931. Solution of an Old Problem of Rational Indices." *Acta Crystallographica*. **A45** 115-123 (1989).
- [49] W. J. Schutte and J. L. De Boer. "Valence Fluctuations in the Incommensurately Modulated Structure of Calaverite  $\text{AuTe}_2$ ." *Acta Crystallographica*. **B44** 486-494 (1988).
- [50] G. Van Tendeloo, P. Gregoriades and S. Amelinckx. "Electron Microscopic Studies of Modulated Structures in  $(\text{Au},\text{Ag})\text{Te}_2$ : Part I. Calaverite  $\text{AuTe}_2$ ." *Journal of Solid State Chemistry*. **50** 321-334 (1983).
- [51] G. Van Tendeloo, P. Gregoriades and S. Amelinckx. "Electron Microscopic Studies of Modulated Structures in  $(\text{Au},\text{Ag})\text{Te}_2$ : Part II. Sylvanite  $\text{AgAuTe}_4$ ." *Journal of Solid State Chemistry*. **50** 335-361 (1983).

- [52] G. Van Tendeloo, S. Amelincx, and P. Gregoriades. "Electron Microscopic Studies of Modulated Structures in (Au,Ag)Te<sub>2</sub>: III. Krennerite." *Journal of Solid State Chemistry*. **53** 281-289 (1984).
- [53] Ecclesiastes 1:9-10. *New American Standard Bible, Updated Edition.* (1999).
- [54] Romans 16:27. *New American Standard Bible, Updated Edition.* (1999).

# List of Figures

1.1	Restrictions on lattice symmetry due to the imposition of periodicity	19
1.2	Attempted tiling of the plane with regular pentagons.	20
1.3	Pyritohedral Pyrite crystals.	21
2.1	Fraunhofer (far-field) diffraction	25
2.2	General scattering geometry, showing incident $\vec{k}$ , final $\vec{k}'$ and scattering $\vec{q}$ wave vectors.	29
2.3	Lattice planes and a reciprocal lattice vector.	32
2.4	Bragg Scattering	35
3.1	Projection of a two-dimensional square lattice onto a line of irrational slope, creating a one-dimensional quasilattice. $A'$ , $B'$ and $C'$ are the projections of <b>A</b> , <b>B</b> and <b>C</b> along $a_{\parallel}$ . $ B' - C' $ has length $\Delta a_{\parallel} = a_0$ ; $ A' - B' $ has length $\Delta a_{\parallel} = \tau a_0$ . The window (gray bar) has width $\Delta a_{\perp} = a_1$ .	46
3.2	Transmission electron microscope image of the quasilattice of an Al-CuFe quasicrystal, with the five planes of symmetry labeled with arrows.	52
3.3	Powder pattern of ideal simple icosahedral quasicrystal for $-4 \leq n_i \leq +4$ and $ Q_{\perp}  \leq 12$ .	57
4.1	Powder pattern of ideal simple icosahedral lattice	66

4.2	Scatterplot in which both parameters $A$ and $B$ , hypothetical parameters for the purpose of illustration, effectively separate the quasicrystals. Blue and red ellipses encompass the known quasicrystals and most of the minerals, respectively. Centers of the ellipses are marked with yellow crosses; the crosses are separated in both parameters, and the ellipses are distinct. The solid green lines near the origin represent the range intercepted by projecting the blue ellipse onto the two axes, then extending those projections to the origin. . . . .	73
4.3	Scatterplot in which parameter $B$ is effective at separation, but parameter $C$ is not. $B$ and $C$ are hypothetical parameters for the purpose of illustration. The crosses are thus separated by a good distance along the $x$ -axis, but are close together in $y$ -axis position. . . . .	74
4.4	Both parameters $C$ and $D$ are ineffective at separation. $C$ and $D$ are hypothetical parameters for the purpose of illustration. The crosses are close together in both $x$ and $y$ , and the ellipses overlap significantly. . . . .	74
4.5	Scatterplots of $N$ vs. % Deviation. Top plot based on unweighted averages, bottom plot based on averages weighted by intensity alone. $N$ is the weighted average length of the the closest matching six-dimensional scattering vector $ \vec{Q} $ . The % Deviation is the average of percent deviations in $ \vec{Q}_{\parallel} $ between real and closest matching ideal peaks. . . . .	76
4.6	Scatterplots of $N$ vs. $ Q_{\perp} $ , for averages weighted by intensity alone. $ Q_{\perp} $ is the magnitude of the $\vec{Q}_{\perp}$ vector of the closest matching ideal peak. . . . .	77
4.7	Scatterplot of $ Q_{\perp} $ vs. % Deviation, based on averages weighted by intensity alone. . . . .	78
4.8	Number of peaks in the real data vs. the number of (2, 1) pairs, per pattern. Only patterns with $\geq 12$ peaks are checked by the programs. . . . .	79

4.9	Average $ Q_{\perp} $ weighted by intensity alone vs. the percentage of peaks involved in a $(\Delta N, \Delta M) = (2, -1)$ pair. . . . .	80
4.10	Average $ Q_{\perp} $ weighted by intensity alone vs. match percentage. The match percentage is the percentage of ideal calculated peaks which after scaling fell within the range of real data that were matched to real peaks. . . . .	81
4.11	Scatterplots of $N$ vs. $ Q_{\perp} $ based on averages weighted by $\sqrt{I}$ (top) and $I$ (bottom). . . . .	82
5.1	Diagram of the basic parts of a scanning electron microscope. Not to scale. . . . .	87
5.2	“Potential barrier (work function $\phi_w$ ) at the metal-vacuum boundary and decrease of potential energy $V(z)$ with increasing external field $E$ for thermionic, Schottky and field emission.”[45] . . . . .	89
5.3	Energy distribution of electron interactions. Secondary electrons (SE), with a peak at 3-5 eV, are defined to be less than 50 eV. Backscattered electrons (BSE) have energies from 50 eV to the beam energy (usually 10-20 keV). . . . .	89
5.4	Interaction volumes for electron interactions. . . . .	90
5.5	Everhart-Thornley detector for secondary electrons.[45] . . . . .	92
5.6	A secondary electron image of the mineral keithconnite. . . . .	93
5.7	Annular silicon ring detector for backscattered electrons.[45] . . . .	95
5.8	“Increase of the backscattering coefficient $\eta$ and the secondary electron yield $\delta$ of 25 – 30 keV electrons with increasing $Z$ .”[45] . . . . .	95
5.9	A backscattered electron image of the mineral keithconnite. The two brighter grains toward the upper right corner of the image are lead-bearing galena. . . . .	97
5.10	Silicon detector for energy-dispersive spectroscopy of X-rays.[45] . . .	98

5.11 Energy-dispersive spectroscopy spectrum of keithconnite. The $L\alpha$ lines for palladium and tellurium are marked. The peak around 0.3 keV originates from the carbon coat put over the sample to increase conductivity.	99
5.12 Electron backscattering diffraction pattern detector.[45]	100
5.13 Electron backscattering diffraction from an AlCuFe icosahedral quasicrystal. A five-fold axis of symmetry is visible in the lower left-hand corner.	101
5.14 Secondary electron image of the surface of the AlCuFe icosahedral quasicrystal from which the diffraction pattern in figure 5.13 was taken.	101
5.15 Diagram of the basic parts of a transmission electron microscope. Not to scale.[44]	104
5.16 Electron diffraction pattern along a two-fold axis of an AlCuFe icosahedral quasicrystal.	105
6.1 Transmission electron microscope image of the Krennerite lattice. The material in the upper left corner is amorphous carbon on the sample holder.	109
6.2 Electron diffraction pattern of calaverite, with several satellite peaks surrounding each major crystal peak. From [50], inverted (light and dark reversed) for clarity.	110
6.3 Electron diffraction pattern from the Krennerite lattice.	112
6.4 Electron diffraction pattern from the Krennerite lattice. This is the same original image as figure 6.3, except that the brightness has been decreased and contrast increased to highlight weaker peaks.	113
6.5 Electron diffraction pattern from the Krennerite lattice. Relative to figure 6.4, the brightness has been further decreased and contrast further increased.	114
6.6 Transmission electron microscope image of synthetic $\text{Ni(OH)}_2$ from Aldrich Chemical Company. The typical grain size is $\approx 10 - 50$ nm.	115

6.7 Electron diffraction image of synthetic Ni(OH) <sub>2</sub> . The diffraction pattern could not be obtained from individual crystal grains, since they were too small. The image reflects contributions from grains spanning a number of orientations. Consequently, there are rings instead of a set of discrete points. . . . .	115
6.8 Secondary electron image of a silver telluride grain in host rock from Baiwa, New Zealand. No volynskite grain can be seen using this imaging technique (compare figure 6.9). The rounded features in the upper and lower right corners of the image are artifacts of charging. . . . .	117
6.9 Backscattered electron microscope image of volynskite (circled in white) embedded in a silver telluride grain in host rock from Baiwa, New Zealand. . . . .	117
6.10 Spectrum from energy-dispersive spectroscopy analysis of the large silver telluride grain in figure 6.9. <i>Bi</i> , <i>Ag</i> , and <i>Te</i> mark the positions of the Bi-M $\alpha$ , Ag-L $\alpha$ and Te-L $\alpha$ transition lines. There is no peak around the <i>Bi</i> line. . . . .	118
6.11 Spectrum from energy-dispersive spectroscopy analysis of the small volynskite grain circled in figure 6.9. <i>Bi</i> , <i>Ag</i> , and <i>Te</i> mark the positions of the Bi-M $\alpha$ , Ag-L $\alpha$ and Te-L $\alpha$ transition lines. . . . .	118
7.1 Scatterplots of $N$ vs. $ Q_{\perp} $ based on averages weighted by $\sqrt{I}$ . . . . .	120

# List of Tables

4.1	Theophrastite powder diffraction pattern from the Powder Diffraction File. The first two columns list the six-dimensional icosahedral indexing and Janot's ( $N, M$ ) indices (see section 3.4) as calculated by our program. The third column lists the hexagonal Miller indices from the Powder Diffraction File itself. The last three columns contain the value of $ Q_{\parallel} $ from the real data, the result from indexing with icosahedral vectors, and the result from indexing with the ordinary hexagonal vectors. . . . .	69
4.2	Table of published simple icosahedral quasicrystals and the weighted average parameters $N$ , % Deviation and $Q_{\perp}$ . . . . .	71
4.3	Top ten mineral candidates for quasicrystallinity. $N$ is the weighted average length of the scattering vector $ \vec{Q} $ . % Dev. is the weighted average of deviations between real and calculated values of $ \vec{Q}_{\parallel} $ . $Q_{\perp}$ is the weighted average of $ \vec{Q}_{\perp} $ . Pair % is the percentage of real data peaks involved in a (2, -1) pair. Weight is the weighting factor used, either intensity $I$ or its square root $\sqrt{I}$ . . . . .	83
6.1	Top ten mineral candidates for quasicrystallinity. . . . .	108